

Copyright © 1998, by the author(s).
All rights reserved.

Permission to make digital or hard copies of all or part of this work for personal or classroom use is granted without fee provided that copies are not made or distributed for profit or commercial advantage and that copies bear this notice and the full citation on the first page. To copy otherwise, to republish, to post on servers or to redistribute to lists, requires prior specific permission.

PLASMA AT THE EDGE, PART I

by

David J. Cooperberg and Charles K. Birdsall

Memorandum No. UCB/ERL M98/31

1 June 1998

Reprinted – 3 December 1999

COVER

PLASMA AT THE EDGE, PART I

by

David J. Cooperberg and Charles K. Birdsall

Memorandum No. UCB/ERL M98/31

1 June 1998

Reprinted – 3 December 1999

ELECTRONICS RESEARCH LABORATORY

College of Engineering
University of California, Berkeley
94720

PLASMAS AT THE EDGE, Part I.

David J. Cooperberg and Charles K. Birdsall

June 1, 1998

ABSTRACT

Modeling and Simulation of High Frequency Surface Waves in Bounded Plasmas

1 Introduction

Our Berkeley Plasma Theory and Simulation Group (PTSG) has been studying bounded plasmas and plasma devices since about 1981, in which the behavior of the plasma at the edge plays a major role. PTSG has published many journal articles in this area. We also have generated a suite of plasma device codes now in world-wide use by many others, who have published something approaching 100 journal articles, using our codes. Our plasma PIC-MCC codes are available free on the web from <http://ptsg.eecs.berkeley.edu>

This report contributes detailed theory and simulation for high frequency (electron) waves that may propagate along the plasma edge, with perturbations in the potential and density in the sheath and pre-sheath regions. A brief summary comes first. The report then begins with Chapter 1 of David Cooperberg's thesis (his title is the Abstract above) which provides an extensive history of the area, followed by his Chapters 2, 3, 4, and 5 as journal articles, plus a short Chapter 6 on future research. That is, this report is Dr. Cooperberg's thesis.

2 Yet to come

In the next year or so, succeeding Parts II, III, IV..., chapters from more Berkeley Ph.D. theses, will be published, also as ERL reports, including low frequency edge waves (at "ion frequencies"), with additional results on coupling to both the high and low frequency edge waves.

There also will be some work on pure electron plasma waves oscillating near and propagating along electron emitters, with attention to both noise and stability, magnetized and not.

3 Acknowledgment of Support

We are very grateful for continual support from ONR, dating from 1977, for most of this work, and for the continued support of Dr. Charles Roberson at ONR for "plasmas at the edge", both near-neutral and non-neutral. David Cooperberg was an ONR ASSERT student. Further support came from ONR Contract N000014-97-1-0241.

SHEATH WAVES, UNMAGNETIZED

David J. Cooperberg, Charles K. Birdsall

EECS Department, University of California, Berkeley CA 94720-1770

Plasmas bounded with metal walls have sheaths at their edges near the walls, along which electrostatic (and electromagnetic) waves may propagate. We build on a long history of dielectric-bounded plasma waves, e.g., relating transverse (or series) resonances to cut-off frequencies of our sheath waves. We present kinetic simulations (PIC-MCC), confirming: the dispersions; the edge (surface) waves perturbed densities and potentials are largest at the edge (with the perturbed fields of the asymmetric modes penetrating the bulk at small values of k); those of the body waves are largest in the body. Physically, the two sets of waves are guided along their respective regions.

We also drive edge waves sufficiently strongly to cause electron heating producing ionization of the background gas, which maintains a plasma discharge. The heating profiles and density scaling of these resonant surface wave discharges differ markedly from the well known capacitive, inductive, and wave-coupled discharges.

First, using warm electrons and fixed ions (matrix sheath), electron surface waves in a plasma slab bounded by metal walls have been analyzed and detected. (See Ref 1.) Second, a more realistic model is used, with warm electrons and ions, free to seek equilibrium, creating a nonuniform self-consistent density, with sheaths, presheaths, and bulk regions, still between metal walls. (See Ref. 2.) For both models, dispersions and eigenfunctions of electrostatic, asymmetric and symmetric, surface and body waves, are obtained from a linearized Vlasov theory. These are then verified with PIC simulations in 2d3v. Propagation of surface and body waves occur analogous to those found in dielectric bounded plasmas, such as Trivelpiece-Gould waves. The lowest frequency asymmetric surface wave, a dipole-like mode, has a cutoff at the series resonance (infinite admittance), also called the lowest frequency Tonks-Dattner or Herlofson resonance; these are followed by higher order surface wave modes, with higher frequency cutoffs. The highest frequency modes are body waves, with Bohm-Gross like dispersion. Collisionless damping is also found and observed.

Third, a plasma with argon neutrals, ions and electrons between two parallel metal plates, is driven (in PIC-MCC 1d3v simulations) by an RF voltage source, with sufficient strength to just maintain a discharge. The minimum required externally applied voltages (near series resonance, with frequencies from 110-470 MHz) were on the order of the electron temperature (a few eV), with correspondingly low plasma potentials (a few 10's of volts). At 470MHz and a pressure of 10 mTorr, the peak, central, electron (and ion) density was $7.2 \times 10^{13} \text{ cm}^{-3}$. (Extrapolation to drive at 2450 MHz indicates a peak density of $1 \times 10^{13} \text{ cm}^{-3}$.) The argon neutral gas pressures were 2-300 mTorr. The diode (gap) impedance was observed to be nearly resistive (as expected at or near resonance). The EEPF's, electron heating profiles, and scaling laws are found to be different from the more common capacitively, inductively and wave-coupled discharges. The self-tuning of the discharge, needed to maintain resonance, is described. See Ref. 3.

Lastly, using a fully electromagnetic 2d3v PIC-MCC code, a plasma is created and sustained by resonant surface waves in a metal bounded cavity 2 by 8 cm at a drive frequency of 150MHz (vacuum wavelength of 2m), applied with a set of antennas (along one of the longer walls) phased to produce a standing wave. See Ref. 4.

Support came from ONR for a student AASERT and ONR Contract N00014-97-1-0241

1. D. J. Cooperberg, *Physics of Plasmas* 5, No. 4 pp.853-861, April 1998.
2. D. J. Cooperberg, *Physics of Plasmas*, 5, No. 4, pp. 862-872, April 1998.
3. D. J. Cooperberg and C. K. Birdsall, *Plasma Sources Sci. Technol.*, 7, pp. 96-113, May 1998.
4. D. J. Cooperberg and C. K. Birdsall, *Plasma Sources Sci. Technol.*, 7, pp. 41-53, February 1998.

**Modeling and Simulation of High Frequency Surface Waves in Bounded
Plasmas**

by

David Jeffrey Cooperberg

**B.S. (Cornell University, Ithaca) 1990
M.A. (University of California, Berkeley) 1992**

**A dissertation submitted in partial satisfaction of the
requirements for the degree of
Doctor of Philosophy**

in

Physics

in the

**GRADUATE DIVISION
of the
UNIVERSITY of CALIFORNIA at BERKELEY**

Committee in charge:

**Professor Charles K. Birdsall, Chair
Professor Joel Fajans
Professor Jonathan S. Wurtele
Professor Michael A. Lieberman**

1998

Abstract

Modeling and Simulation of High Frequency Surface Waves in Bounded Plasmas

by

David Jeffrey Cooperberg

Doctor of Philosophy in Physics

University of California at Berkeley

Professor Charles K. Birdsall, Chair

“For many years plasma simulations were focused on the behavior of the bulk of the plasma, as there are many oscillations, waves, instabilities, and transport problems [to study] in the bulk... For many such models, periodic boundary conditions were acceptable, essentially ignoring boundaries.”[1]. In the past decade accurate modeling of bounded plasma has advanced considerably motivated in part by a need to describe edge transport in fusion devices and in part by a desire to model DC, RF, and microwave discharges which are commonly used in plasma-assisted materials processing.

In the work presented here, we shall make a careful examination of an intrinsic property of bounded plasmas. Specifically, we will be studying a set of high frequency (electron) waves which propagate at the boundary of metal bounded plasmas. It will be shown that their existence and behavior requires an accurate model of the plasma edge and sheath regions.

This work has two main objectives. The first is to clarify the structure of these waves. While there has been considerable experimental and analytic work on electron surface waves in dielectric bound plasmas, there has been little or no investigation of the surface modes in a metal bound slab. Part of the reason for this is that metal bound plasmas are less accessible for some experimental techniques which include wave excitation and detection schemes (typically done with antennae positioned outside the dielectric bound plasma) and partly because it may have been believed that the electric fields of surface waves in metal bound plasmas would be shorted out by the conducting boundaries close to the plasma. This is not the case, as will be demonstrated. It is also hoped that this use of

simulation in the study of electron surface waves will further our general understanding of these waves in both metal and dielectric bound plasmas.

Our second objective is to study how these natural modes may be used to sustain a plasma discharge suitable for plasma processing. Current “surface wave plasmas” are produced in glass tubes with short-gap excitation[2]. Our analysis of surface waves in planar metal bounded plasma slabs enables us to demonstrate, through simulation, new types of surface wave sustained discharges which may operate at low pressures with low sheath potentials and may be scalable to large areas without compromising plasma uniformity.

This study of surface waves in metal bound plasmas also leads to speculation as to the use of such waves in controlling the plasma edge (and possibly the bulk). The application of microwave power at the plasma edges may be used to excite these surface modes and enhance plasma heating there. The effect might be enhanced plasma uniformity in traditional capacitively and inductively coupled discharges.

This work relies heavily on particle-in-cell simulation with Monte-Carlo collisions (PIC-MCC)[1, 3, 4] of unmagnetized, bounded $2d3v$ plasmas. Among the benefits of the PIC-MCC scheme are an adherence to first-principles, which allows a wide range of kinetic, non-linear, non-equilibrium, and non-local behavior to be accurately modeled, and an ease of collecting virtually any diagnostic that could be desired (at any and all positions in phase-space). The accuracy provided by PIC-MCC is of particular importance to this work because of a desire for an accurate representation of sheaths, non-linear effects, and kinetic effects such as Landau damping, stochastic heating, and wave-particle interactions. Also accurate modeling of the electron energy probability function (EEPF) is desired since the EEPF is known to depart from Maxwellian in low pressure discharges[5][6].

An outline of this work is as follows. Chapter 1 presents an overview of past and current work on electron surface oscillations and waves in bounded plasmas. In Chapter 2 we initiate our study of waves in the metal bound slab using a matrix sheath model. A linearized Vlasov treatment for this model is derived and compared to simulation. Next a more realistic model for the plasma and sheath is developed in Chapter 3. The result is the identification of a new set of surface modes which exist only in the non-uniform, thermal, bounded plasma. We then move from the study of surface wave characteristics to a study of surface wave sustained discharges. In Chapter 4 we consider the $1d3v$ plasma which is sustained at the series resonance frequency (which will be shown to be the cut-off frequency for the main asymmetric surface wave). The $2d3v$ surface wave sustained slab

3:

will be treated in Chapter 5.

Charles K. Birdsall

Professor Charles K. Birdsall
Dissertation Committee Chair

Acknowledgements

There are many people to thank for helping me complete this dissertation and for making my years in graduate school as rewarding as they have been.

First, I would like to thank Prof. Birdsall for giving me the opportunity to work with him and his Plasma Theory and Simulation Group (PTSG). Prof. Birdsall's suggestions and extensive experience with plasma simulation helped me define my research. During the course of my studies, as my research interests evolved, I could always count on Prof. Birdsall's open-minded support and encouragement. His enthusiasm both inside the office and out has been inspirational.

I would also like to thank my dissertation committee members, Prof. C. K. Birdsall, Prof. Joel Fajans, Prof. Jonathan S. Wurtele, and Professor Michael A. Lieberman for their careful and thoughtful review of this manuscript. They have provided many insightful comments from which I and this dissertation have benefited.

There are many members, past and present, of PTSG to whom I owe much gratitude including Vahid Vahedi, John Verboncoeur, Keith Cartwright, Peter Mardahl, Emi Kawamura, Peggy Christenson, Morgan Oslake, Venkatesh (PG) Gopinath, Payam Mirrashidi. They have all contributed to my success as a graduate student. Many stimulating discussions about PIC simulation, plasma physics, and "Babylon 5" have been especially appreciated. There have also been many visitors to the group who I will not list here but who have also offered valuable insights.

A special thanks must be given to Vahid Vahedi and John Verboncoeur, for helping me become acquainted with the many PIC codes developed at PTSG. Having the opportunity to absorb some of their knowledge of plasma simulation was very helpful. Their assistance in helping me adapt XDPD2 for this work is greatly appreciated. Discussions with former PTSGer, Dr. X. Q. Xu, helped familiarize me with his earlier work on sheath waves.

This work was supported in part by an Office of Naval Research ASSERT (N100014-93-1-1389). Much of the simulation work presented in Chapter 5 was performed with resources made available by the Berkeley NOW Project computing facility.

Of course a rewarding graduate school experience must allow for the occasional distraction and diversion in order to break up the often long hours spent working and studying. I have been fortunate enough to participate in more than a few such activities.

Thanks to the beer brewing squad, the poker group, the volleyball team, the hiking and biking companions, and all those who made attending conferences much more fun than they might have been.

I must also thank the folks at 1992 Yosemite (Tim Shaw, Peter Schupp, Ted Kyi, Bob Pape), where I lived for the majority of my graduate student days, and where many a good time and good barbecue were had.

Thanks also to Jaimie Yeh for making my early career as a solid-state experimentalist much more enjoyable than it might have been and especially for introducing me to Lisa.

Of course I could not have made it through graduate school without the support of my family for which I am truly grateful.

Most of all, I would like to thank Lisa Goddard, my fiancée, for her faith in me, and for all the inspiration and support she has given me.

Chapter 1

Brief History of Electron Resonances and Surface Waves in Bounded Plasmas

Plasmas bounded by conducting or dielectric walls provide regions near the plasma edge in which the permittivity, ϵ , changes sign. This sign change takes place at the plasma/dielectric interface in the dielectric bounded case, at the plasma/sheath interface for a uniform metal bounded plasma with a matrix sheath, and at some intermediate point inside the plasma (where the local plasma frequency equals the excitation frequency) for non-uniform plasmas. A consequence of this sign change in ϵ is the introduction of surface wave modes. The field strength in these modes is greatest at a point near the plasma boundary and decays exponentially away from this point. One dimensional simulations of a plasma slab show: (a) plasma oscillations at high frequencies ($\omega \gtrsim \omega_{pe}$), associated with the bulk; and (b) resonances (main or series, and secondary or Tonks-Dattner) on the order of but less than ω_{pe} , associated with the edges. Two dimensional simulations of a plasma slab similarly show modes associated with the bulk and waves which propagate along the walls (in \hat{y}) which are localized in the edge (analogous to Gould-Trivelpiece and Tonks-Dattner waves in a plasma column). The resonances found in 1d are the cut-off frequencies ($k_y = 0$) in 2d. Evidence of the series resonance in a parallel plate discharge is demonstrated by the measurement of plasma impedance which approaches a pure resistance when driving at or near $f_{series} = f_{pe}(2s/L)^{1/2}$ (where s is the sheath width and L is the total system width).

In 2d thermally excited waves can be detected via spectral analysis and also can be driven to sustain a plasma. Before proceeding with a further description of the current work on surface modes found in the metal bounded slab, we present a history of the experimental and theoretical advances made in understanding high frequency surface waves in bounded plasmas, and advances in the area of surface wave produced plasmas.

1.1 Detection and Analysis of Surface Waves

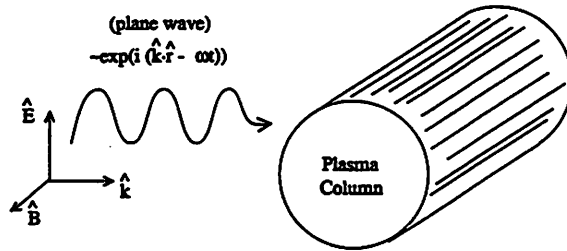


Figure 1.1: Schematic of experiment to detect electron resonances in a plasma column.

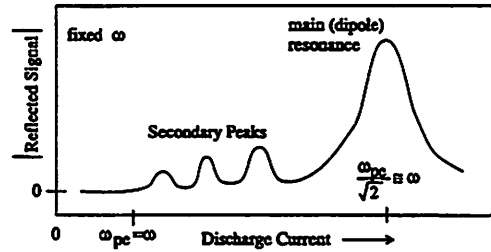


Figure 1.2: Sketch of scattered field intensity

Electron resonances in bounded plasmas have been studied and observed for some time. In 1931 Tonks[9][10] studied the fields scattered by a plasma column and found that the scattered field versus plasma density exhibits multiple resonances (Figs. 1.1 and 1.2) with a main resonance at $\omega = \omega_{pe}/\sqrt{2}$ and secondary resonances at lower densities. The main resonance was re-derived by Herlofson[11] in 1951 in a study of resonant scattering from ionized meteor tails. Herlofson further showed that only a single dipolar resonance existed in the cold plasma limit in contradiction to observation. Later laboratory experiments were performed by Dattner[12] in which he measured the electron densities at which the secondary resonances occurred. These secondary resonances shall hereafter be referred to as Tonks-Dattner resonances as is done in the literature.

A cold homogeneous treatment of the plasma cylinder experiments describes only the main (dipole) resonance. Vandenplas[13] outlines the research which eventually led to a better theoretical model of the plasma cylinder which accurately predicted the Tonks-Dattner resonances. The first analysis was performed for a uniform thermal plasma. A formula for the resonances is then

$$\omega^2 = \omega_{pe}^2 [1 + 3\lambda_{De}^2 k_n^2], \quad (1.1)$$

where the discrete k_n are determined by enforcing a boundary condition of zero perturbed flux at the cylinder wall. While a secondary spectrum is predicted, the spacing and location of the resonances was in poor agreement with observation. The next addition to the analytical work involved the inclusion of a plasma radial density profile[14][15][16]. The hot non-uniform plasma was described by a linearized fluid calculation which included a scalar perturbed pressure term. Good agreement with experiment was shown by Parker *et. al.*[15] when a Tonks-Langmuir[17] model of the steady-state electron density was used. Here the resonances may be understood as radial longitudinal standing waves confined in the region between the plasma boundary and the cutoff radius where $\omega = \omega_{pe}(r_c)$. Gaigneaux and Vandenplas[18] extended the work of Parker *et. al.*[15] by introducing new dimensionless parameters and a general linear law permitting a prediction of the Tonks-Dattner resonance spectrum over a wider range of plasma densities and also allowing for an independent measure of electron temperature.

The limits of applicability of the scalar perturbed pressure fluid treatment, which has been successful in predicting the resonance spectrum, have been analyzed by Baldwin[19]. Baldwin showed that for afterglow plasmas with sufficiently slowly varying density profiles the perturbed scalar pressure fluid treatment breaks down and one should apply a kinetic treatment of the problem. The reason, in keeping with the idea that the resonances consist of longitudinal waves trapped at the plasma boundary, is that the waves which are launched at the critical point $\omega = \omega_{pe}(r_c)$ can become severely Landau damped as they approach the outer wall. This is because the decreasing density leads to a decreasing phase velocity for the longitudinal waves. The linearized Vlasov equation is solved by the trajectory method for this case. The resonant particles responsible for Landau damping the outward traveling wave are shown to partially reconstruct an inward traveling wave after reflection by the plasma sheath potential. Proof of the validity of this analysis was offered when it was shown that application of a weak axial magnetic field destroyed the resonance spectrum[20]. Ignat[21] attempted to verify the analysis of Baldwin by comparing the predicted resonance spectrum to experiment on argon, helium, and neon afterglow plasmas; however, the “flawed” calculation of Parker *et. al.*[15] yielded better agreement.

In addition to the experiments performed on plasma cylinders, a study of plasma resonance probes which measured resonances at frequencies below ω_{pe} were explained in terms of the “series resonance”[13, 22, 23]. The “series resonance” results from the balancing of the probe capacitive sheath impedance with the bulk plasma’s primarily inductive

impedance, and is analogous to the main dipole resonance in a plasma cylinder.

The electron resonances found in a radially bounded plasma represent cutoffs for waves which may propagate along the boundary wall. Trivelpiece and Gould[24] derived dispersion relations for the cold plasma cylinder bounded by dielectric and metal with and without an applied steady axial magnetic field. Modes with frequencies well below the metal waveguide cutoffs and phase velocities much less than the velocity of light were handled in the quasi-static limit. Analytic results were compared favorably with experimental measurements. For zero applied magnetic field, particular attention is given to describing a circularly symmetric mode as resulting from a perturbed peristaltic surface charge layer (see Figs. 1.3 and 1.4). A more thorough quasi-static, $T_e = 0$ treatment of the surface modes

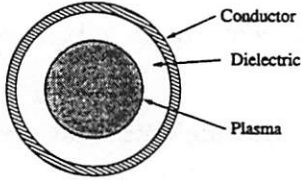


Figure 1.3: Cross-section of column used in experiment to detect electron resonances in a cylindrical, bounded plasma. (after Trivelpiece[7])

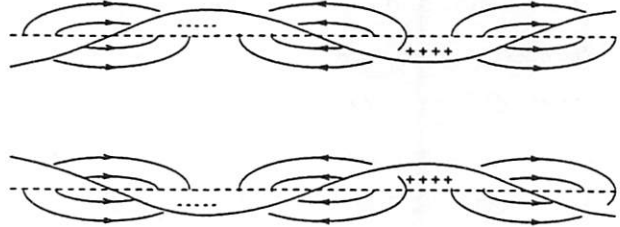


Figure 1.4: Snapshot of electric fields and perturbed surface charge layer formed by peristaltic perturbation of electron density about an equilibrium cylindrical (ion) density profile. (after Trivelpiece[7])

on a bounded plasma column with zero axial magnetic field is provided by Trivelpiece[7]. Modes with $m = 1$ (dipole) angular variation are discussed. The cut off for this mode is essentially the main resonance discussed earlier with a modification due to dielectric and metal boundaries. A further result is that, for parabolic radial plasma density profiles, the low frequency behavior of these surface waves may be accurately captured by replacing ω_{pe} with its spatially averaged value. We shall refer to these surface waves which have been derived in the $T_e = 0$ limit as Gould-Trivelpiece modes as is commonly done in the literature.

Two review articles[25][26] have been written about the cylindrical surface waves (Gould-Trivelpiece modes). Topics including damping, methods for launching and detection, linear dispersion as derived from fluid and kinetic calculations and measured by experiment, and non-linear phenomenon, including second order interactions leading to the generation of Tonks-Dattner waves, are discussed. Also an informative diagram is given[26] which

summarizes the regimes under which various simplifications may be made.

Computer simulation of surface waves has been performed by Decyk[27][28]. In this work a measurement of the autocorrelation of the potential in electrostatic simulations of a uniform thermal plasma slab bounded by vacuum were used to measure the dispersion relation for two electron surface wave branches whose frequencies were below ω_{pe} . One was symmetric and the other was asymmetric in the direction perpendicular to the boundaries. Body waves with frequencies above ω_{pe} were also measured in these simulations. The eigenfunctions and real ω dispersion curves for these modes were derived from a warm fluid calculation and plotted. The imaginary ω part of the dispersion relation resulting from Landau damping was measured and compared to the results of a kinetic Vlasov calculation performed by Cheng and Harris[29].

The additional Tonks-Dattner resonances of a plasma column also represent cut-offs for axially propagating surface waves as has been observed by O'Brien *et. al.*[30], O'Brien[31], Kerzar *et. al.*[32], and Kerzar and Weissglas[33] and others. In these works, experimental measurements are compared with several theories which differ in the modeling of the radial plasma density profile. A numerical solution is also found by extending the method of Parker *et. al.*[15] to include axial propagation. Surprisingly, only fair agreement seems to have been achieved. Only the first three azimuthally symmetric modes and first two dipole modes were detected. Difficulty in detecting modes of higher angular dependence and higher radial mode number was caused by coupling to lower modes, as well as the higher damping present in higher modes.

Some kinetic modeling of surface waves has been performed which demonstrates the effects of collisionless (Landau) damping. Atanasov *et. al.*[34] find the exact solution of the linearized Vlasov's and Maxwell's equations for a bounded, homogeneous (to zeroth order), hot plasma column under the condition of specular reflection at the plasma boundaries and azimuthal symmetry (the $m=0$ mode). The dispersion relation including a space damping rate are obtained. A similar approach is taken by Dengra and Ballesteros[35] in which the collisionless energy absorbed per electron is calculated. The omission of a radial density variation severely limits the accuracy of these results.

Another phenomenon is theorized by Gradov and Stenflo[36] in their discussion of linear cold bounded plasma slab. Here the authors describe resonant damping of surface wave eigenmodes in a plasma slab with an edge density gradient. In their description, surface waves excite a local Langmuir wave at some location near the plasma boundary where the

density is decreasing such that the local ω_{pe} equals the surface wave frequency and this Langmuir wave continues outward (towards lower density) until it is Landau damped away. The dispersion relation including the described damping and the time dependence of the electric field at the point where $\omega_{pe}(r_c) = \omega$ are derived.

1.2 Surface Waves to Sustain Discharges

The waves and resonances discussed above, which have been studied to further the basic understanding of bounded plasmas, have also appeared in further work in which excitation of these surface waves and resonances provides a mechanism for heating and sustaining plasma discharges. A detailed review of early efforts on resonance-sustained, radio frequency gas discharges is given by Taillet[37]. In this work the enhancement of the RF electric field in a planar capacitively driven discharge is emphasized. A simple model of a collisional homogeneous plasma slab in between two sheath regions in which $n_e = 0$ is developed from previous theoretical work summarized by Vandenplas[13]. Justification for extending the results to inhomogeneous plasmas was based on a variational calculation of Crawford and Kino[38] and cited in Vandenplas[13], which showed that the plasma density could be replaced by the average plasma density in an expression for the internal fields at resonance. Taillet's analysis assumes that the resonance enhanced field strength remains in the linear regime while still providing sufficient electron heating to sustain the plasma. A relation, which equates the ohmic power absorbed by the plasma electrons to the energy lost due to ionization, excitation, and diffusion, characterizes the discharge. It is shown that stable and unstable equilibria exist. Some experimental results given by Taillet[37] include measurement of the plasma electric field using electron beam probing. The electric field is observed to be approximately 10 times greater in magnitude than the vacuum field and the phase of the field in the plasma bulk is opposite to that at the plasma edge. Measurements of the plasma profile deduced from photometric data along with density measurements taken from a Langmuir probe were used to further verify that the discharges were indeed operating at the series resonance. Some effects associated with electronegative gases were also discussed.

Further investigation of resonance sustained discharges was performed by Messiaen and Vandenplas[39]. This work examined the nonlinear behavior of a cylindrical mercury DC discharge plasma inserted across a waveguide operating at 2.7GHz. Several interesting

results were obtained for high incident microwave power. One result was that the plot of reflected power versus density exhibited a broadening of the peaks to include plateau regions indicating a tendency for the plasma to remain in a resonant state. Another result was that for sufficiently high incident power the plasma could be sustained in the absence of the dc current. In this case, the power absorbed was measured to be independent of the incident power. Also the plasma density observed when the discharge was maintained by the incident HF power was found to be nearly the same as that associated with the resonance observed at low incident power (when the plasma was maintained by the DC current). The conclusion is that the plasma is resonance sustained. A final interesting result is that when the incoming field energy is decreased below a certain minimum the plasma jumps to a lower density which was considered to result from coupling to the next higher Tonks-Dattner resonance.

In a later work Messiaen and Vandenplas[40] reported on resonantly sustained rf plasmas in a spherical cavity. For moderate rf power the system was determined to be in a linear resonant state with density far above the critical density (defined by $\omega_{pe}(r_c) = \omega_{rf}$) which is characteristic of a geometric resonance associated with a bounded plasma. The density was found to depend heavily on the frequency and only slightly on the power level of the exciting signal since detuning occurs to maintain the resonant state.

This work on resonance sustained discharges was significantly advanced by Godyak[41]. A homogeneous model for steady-state low pressure rf discharges is developed[42] which is used to predict the total impedance across a discharge gap. This impedance is taken to be the sum of plasma, space-charge sheath, and stochastic (interaction with moving sheath walls) impedances. The total impedance is then used in combination with an energy balance equation to predict the internal properties of the rf discharge including the current-voltage characteristic and the dependence of plasma density, and discharge voltages on applied frequency. This analysis has been extended to the inhomogeneous plasma model which results in the appearance of form factors and scaling factors which do not greatly effect the qualitative behavior[41]. Godyak and Popov[43] conducted an experimental study of resonant discharges to test theoretical predictions. Resonant discharges are maintained at a theoretically predicted minimum applied voltage and resonant frequency. Scaling laws including $n \propto \omega^3$ and $s \propto \omega^{-1}$, where n is the peak plasma density and s is the average sheath thickness, are verified.

The resonantly sustained plasmas that have been discussed so far are generally

confined in space due to their method of excitation (within some cavity or between electrodes). This prompted Moisan to develop a device called a surfatron in which a plasma column is sustained by a traveling surface wave launched from one end[44]. The launcher surrounds a gas filled dielectric tube which contains the plasma. Reported operation occurs over a wide range of neutral gas pressures and electron densities with the length of the plasma being a function of input power. In a more recent work, Moisan and Zakrzewski[2] give a review of the basic theory and various experimental designs for plasma sources based on the propagation of electromagnetic surface waves. Devices operate from a few hundred kHz to ~ 10 GHz with density ranges from 10^{10}cm^{-3} to 10^{13}cm^{-3} , tube radii from 0.5mm to 10cm, and neutral gas pressures from 10^{-5} Torr to a few times atmospheric pressure. The surfatron was the first of these plasma sources and has inspired a great deal of subsequent research in the field.

Early studies of surface wave sustained plasmas focused on describing their axial dependencies. A simple theory, derived by Zakrzewski *et. al.*[45], of the collisional attenuation was obtained by extension of the collisionless theory, and led to a good prediction of axial attenuation of the surface wave fields when plasma density, electron collision frequency, and tube dimensions are provided. Radial dependencies were neglected. Another work by Glaude *et. al.*[46] furthers the analysis of weakly damped surface waves. In this study, a plasma, which is homogeneous in the radial direction, undergoes ohmic heating by the wave fields. After introducing a constant equal to the average energy absorbed per electron (independent of wave power or axial position), and assuming that the power lost at some axial position, z , is equal to the energy absorbed by electrons at that position, it is shown that the plasma density undergoes nearly linear attenuation in the axial direction. This is shown to be in agreement with experiment over the middle portion of the discharge length. Conditions for discharge stability have also been worked out in the thin cylinder approximation (cylinder radius \ll axial wavelength)[47]. This thin cylinder approximation is made in much of the work on surface wave plasmas.

More self-consistent modeling was introduced by Ferreira[48][49] and later by Aliev *et. al.*[50][51]. A first effort[48] in the weak attenuation limit predicted the absolute value and radial profiles for electron density, electron temperature, HF (high frequency) fields, and excited atomic densities as functions of gas pressure, wave frequency, and power absorbed. The equations used include electron and ion continuity, electron and ion momentum transfer with elastic electron-neutral collisions, power balance with local ohmic heating, and surface

wave electric fields which are determined from the homogeneous plasma approximation, which is justified in the thin cylinder approximation since the radially averaged plasma density can be used [7]. To derive the radial electron temperature profile it is assumed that the HF field is locally dissipated (i.e., neglecting heat conduction).

Later Ferreira extends his model to include axial variation [49]. This analysis differs from that of Glaude *et. al.* [46] in that the assumption that wave power absorbed over a given axial length be proportional to the number of electrons in that slice and independent of wave power is unnecessary. This quantity is instead shown to be constant under certain operating conditions. Finally, the model is extended beyond the thin cylinder approximation by accounting explicitly for field boundary conditions with a radial plasma inhomogeneity [52]. Here, the radially inhomogeneous plasma is treated as a cold dielectric and the possibility of local plasma resonances is not considered.

Another model of HF surface wave discharges put forth by Zhelyazkov and Benova [53] includes more carefully the thickness and dielectric constant of the containing vessel which leads to more favorable agreement with experiment. When this model was applied to an analysis of the dipolar ($m=1$) surface mode the interesting result was obtained that a critical value for $\omega R/c$ exists below which no plasma was likely to be sustained. This phenomenon is observed by Margot-Chaker *et. al.* [54] who attribute its cause to a stability criterion [54][55]

In another work by Aliev *et. al.* [56], the axial structure of weakly damped surface wave plasmas in both ambipolar diffusion and volume recombination regimes have been expressed with similarity laws.

Since detailed information on the electron energy distribution function, EEDF, is required to help determine transport properties and rates of atomic processes, there have been several recent efforts to more accurately model the EEDF in surface wave plasmas by solving the electron Boltzmann equation in various limits. All the studies discussed here start by expanding the distribution function in spherical harmonics in v -space and then truncating the series after the first two terms (Lorentz approximation). This is justified when the electron-neutral mean free path is small compared to the spatial scales of the EEDF. The distribution is then written as the sum of a large steady-state term and a small rapidly varying term. The resulting equations are combined to give a solution for the spherically symmetric steady-state portion of the distribution function [57].

An early work by Kortshagen *et. al.* [58] makes the further assumption that the

distribution function may be written as a separate function of space and velocity. This assumption requires sufficiently low plasma densities and sufficiently high gas pressures. The thin cylinder approximation is made so that a uniform (across the radius) axial surface wave field may be imposed, and an ambipolar field is derived from the radial density profile in a diffusion controlled regime. Numerical solutions for argon are given but not compared with experiment. Later work by Kortshagen and Schlüter[59] incorporated a Fokker-Plank term in the electron Boltzmann equation to account for the effect of electron-electron Coulomb collisions. In this work radial inhomogeneity is neglected for simplicity. The maintenance field strength is self-consistently determined by solving a particle balance equation in the thin cylinder approximation. The most noteworthy result is an increasing temperature at low electron energies for an increasing ratio of electron density to neutral density. This result is explained as the removal of a Ramsauer minimum induced dip in the EEDF at low energies. This effect is also discussed by Godyak *et. al.*[5] as an explanation for their experimental results in RF capacitive discharges.

In order to better model low pressure discharges, a non-local approach[60][61] has been adopted where the complete spatially inhomogeneous Boltzmann equation is solved. This is better than the local approach previously discussed because at low pressure an electron heated at a certain position is not converted to an energy gain of the whole distribution at that position[62].

A new electron heating mechanism has been described by Aliev *et. al.*[63] on the basis of a non-local kinetic approach. This mechanism is predicted to play a significant role in the maintenance of discharges at sufficiently low pressures ($\nu < \omega$ where ν is the total electron collision frequency and ω is the surface wave frequency). In a first calculation[63], the existence of a region of enhanced radial electric field near the column boundary, at the radius at which the local plasma frequency equals the applied frequency, is imposed as an approximation to the self consistent fields. The location of the enhanced field is assumed far enough from the sheath and of large enough spatial extent that the thickness of the sheath may be neglected and that a specular reflection approximation can be made. This enhanced field then undergoes a Cherenkov particle-wave interaction with the electrons passing through it. The heating term results from a quasi-linear term given by the period averaged product of the radially enhanced field and the v-space gradient of the perturbed distribution function. The result is the generation of a hot tail in the EEDF.

This early work was followed by a self-consistent calculation[64][65] which included

a set of fluid equations for ion motion, the surface wave electric field equations, and a self-consistent ambipolar field. The enhanced radial field is then self-consistently computed. The spatially inhomogeneous Boltzmann equation is then solved in the non-local approximation to give the EEDF. Numerical results for mean power absorbed per electron due to ohmic and collisionless (quasi-linear) heating are given under varying discharge conditions.

The effect of the enhanced radial field in the limit of small electron mean free paths (compared to spatial scale of the enhanced field) has also been studied[66]. The equations of hydrodynamics are used to determine radial temperature profiles for both electrons and ions. Here the energy gain in the resonance region results in an increase in the bulk part of the EEDF rather than in a hot tail region.

The effects of collisionless (quasi-linear) heating on the axial structure of surface wave plasmas has also been investigated[67][68][69] with pronounced effects on the axial plasma profile resulting at the ends of the discharge column. Surface waves damped primarily through quasi-linear heating of the electrons at the end of a column discharge are shown to decay linearly rather than exponentially along the propagation direction[70].

In addition to the traveling surface wave sustained cylindrical discharges discussed so far there has been an effort to develop standing and planar surface wave sustained plasmas. Some motivation for this effort comes from a desired plasma uniformity which can be of use in laser sources and materials processing applications. Rakem *et. al.*[71] make a comparison between a simple model and experiment[72] on a cylindrical standing surface wave plasma where the far end of the column is shorted. For lengths less than some limit, the density remains nearly constant (with some modulation due to the standing wave fields). An argon ion laser was built based on this structure.

Nonaka[73] reports on new devices similar to the surfatron but with varying cross-sections of which a rectangular one is of particular interest. A large area (up to 0.73m x 1.72m) plasma is produced. Later analysis[74] of this planar surface wave source led to determination of the axial density gradient in diffusion and recombination dominated regimes and the electrostatic mode structure. The axial density gradient is predicted to be less than in the cylindrical case.

Another planar microwave surface wave device consists of a dielectric wave guide (18cm x 30cm) bound by metal and plasma on either side with a vacuum gap between the dielectric and the plasma[75]. Microwave energy is fed into the dielectric waveguide, and the fringing fields couple to and sustain the plasma. In the directions aligned with the

plane of the dielectric, the plasma density is modulated about a nearly constant value by the standing waves. In the perpendicular (to the dielectric) direction the measured electron density rapidly decays. A simple model is presented based on a homogeneous plasma.

This concludes our review of past and present research on high frequency electron surface waves and resonances primarily in dielectric bounded plasmas. In the following chapters, we present a study, based on particle-in-cell simulation, of the nature of these waves in metal bound plasmas and their application to sustaining plasma discharges.

An outline of this work is as follows. In Chapter 2 we initiate our study of waves in the metal bound slab using a matrix sheath model. A linearized Vlasov treatment for this model is derived and compared to simulation. Next a more realistic model for the plasma and sheath is developed in Chapter 3. The result is the identification of a new set of surface modes which exist only in the non-uniform, thermal, bounded plasma. We then move from the study of surface wave characteristics to a study of surface wave sustained discharges. In Chapter 4 we consider the 1d3v plasma which is sustained at the series resonance frequency (which will be shown to be the cut-off frequency for the main asymmetric surface wave). Results including the scaling of plasma density and sheath width with frequency, discharge gap impedances, electron energy distributions and heating profiles will be given and compared with theory. The 2d3v surface wave sustained slab will be treated in Chapter 5. The 2d3v surface waves are excited in an asymmetric and hybrid fashion with different current loop antennae configurations. Comparisons are made between simulation results and theoretical predictions for the wave dispersion relations and eigenfunctions.

Chapter 6

Suggestions for Future Research

It is my hope that the work presented here will inspire future research in the area of high frequency surface wave sustained plasmas, including further modeling efforts as well as laboratory based experiments. Future simulation may be aimed at extending the results presented here to higher frequencies, higher plasma densities, larger volumes, and to the many different gases used in plasma processing. This will require more refined computational techniques and greater computing power along with development of a collision model for each new gas-phase chemistry. Of particular interest would be an understanding of the maximum attainable plasma densities, and the EEDFs and uniformity of the plasmas at these densities.

The development of an analytic model which might predict the EEDFs and electron cooling effects observed here would also be of particular interest. It is believed that a solution to the inhomogeneous Boltzmann equation in a non-local limit (at low gas pressures) may lead to the desired results. It is suggested that further simulation be used to help validate such a model.

Finally there is a wealth of laboratory work to be performed based on the encouraging simulation results presented here. An investigation of surface wave launching schemes which are able to sustain uniform plasmas over large areas is of particular interest. Both slow and fast wave coupling should be investigated. Also metal and dielectric bound plasmas might be considered.

Bibliography

- [1] C. K. Birdsall. Particle-in-cell charged-particle simulations, plus monte carlo collisions with neutral atoms, pic-mcc. *IEEE Transactions on Plasma Science*, 19(2):65, 1991.
- [2] M. Moisan and Z. Zakrzewski. Plasma sources based on the propagation of electromagnetic surface waves. *J. Phys. D: Appl. Phys.*, 24:1025, 1991.
- [3] C. K. Birdsall and A. B Langdon. *Plasma Physics Via Computer Simulation*. (Adam Hilger, Bristol, England, 1991).
- [4] V. Vahedi and M. Surendra. A monte carlo collision model for the particle-in-cell method: applications to argon and oxygen discharges. *Comp. Phys. Comm.*, 87:179, 1995.
- [5] V. A. Godyak, R. B. Piejak, and B. M. Alexandrovich. Measurements of electron energy distribution in low-pressure rf discharges. *Plasma Sources, Science and Technology*, 1(1):36, 1992.
- [6] V. Vahedi, C.K. Birdsall, M.A. Lieberman, G. DiPeso, and T.D. Rognlien. Capacitive rf discharges modelled by particle-in-cell monte carlo simulation. ii. comparisons with laboratory measurements of electron energy distribution functions. *Plasma Sources, Science and Technology*, 2(4):273-8, Nov. 1993.
- [7] A. W. Trivelpiece. *Slow-Wave Propagation in Plasma Wave Guides*. (San Francisco Press, Inc., San Francisco, 1967).
- [8] M. A. Lieberman and A. J. Lichtenberg. *Principles of Plasma Discharges and Materials Processing*. Wiley, New York, 1994.
- [9] L. Tonks. The high frequency behavior of a plasma. *Phys. Rev.*, 37:1458, 1931.

- [10] L. Tonks. Plasma-electron resonance, plasma resonance and plasma shape. *Phys. Rev.*, 38:1219, 1931.
- [11] N. Herlofson. *Arkiv Fysik*, 3:247, 1951.
- [12] A Dattner. Resonance densities in a cylindrical plasma column. *Phys. Rev. Letters*, 10(6):205, 1963.
- [13] Paul E. Vandenplas. *Electron waves and resonances in bounded plasmas*. (Interscience Publishers, New York, 1968).
- [14] J. C. Nickel, J. V. Parker, and R. W. Gould. Resonance oscillations in a hot nonuniform plasma. *Physical Review Letters*, 11(5):183, September 1963.
- [15] J. V. Parker, J. C. Nickel, and R. W. Gould. Resonance oscillations in a hot nonuniform plasma. *Phys. Fluids*, 7:1489, 1964.
- [16] P. Weissglas. Resonance oscillations in a hot nonuniform plasma. *Phys. Rev. Letters*, 10(6):206, 1963.
- [17] L. Tonks and I. Langmuir. A general theory of the plasma of an arc. *Phys. Rev.*, 34:876, 1929.
- [18] M. Gaigneaux and P. E. Vandenplas. Temperature (tonks-dattner) resonances theoretically revisited: New temperature and density diagnostics. *Phys. Fluids*, 29(5):1472, 1986.
- [19] D. E. Baldwin. Kinetic model of tonks-dattner resonances in plasma columns. *Phys. Fluids*, 12(2):279, 1969.
- [20] D. E. Baldwin and J. L. Hirshfield. Kinetic model of tonks-dattner resonances in a positive column. *Applied Phys. Letters*, 11(6):175, 1967.
- [21] D. W. Ignat. Experimental test of a kinetic theory of tonks-dattner resonances. *Phys. Fluids*, 13(7):1771, 1970.
- [22] R. W. Gould. Radio frequency characteristics of the plasma sheath. *Physics Letters*, 11(3):236, 1964.

- [23] R. S. Harp and F. W. Crawford. Characteristics of the plasma resonance probe. *Journal of Applied Physics*, 35(12):3436, 1964.
- [24] A. W. Trivelpiece and R. W. Gould. Space charge waves in cylindrical plasma columns. *J. Appl. Phys.*, 30:1784, 1959.
- [25] M. Moisan, A. Shivarova, and A. W. Trivelpiece. Review article: Experimental investigations of the propagation of surface waves along a plasma column. *Plasma Physics*, 24(11):1331, 1982.
- [26] A. Shivarova and I. Zhelyazkov. Chapter 12: Surface waves in gas-discharge plasmas. In A. D. Boardman, editor, *Electromagnetic Surface Modes*, page 465. John Wiley & Sons Ltd., New York, 1982.
- [27] V. K. Decyk. *Computer Simulation Study of Waves in Bounded Plasma with Application to Lower Hybrid Heating*. PhD thesis, University of California at Los Angeles, November 1977.
- [28] V. K. Decyk and J. M. Dawson. Computer model for bounded plasma. *Journal of Computational Physics*, 30:407, 1979.
- [29] C. C. Cheng and E. G. Harris. Waves and instabilities in a finite plasma. *Phys. Fluids*, 12(6):1262, 1968.
- [30] B. O'Brien, R. W. Gould, and J. Parker. Longitudinal wave-propagation modes along a positive column. *Phys. Rev. Letters*, 14(16):630, 1965.
- [31] B. B. O'Brien Jr. Slow wave transmission modes of an isotropic inhomogeneous cylindrical hot plasma. *Plasma Physics*, 9:369, 1967.
- [32] B. Kerzar, K. Abrahamsen, and P. Weissglas. Nonlinear plasma wave interaction in an arc discharge. *Applied Physics Letters*, 7(6):155, 1965.
- [33] B. Kerzar and P. Weissglas. Plasma microwave interaction. *Journal of Applied Physics*, 36(8):2479, 1965.
- [34] V. Atanassov, I. Zhelyazkov, A. Shivarova, and Zh. Genchev. Kinetic theory of surface wave propagation along a hot plasma column. *Journal Plasma Physics*, 16(1):47, 1976.

- [35] A. Dengra and J. Ballesteros. Surface-wave-particle interactions in a cylindrical plasma. *Journal Plasma Physics*, 47(part S):389, 1992.
- [36] O. M. gradov and L. Stenflo. Linear theory of a cold bounded plasma. *Physics Reports*, 94(3):111, 1983. Review Section of Physics Letters.
- [37] J. Taillet. Resonance-sustained radio frequency discharges. *Amer. J. Phys.*, 37(4):423, 1969.
- [38] F. W. Crawford and G. S. Kino. *Compt. Rend. Acad. Sci.*, 256:1939, 1963.
- [39] A. M. Messiaen and P. E. Vandenplas. Nonlinear resonance effect at high power in a cylindrical plasma. *Physics Letters*, 25A(4):339, 1967.
- [40] A. M. Messiaen and P. E. Vandenplas. Resonantly sustained bounded radiofrequency plasma in a spherical cavity. *Applied Physics Letters*, 15(1):30, 1969.
- [41] V. A. Godyak. *Soviet RF Discharge Research*. Delphic Assoc., 1986.
- [42] V. A. Godyak. Steady-state low-pressure rf discharges. *Soviet Journal of Plasma Physics*, 2(1):78, January-February 1976.
- [43] V. A. Godyak and O. A. Popov. Experimental study of resonant rf discharges. *Soviet Journal of Plasma Physics*, 5(2):227, March-April 1979.
- [44] M. Moisan, C. Beaudry, and P. Leprince. A small microwave plasma source for long column production without magnetic field. *IEEE Transactions on Plasma Science*, PS-3(2):55, 1975.
- [45] Z. Zakrzewski, M. Moisan, V. M. M. Glaude, C. Beaudry, and P. Leprince. Attenuation of a surface wave in an unmagnetized rf plasma column. *Plasma Physics*, 19(2):77, 1977.
- [46] V. M. M. Glaude, M. Moisan, and R. Pantel. Axial electron density and wave power distributions along a plasma column sustained by the propagation of a surface microwave. *J. Appl. Phys.*, 51(11):5693, 1980.
- [47] Zenon Zakrzewski. Conditions of existence and axial structure of long microwave discharges sustained by travelling waves. *Journal Physics D: Applied Physics*, 16:171, 1983.

- [48] C. M. Ferreira. Theory of plasma column sustained by a surface wave. *Journal Physics D: Applied Physics*, 14:1811, 1981.
- [49] C. M. Ferreira. Modelling of a low-pressure plasma column sustained by a surface wave. *Journal Physics D: Applied Physics*, 16:1673, 1983.
- [50] Yu. M. Aliev, A. G. Boev, and A. P. Shivarova. On the non-linear theory of a long gas discharge produced by an ionizing slow electromagnetic wave. *Physics Letters*, 92(5):235, 1982.
- [51] Yu. M. Aliev, A. G. Boev, and A. P. Shivarova. Slow ionising high-frequency electromagnetic wave along a thin plasma column. *Journal Physics D: Applied Physics*, 17:2233, 1984.
- [52] A. B. Sa, C. M. Ferreira, S. Pasquiers, C. Boisse-Laporte, P. Leprince, and J. Marec. Self-consistent modeling of surface wave produced discharges at low pressures. *Journal Applied Physics*, 70(8):4147, 1991.
- [53] I. Zhelyazkov and E. Benova. Modeling of a plasma column produced and sustained by a traveling electromagnetic surface wave. *J. Appl. Phys.*, 66(4):1641, 1989.
- [54] J. Margot-Chaker, M. Moisan, M. Chaker, V. M. M. Glaude, P. Lauque, J. Paraszczak, and G. Sauvè. Tube diameter and wave frequency limitations when using the electromagnetic surface wave in the $m=1$ (dipolar) mode to sustain a plasma column. *Journal Applied Physics*, 66(9):4134, 1989.
- [55] E. Benova, I. Ghanashev, and I. Zhelyazkov. Theoretical study of a plasma column sustained by an electromagnetic surface wave in the dipolar mode. *Journal Plasma Physics*, 45(2):137, 1991.
- [56] Yu. M. Aliev, K. M. Ivanova, M. Moisan, and A. P. Shivarova. Analytical expressions for the axial structure of surface waves sustained plasmas under various regimes of charged particle loss. *Plasma Sources Sci. Technol.*, 2(3):145, 1993.
- [57] I.P. Shkarofsky, T. W. Johnston, and M. P. Bachynski. *The Particle Kinetics of Plasmas*. Addison-Wesley, Reading, MA, 1966.

- [58] U. Kortshagen, H. Schlüter, and A. Shivarova. Determination of electron energy distribution functions in surface wave produced plasmas: I. modelling. *Journal Physics D: Applied Physics*, 24, 1571 1991.
- [59] U. Kortshagen and H. Schlüter. On the influence of coulomb collisions on the electron energy distribution function of surface wave produced argon plasmas. *Journal Physics D: Applied Physics*, 25:644, 1992.
- [60] Ira B. Bernstein and T. Holstein. Electron energy distributions in stationary discharges. *Physical Review*, 94(6):1475, 1954.
- [61] L. D. Tsendin. Energy distribution of electrons in a weakly ionized current-carrying plasma with a transverse inhomogeneity. *Soviet Physics-JETP*, 39(5):805, 1974.
- [62] U. Kortshagen. A non-local kinetic model applied to microwave produced plasmas in cylindrical geometry. *Journal Physics D: Applied Physics*, 26:1691, 1993.
- [63] Yu. M. Aliev, A. V. Maximov V. Yu. Bychenkov, and H. Schlüter. High energy electron generation in surface-wave-produced plasmas. *Plasma Sources Sci. Technol.*, 1:126, 1992.
- [64] Yu. M. Aliev, A. V. Maximov, U. Kortshagen, H. Schlüter, and A. Shivarova. Modeling of microwave discharges in the presence of plasma resonances. *Physical Review E*, 51(6):6091, 1995.
- [65] H. Schlüter. *Microwave Plasma and Its Applications*, chapter Surface Wave Sustained Microwave Discharges in the Presence of Plasma Resonances. The Moscow Physical Society, 1995.
- [66] Yu. M. Aliev, A. V. Maximov, and H. Schlüter. The influence of the plasma resonance heating on the maintenance of surface wave produced discharges. *Physica Scripta*, 48:464, 1993.
- [67] Yu. M. Aliev, A. V. Maximov, H. Schlüter, and A. Shivarova. Axial structure of surface-wave-sustained discharges influenced by local plasma resonances. *J. Plasma Physics*, 52(2):321, 1994.
- [68] Yu. M. Aliev and A. V. Maximov. On the axial structure of surface wave sustained discharges. *Physica Scripta*, 51:257, 1995.

- [69] Yu. M. Aliev, J. Berndt, H. Schlüter, and A. Shivarova. Numerical calculations on surface wave propagation in longitudinally non-uniform plasmas. *Plasma Physics Controlled Fusion*, 36:937, 1994.
- [70] Yu. M. Aliev. *Microwave Discharges: Fundamentals and Applications*, volume 302 of *NATO Advanced Study Institute, Series B: Physics*, chapter Some Aspects of Nonlinear Theory of Ionizing Surface Plasma Waves, page 105. Plenum Press, New York, 1993.
- [71] Z. Rakem, P. Leprince, and J. Marec. Modelling of a microwave discharge created by a standing surface wave. *Journal Physics D: Applied Physics*, 25:953, 1992.
- [72] Z. Rakem, P. Leprince, and J. Marec. Characteristics of a surface wave produced discharge operating under standing wave conditions. *Revue Phys. Appl.*, 25:125, 1990.
- [73] Shigehiko Nonaka. Proposal of non-cylindrical and large-area rf plasma productions by surface wave. *Journal of the Physical Society of Japan*, 63(8):3185, 1994.
- [74] Shigehiko Nonaka. The axial gradient of planar rf plasmas produced by a surface wave. *Journal Physics D: Applied Physics*, 28:1058, 1995.
- [75] K. Komachi and S. Kobayashi. Generation of a microwave plasma using traveling waves. *Journal of Microwave Power and Electromagnetic Energy*, 24(3):140, 1989.

Electron surface waves in a plasma slab with uniform ion density

D. J. Cooperberg

Department of Electrical Engineering and Computer Science, University of California, Berkeley, California 94720

(Received 15 July 1997; accepted 13 January 1998)

Electron surface waves in a metal bound plasma slab have been detected and analyzed. In this work it is shown that the presence of a matrix sheath between the central quasineutral region and the metal walls allows for the propagation of surface waves analogous to those found in dielectric bound plasmas. Measurements of the dispersion relations and eigenfunctions of asymmetric and symmetric, electrostatic, surface, and body waves are made via particle-in-cell simulation of a plasma slab with sheaths. The plasma slab has finite temperature electrons and fixed ions of uniform density. The sheaths consist of electron free, fixed, uniform ion regions ("matrix sheath") of thickness $\sim \lambda_{De}$. A linearized Vlasov theory is developed for comparison with the simulation. It is shown that the long wavelength approximation ($k\lambda_{De} \ll 1$) is not valid even for long wavelengths in the propagation direction. Collisionless damping of both surface and body waves is measured which compares well with theoretical estimates. © 1998 American Institute of Physics. [S1070-664X(98)03804-X]

I. INTRODUCTION

Surface waves on dielectric (glass) bounded cylindrical plasmas, known as Gould-Trivelpiece waves have been well studied^{1,2} and are well characterized. Surface waves have also been studied in dielectric bounded plasma slabs by computer simulation.³ Surface waves in dielectric bound plasmas are a continuing area of research in the field of high frequency discharges where these waves are driven to sustain plasma columns.⁴ In past treatments, the effect of the plasma sheath is typically neglected on the basis that the sheath scale length, λ_{De} , is much less than the typical scale length (depth of penetration) of the surface wave.

In this work we will demonstrate that the sheath region between plasma and a metal boundary can itself provide the means for surface wave propagation. We shall refer to these waves as "sheath waves" to emphasize the importance of the sheath. It is hoped that this investigation may lead to a better understanding of sheath physics and to applications, such as bulk plasma control via sheath mode excitation.

The structure of this paper is as follows. In Sec. II we describe the system which is the subject of our theoretical and experimental studies. Our experimental results are produced by particle-in-cell simulation⁵ which is fully capable of capturing the kinetic behavior of the $2d3v$ (two spatial and three velocity components) bounded plasma since it operates from first principles (i.e., solving Poisson's equation, and particle equations of motions). In Sec. III we will develop a kinetic theory for sheath waves. In Sec. IV simulation results are presented and compared with theory. Conclusions are made in Sec. V.

II. MODEL DESCRIPTION

A plasma slab model is used to study "sheath" waves in metal bounded plasmas. We allow for two spatial dimensions and three velocity dimensions. The absence of a means to

scatter energy into or out of the third velocity dimension will have no effect on our results. The model includes a wall to wall uniform, immobile, neutralizing background of ions, and thermal electrons loaded in the central region (Fig. 1). The positively charged sheaths which exist between the quasineutral plasma bulk and the grounded metal boundaries are modeled as electron free regions ("the matrix sheath" approximation). These sheaths are of thickness Δ , chosen to be on the order of a few electron Debye lengths; they are maintained by specular reflection of electrons at the distance, Δ , from the walls. This model provides a detailed comparison of $\omega(k_y) = \omega_r(k_y) + i\omega_i(k_y)$ and eigenfunctions in \hat{x} as measured in simulation and calculated from the linearized Vlasov equation.

III. LINEAR KINETIC THEORY

The kinetic theory presented here draws on the work of Xu *et al.*⁶ who adapted the work of Cheng and Harris⁷ (in which surface waves in a plasma slab bound by vacuum were described) to include the presence of conducting walls and positively charged sheath regions. We shall show that a key approximation made by Xu has limited applicability and also correct an algebraic error which appeared in his final result for $\omega(k_y)$. New results for the imaginary part of the dispersion resulting from Landau damping are presented.

As described above, the static sheaths of thickness Δ are modeled as fixed, uniform ion layers with no electrons. The sheaths are maintained by reflecting incident electrons back into the bulk plasma. We shall see that the presence of this sheath layer allows a contrast with the Gould-Trivelpiece¹ model for modes in a dielectric lined waveguide. We may also contrast our work with that of Decyk,³ who worked with a fluid model in which $\Delta \rightarrow \infty$.

Combining the linearized Vlasov equation for the electrons with the linearized Poisson's equation enables the deri-

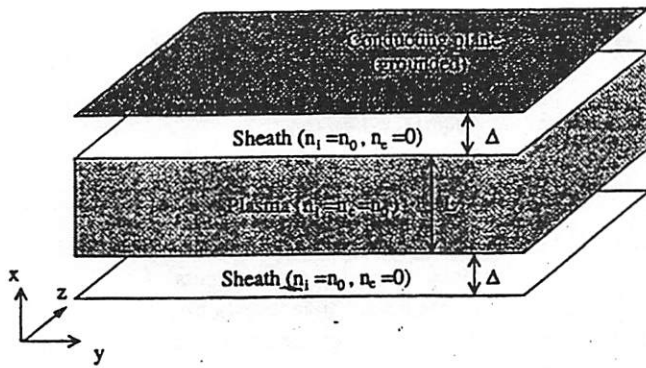


FIG. 1. Schematic of plasma slab simulation.

vation of electrostatic sheath wave dispersion relations and the eigenfunctions describing these waves. The quasistatic limit is justified since the slow-wave results we will obtain contain wavelengths much shorter than those in free space at the same frequency; also, the dominant energies are kinetic and electric. We assume herein that wave quantities may be written as $\Phi(\mathbf{r}, t) = \phi(x)e^{i(k_y y - \omega t)}$, with k_y real. We write the governing equations for the perturbed quantities as:

$$\frac{\partial f(\mathbf{r}, \mathbf{v}, t)}{\partial t} + \mathbf{v} \cdot \frac{\partial f(\mathbf{r}, \mathbf{v}, t)}{\partial \mathbf{r}} + \frac{e}{m} \nabla \Phi(\mathbf{r}, t) \cdot \frac{\partial F_m(\mathbf{v})}{\partial \mathbf{v}} = 0, \tag{1}$$

$$F_m = n(\mathbf{r}) \left(\frac{m_e}{2\pi k T_e} \right)^{\frac{3}{2}} e^{-\frac{m_e \mathbf{v}^2}{2kT_e}}, \tag{2}$$

$$\nabla^2 \Phi^p(\mathbf{r}, t) = \frac{e}{\epsilon_0} \int f d^3 v, \tag{3}$$

where e and m are the electron charge and mass, respectively, F_m is an equilibrium Maxwellian velocity distribution, and Φ^p is the particular solution to Poisson's equation. The full expression for the perturbed potential is $\Phi = \Phi^p + \Phi^h$. The zero-order steady-state potential which results from the ion rich "matrix" sheaths plays no role in what follows and need not be discussed further. Boundary conditions for the potential are $\Phi(x=0, y, t) = \Phi(x=L+2\Delta, y, t) = 0$ (external short circuit). It is further required that Φ and $\partial\Phi/\partial x$ be continuous at the sheath edges, $x = \Delta$, and $x = L + \Delta$. For the electron distribution, specular reflection leads to the conditions

$$f(x = \Delta, y, v_x, v_y, v_z, t) = f(x = \Delta, y - v_x, v_y, v_z, t), \tag{4}$$

$$f(x = L + \Delta, y, v_x, v_y, v_z, t) = f(x = L + \Delta, y - v_x, v_y, v_z, t). \tag{5}$$

To proceed, we assume the following forms of $\phi(x)$ within our system,

$$\phi(x) = A \sinh(k_y x), \quad 0 < x < \Delta, \tag{6}$$

$$\begin{aligned} \phi(x) &= B e^{-k_y(x-\Delta)} + C e^{-k_y(L+\Delta-x)} \\ &+ \sum_{k_x = n\pi/L=0}^{\infty} a(k_x) \cos(k_x(x-\Delta)), \end{aligned}$$

$$\Delta < x < L + \Delta \tag{7}$$

$$\phi(x) = D \sinh(k_y(L+2\Delta-x)), \quad L + \Delta < x < L + 2\Delta. \tag{8}$$

In the central region, $\Delta < x < L + \Delta$, we have used

$$\phi^p(x) = \sum_{k_x = n\pi/L}^{\infty} a(k_x) \cos(k_x(x-\Delta)), \tag{9}$$

where the $k_x = 0$ term must be multiplied by 0.5. This choice is valid because of the specular reflecting boundary condition which allows us to continue ϕ^p as an even function about $x = \Delta$ and $x = L + \Delta$. The justification is that there can be no distinction between a particle with $x > \Delta$ approaching $x = \Delta$ ($v_x < 0$) and a "pseudoparticle" with $x < \Delta$ approaching $x = \Delta$ with $v_x > 0$. The "pseudoparticle" will be incarnated as the reflected original particle once it crosses $x = \Delta$. A similar argument holds for $x = L + \Delta$.

Next we express the full solution in the central region ($\Delta < x < L + \Delta$) as

$$\phi(x) = \sum_{k_x = n\pi/L}^{\infty} \phi(k_x) \cos(k_x(x-\Delta)), \tag{10}$$

where

$$\begin{aligned} \phi(k_x) &= a(k_x) + \frac{2k_y}{Lk^2} [1 - e^{-k_y L} \cos(k_x L)] \\ &\times [B + C \cos(k_x L)]. \end{aligned} \tag{11}$$

We proceed as in Ref. 7 by solving for the perturbed distribution function, $f(\mathbf{r}, \mathbf{v}, t)$, by integrating over the unperturbed orbits. Substituting Eq. (1) into the expression for the total time derivative of $f(\mathbf{r}, \mathbf{v}, t)$ produces,

$$\begin{aligned} \frac{Df(\mathbf{r}, \mathbf{v}, t)}{Dt} &= \frac{\partial f(\mathbf{r}, \mathbf{v}, t)}{\partial t} + \mathbf{v} \cdot \frac{\partial f(\mathbf{r}, \mathbf{v}, t)}{\partial \mathbf{r}} + \frac{e}{m} \nabla \Phi(\mathbf{r}, t) \\ &\cdot \frac{\partial f(\mathbf{r}, \mathbf{v}, t)}{\partial \mathbf{v}} \\ &= -\frac{e}{m} \nabla \Phi(\mathbf{r}, t) \cdot \frac{\partial F_m(\mathbf{v})}{\partial \mathbf{v}} \\ &+ \frac{e}{m} \nabla \Phi^0(\mathbf{r}) \cdot \frac{\partial f(\mathbf{r}, \mathbf{v}, t)}{\partial \mathbf{v}}. \end{aligned} \tag{12}$$

Here $\Phi^0(\mathbf{r})$ is the steady-state potential of the central, quasineutral region, and $\nabla \Phi^0(\mathbf{r}) = 0$. Second-order terms have been dropped. If we assume the modes we are looking for are damped [i.e., $\text{Im}(\omega) < 0$], then we can integrate Eq. (12),

$$\int_t^\infty dt' \frac{Df(\mathbf{r}'(\mathbf{r}, \mathbf{v}, t'), \mathbf{v}'(\mathbf{r}, \mathbf{v}, t'), t')}{D\mathbf{r}'} = f(\mathbf{r}, \mathbf{v}, \infty) - f(\mathbf{r}, \mathbf{v}, t) = - \int_t^\infty dt' \frac{e}{m} \nabla \Phi(\mathbf{r}'(\mathbf{r}, \mathbf{v}, t'), t') \cdot \frac{\partial F_m(\mathbf{v}'(\mathbf{r}, \mathbf{v}, t'))}{\partial \mathbf{v}} \quad (13)$$

Here $\mathbf{r}'(\mathbf{r}, \mathbf{v}, t')$ and $\mathbf{v}'(\mathbf{r}, \mathbf{v}, t')$ are the unperturbed trajectories and take the values \mathbf{r} and \mathbf{v} , respectively at time $t'=t$. For specular reflection of electrons at $x=\Delta$ and $x=L+\Delta$ and no other forces we can write,

$$x'(\mathbf{r}, \mathbf{v}, t') = x'(x, v_x, t'), \quad (14)$$

$$y'(\mathbf{r}, \mathbf{v}, t') = y + v_y(t' - t), \quad (15)$$

$$v'_x(\mathbf{r}, \mathbf{v}, t') = \pm v_x, \quad (16)$$

$$v'_y(\mathbf{r}, \mathbf{v}, t') = v_y, \quad (17)$$

$$v'_z(\mathbf{r}, \mathbf{v}, t') = v_z, \quad (18)$$

where $x'(x, v_x, t')$ is the integral of v'_x . We further simplify Eq. (13) by noting that $f(\mathbf{r}, \mathbf{v}, \infty) \rightarrow 0$ for damped waves. After substituting Eqs. (2), (10), and (14)–(18) into Eq. (13), we have

$$f(\mathbf{r}, \mathbf{v}, t) = - \frac{m_e}{kT_e} \int_t^\infty dt' \frac{e}{m} \sum_{k_x=n\pi/L}^\infty \phi(k_x) e^{i(k_y y' - \omega t')} \quad (19)$$

$$f(\mathbf{r}, \mathbf{v}, t) = \frac{e}{kT_e} \phi(k_x) e^{i(k_y y - \omega t)} \sum_{k_x=n\pi/L}^\infty \frac{F_m(v)}{(w - k_y v_y + k_x v_x)(w - k_y v_y - k_x v_x)} [\cos(k_x(x - \Delta))(k_y^2 v_y^2 - k_y v_y w - k_x^2 v_x^2) + i \sin(k_x(x - \Delta))(k_x k_y v_x v_y - k_x v_x w - k_y v_y k_x v_x)]. \quad (25)$$

In order to obtain the dispersion relation, we may now substitute Eq. (25) into Poisson's equation (Eq. 3) and integrate over velocity space. Before doing so, we note that the denominator of Eq. (25) is an even function of v_x , as is $F_m(|v'|)$, and we may drop odd terms in v_x since they will not contribute to the integral. Poisson's equation, after some algebra, then reduces to

$$(k_x^2 + k_y^2) a(k_x) = \frac{e^2}{\epsilon_0 k T_e} \phi(k_x) \int d^3 v \frac{(\mathbf{k} \cdot \mathbf{v}) F_m(v)}{w - \mathbf{k} \cdot \mathbf{v}}, \quad (26)$$

where we have used Eq. (9) for ϕ^p . The now recognizable integral may be evaluated quickly. The result is

$$a(k_x) = - \phi(k_x) \frac{2w_{pe}^2}{v_{Te}^2} \frac{1}{k^2} (1 + \zeta Z(\zeta)) = \phi(k_x) (1 - \epsilon(w, \mathbf{k})), \quad (27)$$

where $\zeta = \omega/|k| \sqrt{m_e/2kT_e}$, $\omega_{pe} = \sqrt{n e^2 / \epsilon_0 m_e}$, v_{Te} and

$$F_m(\mathbf{v}'(\mathbf{r}, \mathbf{v}, t')) (-k_x v'_x \sin(k_x(x' - \Delta)) + i k_y v'_y \times \cos(k_x(x' - \Delta))). \quad (20)$$

We need to evaluate terms which include the factors $\cos(k_x(x'(x, v_x, t') - \Delta))$ and $v'_x \sin(k_x(x'(x, v_x, t') - \Delta))$. The utility of expressing $\phi(x)$ as a cosine series⁷ is demonstrated when it is observed that

$$\cos(k_x(x'(x, v_x, t') - \Delta)) = \cos(k_x((x - v_x(t - t')) - \Delta)) \quad (21)$$

$$v'_x \sin(k_x(x', (x, v_x, t') - \Delta)) = v_x \sin(k_x((x - v_x(t - t')) - \Delta)). \quad (22)$$

With Eqs. (21) and (22), making the variable change $t'' = t' - t$, we have

$$f(\mathbf{r}, \mathbf{v}, t) = - \frac{e}{kT_e} \phi(k_x) e^{i(k_y y - \omega t)} \times \sum_{k_x=n\pi/L}^\infty \int_0^\infty dt'' e^{i(k_y v_y t'' - \omega t'')} \quad (23)$$

$$F_m(v) (-k_x v_x \sin(k_x((x + v_x t'') - \Delta)) + i k_y v_y \cos(k_x((x + v_x t'') - \Delta))), \quad (24)$$

where we have taken advantage of the fact that $F_m(\mathbf{v}') = F_m(|v'|)$. The integral may be evaluated with the solution for $f(\mathbf{r}, \mathbf{v}, t)$ being

$= \sqrt{2kT_e/m_e}$, $Z(\zeta)$ is the plasma dispersion function, and $\epsilon(\omega, k)$ is the dielectric constant for an infinite warm plasma, given by

$$\epsilon(\omega, \mathbf{k}) = 1 + \frac{2w_{pe}^2}{k^2 v_{Te}^2} [1 + \zeta Z(\zeta)]. \quad (28)$$

Next we enforce the boundary conditions, $\phi(x)$ and $(\partial\phi(x)/\partial x)$ continuous at $x=\Delta$ and $x=L+\Delta$. We start by inserting Eq. (11) into Eq. (27), with the result,

$$\phi(k_x) = \frac{2k_y}{Lk^2 \epsilon(w, \mathbf{k})} [1 - e^{-k_y L} \cos(k_x L)] \times [B + C \cos(k_x L)], \quad (29)$$

going into Eq. (7), the expression for ϕ in the center region. Four equations in four unknowns, A , B , C , and D result from enforcement of the boundary conditions. With Eqs. (6) and (8), the sheath solutions, we find

$$B = \pm C, \quad (30)$$

and

$D(w, k)$

$$= \lim_{\delta \rightarrow 0} \left(ky \tanh(k_y \Delta) \sum_{k_x = n\pi/L}^{\infty} \frac{2k [1 \pm \cos(k_x L)]}{L k^2 \epsilon(w, k)} k_x \right. \\ \left. \times \sin(k_x \delta) + \sum_{k_x = n\pi/L}^{\infty} \frac{2k_y [1 \pm \cos(k_x L)]}{L k^2 \epsilon(w, k)} \cos(k_x \delta) \right). \quad (31)$$

In Eq. (31) we may not pull the limit inside the sums on the right-hand side as has been done elsewhere.⁷ Instead, we must evaluate the sums and then take the limit. In doing so, we are aided by the fact that each summand approaches 0 as $k_x \rightarrow \infty$. This can be seen by examining the form of $\epsilon(k, \omega)$ as $k_x \rightarrow \infty$. In order to evaluate the first term, we take advantage of the fact that $\lim_{\delta \rightarrow 0} \sum_{k_x = n\pi/L}^{\infty} s(k_x) \sin(k_x \delta) = \lim_{\delta \rightarrow 0} \sum_{k_x = n\pi/L = m\pi/L}^{\infty} s(k_x) \sin(k_x \delta)$, where m is an arbitrarily large integer. We can then replace $\epsilon(k, \omega)$ with its asymptotic form as $k_x \rightarrow \infty$. A similar argument for the second term shows that we can truncate that sum at some finite upper bound which allows us to evaluate the limit. The final result for the dispersion relation is

$$D(w, k) = \tanh(k_y \delta) + \frac{2k_y}{L} \sum_{k_x = n\pi/L = -\infty}^{\infty} \frac{1}{k^2 \epsilon(w, k)} = 0. \quad (32)$$

We have used the fact that $\epsilon(\omega, k)$ is an even function of k_x .

A. The limit $|k|\lambda_{De} \ll 1$

In the long wavelength limit, $k\lambda_{De} \ll 1$, which we will show later to be of questionable validity, the dielectric function becomes

$$\epsilon(w, k) = 1 - \frac{w_{pe}^2}{w^2} - \frac{3}{2} \frac{w_{pe}^2 k^2 v_{Te}^2}{w^4} + i\sqrt{\pi} \frac{2w_{pe}^2 w}{k^3 v_{Te}^3}, \quad (33)$$

and the dispersion relation reduces to

$$D(w, k_y) = \tanh(k_y \Delta) \\ + \frac{1}{1 - \frac{w_{pe}^2}{w^2}} \left\{ \coth\left(\frac{k_y L}{2}\right) - \frac{k_y}{\tau} \coth\left(\frac{\tau L}{2}\right) \right\}, \quad (34)$$

as given by Xu *et al.*⁶ where

$$\tau^2 = k_y^2 + \frac{2}{3} \frac{w^2}{w_{pe}^2 v_{Te}^2} (w_{pe}^2 - w^2). \quad (35)$$

From Eq. (34) with the assumption $\tau L \gg 1$, which is reasonable for $\Delta \ll L$, we arrive at

$$w_r^s = \frac{w_{pe}}{\sqrt{1 + \coth\left(\frac{k_y L}{2}\right) \coth(k_y \Delta)}} \\ \times \left(1 + \frac{\sqrt{3}}{2} k_y \lambda_{De} \sqrt{\tanh\left(\frac{k_y L}{2}\right) \coth(k_y \Delta)} \right) \quad (36)$$

for the symmetric (in the perpendicular, x direction) mode and

$$w_r^{AS} = \frac{w_{pe}}{\sqrt{1 + \tanh\left(\frac{k_y L}{2}\right) \coth(k_y \Delta)}} \\ \times \left(1 + \frac{\sqrt{3}}{2} k_y \lambda_{De} \sqrt{\coth\left(\frac{k_y L}{2}\right) \coth(k_y \Delta)} \right) \quad (37)$$

for the asymmetric (in x) branch. These results differ from those reported by Xu *et al.*⁶ in the second term in parentheses which, in the previous calculation, contained $\tanh(k_y \Delta)$ factors instead of $\coth(k_y \Delta)$. This is not insignificant because, for example, one can readily deduce that the temperature dependence of the asymmetric cutoffs ($k_y = 0$) is only captured by the correct expression. Theoretical and observed results will be included in the following section.

These relations represent symmetric and asymmetric surface/sheath modes analogous to $m=0$ (azimuthally symmetric) and $m=1$ (dipole) Gould-Trivelpiece modes in a dielectric lined cylindrical waveguide. The main difference, aside from the slab configuration, is that the dielectric lining has been replaced by a matrix sheath with thickness on the order of λ_{De} . In the limit $k_y \rightarrow 0$, we find that the symmetric (cutoff) frequency goes to zero and the asymmetric (cutoff) frequency approaches

$$\omega = \omega_{pe} \sqrt{\frac{2\Delta}{2\Delta + L}} \left(1 + \sqrt{\frac{3\lambda_{De}^2}{2\Delta L}} \right). \quad (38)$$

In the same limit, the frequency for the azimuthally symmetric Gould-Trivelpiece mode similarly tends to zero and the dipole Gould-Trivelpiece mode becomes

$$\omega = \frac{\omega_{pe}}{\sqrt{1 + K_e \frac{b^2 + a^2}{b^2 - a^2}}} \quad (39)$$

for $T_e = 0$ (plasma radius a , dielectric radius b , dielectric constant K_e). We note that, in the limit $a \rightarrow b$, Eq. (39) predicts that the dipole cutoff tends to zero. As shown here for the plasma slab, it is predicted that the presence of the plasma sheath will provide a nonzero cutoff for this mode. In the opposite limit $k_y \Delta, k_y L \gg 1$, the two slab modes merge and are represented by

$$\omega = \frac{\omega_{pe}}{\sqrt{2}} \left(1 + \frac{\sqrt{3}}{2} k_y \lambda_{De} \right). \quad (40)$$

Similarly, for Gould-Trivelpiece modes, the dipole and azimuthally symmetric modes both tend toward

$$\omega = \frac{\omega_{pe}}{\sqrt{1 + K_e}}. \quad (41)$$

In the semi-infinite slab limit, these modes resemble those studied in simulations by Decyk³ (who describes the same slab model with a fluid theory in the limit $\Delta \rightarrow \infty$) and those studied theoretically by Cheng and Harris.⁷ In the latter work, an expression for the Landau damping is given to be

$$\omega_i = -\omega_{pe} \sqrt{\frac{2}{\pi}} k_y \lambda_{De} \quad (42)$$

for $k_y L \gg 1$, but this expression is only valid for us in the more restrictive limit $k_y \Delta \gg 1$. Since we require $\Delta \sim \lambda_{De}$, we see that this violates the long wavelength approximation used by Cheng and Harris. Therefore we can not expect to see damping linear with k_y . [For the same reason we should be skeptical about the limit taken in Eq. (40).]

B. The limit $|k| \lambda_{De} \leq 1$

It is of more interest to examine the regime for which $k \lambda_{De} \leq 1$. This is because while we might have $k_y \rightarrow 0$, significant contributions to the sum in Eq. (32) may come from terms with $k_x \lambda_{De}$ approaching unity. This is because the eigenfunctions for the surface waves describing their dependence on the \hat{x} , perpendicular, direction necessarily include contributions from Fourier components given by $k_x \sim 2\pi/\Delta$ where we have chosen Δ to be a sheath thickness which is on the order of a few λ_{De} . When $\Delta \sim \lambda_{De}$, there are significant contributions to the plasma dielectric function [Eq. (28)] from components where $\zeta (= (\omega/\sqrt{2} k v_{Te})) \sim 1$, and one must evaluate Z , the plasma dispersion function, explicitly, in order to compute the dispersion relation. This has been done numerically; results with and without the approximation $k \lambda_{De} \ll 1$ will be shown. In the following section we shall refer to results based on the long wavelength approximation to Z as the "approximate" solutions and results based on the exact form of Z as the "exact" solution.

Of particular interest to later discussion is the value of ω for the asymmetric mode in the $k_y = 0$ limit. Assuming that the long wavelength limit is valid ("approximate" theory), Eq. (37) then reduces to [as previously demonstrated in Eq. (38)]

$$\omega_r^{AS} = \omega_{pe} \sqrt{\frac{2\Delta}{2\Delta + L}} \left(1 + \sqrt{\frac{3\lambda_{De}^2}{2\Delta L}} \right) \equiv \omega_{sr}, \quad (43)$$

where ω_{sr} is known as the series resonance⁸⁻¹⁰ which results from the balancing of the sheath capacitances and plasma inductance. It should be noted that ω_{sr} may be much lower than ω_{pe} when $L/\lambda_{De} \gg 1$.

C. Modes near ω_{pe}

Before leaving this model, we note that Eq. (32) also predicts a number of modes grouped around the electron plasma frequency. Using Eq. (34) and Eq. (35) for $\tau^2 < 0$ (requiring $\omega > \omega_{pe}$), we may derive an equation which determines τ as a function of k_y ,

$$-\cot\left(\frac{|\tau|L}{2}\right) \tan\left(\frac{|\tau|L}{2}\right) = \frac{|\tau|}{k_y} \left(\tanh(k_y \Delta) \frac{\sqrt{1 + 12(k_y^2 - \tau^2)} - 1}{\sqrt{1 + 12(k_y^2 - \tau^2)} + 1} + \frac{\coth\left(\frac{k_y L}{2}\right)}{\tanh\left(\frac{k_y L}{2}\right)} \right) \quad (44)$$

This rather complicated expression describing symmetric (upper) and asymmetric (lower) waves can be understood, after examination, by noting that the roots, k_x , for a given k_y , have spacing of about $2\pi/L$. These roots describe a discrete set of Bohm-Gross modes. The $k_y = 0$ cutoffs are cited in other work¹⁰ as thermal resonances.

These resonances have been observed experimentally in cylindrical plasmas¹¹ to have greater spacing than is predicted from a uniform density plasma model. Since our computer experiment is able to model accurately a uniform plasma, we do not discover this discrepancy. However, in the interest of more accurately understanding laboratory plasmas, in a later work we will consider the nonuniform plasma slab. Significantly better agreement between theory and laboratory observation of cylindrical resonance spectrum is demonstrated by incorporating the effects of a nonuniform density profile as suggested by Parker, Nickel, and Gould.¹²

IV. SIMULATION AND RESULTS

Particle-in-cell (PIC) simulations have been made to verify the calculations presented above. The first simulation strictly followed the matrix sheath model used in the calculation. Immobile ions were loaded with uniform density throughout the system, while mobile electrons were loaded uniformly in an interior region, leaving electron free slabs of thickness Δ next to each grounded boundary. In this electrostatic simulation, the electrons were specularly reflected at the sheath-plasma boundaries ($x = \Delta$ and $x = \Delta + L$) as in the calculation.

The particle-in-cell code XPDP2 was used for these simulations. This code has been adapted from XPDP1 (Ref. 13) to include a second spatial dimension which is taken to be periodic. Various routines have been added to enhance diagnostic output, including those needed for power spectrum densities. The grid spacings in \hat{x} and \hat{y} were chosen to resolve λ_{De} and the time step was chosen to resolve frequencies $\leq \omega_{pe}$. The number of physical particles per computer particle was kept small enough to ensure negligible self-heating over the simulation run-time. Finally, the length of the system in the propagating, \hat{y} , direction was long enough to ensure against finite grid effects⁵ affecting $\omega(k_y)$ over the range of k_y studied.

The simulation model has $L_x = L + 2\Delta = 2.0$ cm $= 37\lambda_{De}$, $L_y = 8.0$ cm, and $\Delta \approx 0.133$ cm. Zero-order plasma parameters in the central region are $n_e = n_i = 1.0 \times 10^{15} \text{ m}^{-3}$, $\omega_{pe} = 1.78 \times 10^9 \text{ s}^{-1}$, $T_e = 4.0 \text{ eV}$, $\lambda_{De} = 0.0468$ cm.

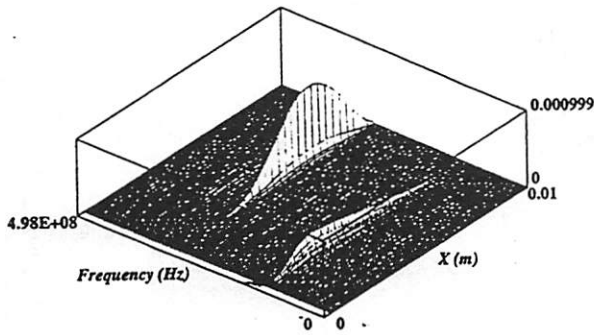


FIG. 2. PSD of electrostatic potential showing $|\Phi(x)|^2$ for the asymmetric sheath wave ($k_y=0$, series resonance). A metal wall is at $x=0$, and the midplane is at $x=0.01$ m.

A. Dispersion relations

The dispersion relations were measured by sampling the electrostatic potential in time and space. This signal was processed by windowing the data¹⁴ (in time and propagation dimension, \hat{y}) followed by taking discrete Fourier transforms in these dimensions. After time averaging the resultant transforms,¹⁴ one arrives at the power spectral density (PSD) in frequency and k_y of the electrostatic potential, $|\Phi(k_y, \omega, x)|^2$. This gives us detailed information on the structure of the signal in the perpendicular, \hat{x} direction, for a given frequency and k_y ; however, memory constraints limit the number of k_y 's for which this data may be kept. A sample of the measured $|\Phi(k_y, \omega, x)|^2$ data for $k_y=0$ is shown in Fig. 2. In order to obtain dispersion information, we need not record the mode structure in \hat{x} . Instead we calculate the power spectral density of

$$\Phi(k_y, \omega) = \sum_0^{L/2+\Delta} \Phi(x, y, t) \mp \Phi(L+2\Delta-x, y, t), \quad (45)$$

where the \mp sign is for (a)symmetric modes. The result is shown in Fig. 3 for the asymmetric branch.

The waves were thermally excited (i.e., small-amplitude) and a measure of the peak and full width at half maximum (FWHM) of the power spectral density $|\Phi(k_y, \omega)|^2$ was used to determine $\omega(k_y) = \omega_r(k_y) + i\omega_i(k_y)$. Figures 4 and 5 show simulation and theoretical results for real dispersion, $\omega_r(k_y)$, for the asymmetric and symmetric surface waves, and first three body (Bohm–Gross) waves. The “exact”

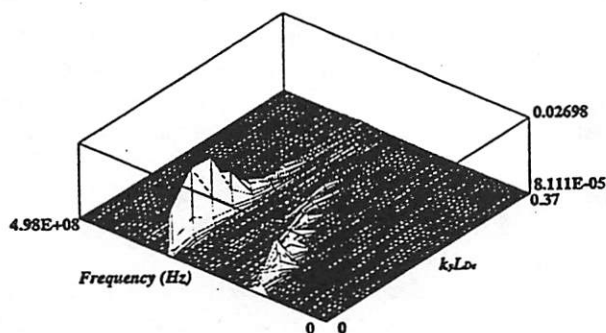


FIG. 3. PSD of electrostatic potential showing dispersion relation for asymmetric modes.

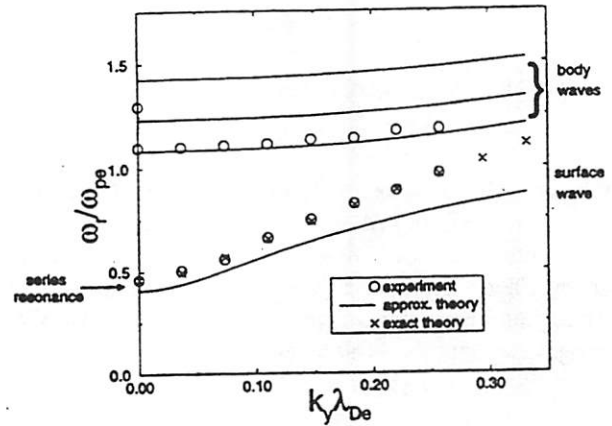


FIG. 4. Dispersion relations for matrix sheath simulation showing the asymmetric surface wave (lower) and asymmetric Bohm–Gross branches (upper).

theory shown in Fig. 4 refers to a numerical evaluation for ω_r which allows for $\zeta \sim 1$ as previously mentioned. We see that while there is a fair agreement between the measured data and the approximate theory, the exact theory is far more accurate in describing the sheath waves. In particular, we find that the series resonance (cutoff for the asymmetric sheath mode) predicted by the approximate theory differs from the measured value by 1.2 times the thermal correction predicted in Eq. (43). Put another way, if the approximate theory were used to predict the electron temperature, one would find $T_e = 19$ eV compared to the chosen value of 4 eV. One could alternatively adjust Δ to gain a better agreement. The predicted value for Δ using the approximate theory would be 0.184 cm compared to the chosen simulation value of 0.133 cm.

B. Eigenfunctions, $\phi(x)$

We next discuss the eigenfunctions $\Phi(x)$ associated with the sheath and body modes. These eigenfunctions describing the transverse dependence of the (a)symmetric sheath and body waves are plotted in Figs. 6–9 for different values of k_y . These plots were obtained from the $|\Phi(k_y, \omega, x)|^2$ PSDs (a sample output in Fig. 2) with background noise weakly dependent on frequency subtracted out.

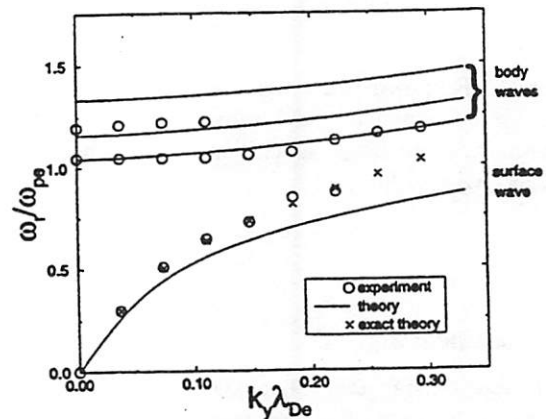


FIG. 5. Dispersion relations for matrix sheath simulation showing the symmetric surface wave (lower) and symmetric Bohm–Gross branches (upper).

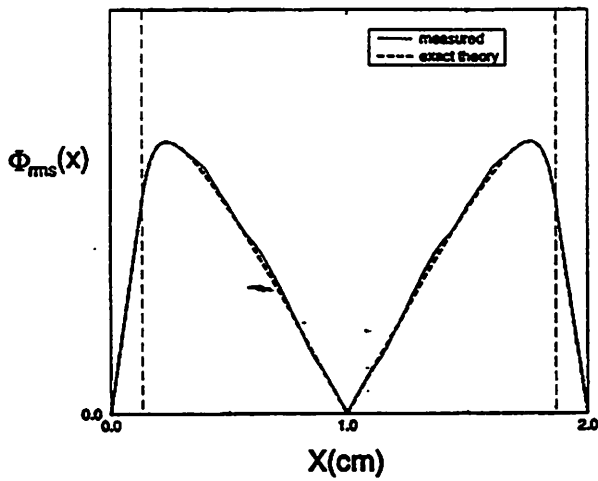


FIG. 6. Electrostatic potential perturbation, $\Phi_{ms}(x)$ (at series resonance, $k_y=0$). The position of the sheath plasma boundaries is also shown. Note, the cusp at $x=1.0$ cm in the measured data results from plotting a root-mean-square (rms) signal and the potential should be thought of as smoothly crossing zero at these points. The theoretical data have been plotted with the same cusps to facilitate comparison.

Numerical solutions of the exact theory are shown for comparison. Figure 6 shows the potential structure at the series resonance. The inferred electric field strength is nearly constant in the plasma body and a factor $(1 - \omega_{pe}^2/\omega^2)$ down from the strength in the sheaths. This is predicted by cold theory. The detailed matching of solutions at the plasma-sheath interfaces requires the exact warm kinetic solution. The $\Phi(x)$ for the first asymmetric (lowest frequency) body wave is shown in Fig. 7 for $k_y=0$. The associated fields are largest in the body of the plasma. Figures 8 and 9 show the symmetric eigenfunctions for the symmetric sheath mode and the first body symmetric mode at $k_y=2\pi/5L_y$.

To check that we are in fact measuring a thermal excitation, we can estimate the expected electrostatic field energy stored in a mode to be $\sim k_B T_e/2$ by appealing to the equipar-

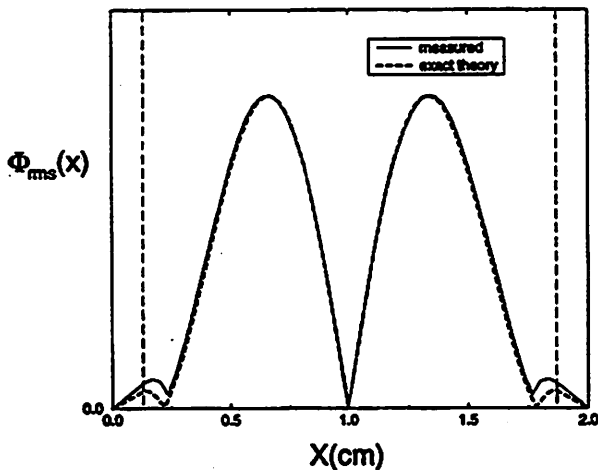


FIG. 7. Electrostatic potential perturbation, $\Phi_{ms}(x)$ [the first, asymmetric, Bohm-Gross (body) wave, $k_y=0$]. Note, the cusps in the measured data result from plotting a rms signal and the potential should be thought of as smoothly crossing zero at these points. The theoretical data have been plotted with the same cusps to facilitate comparison.

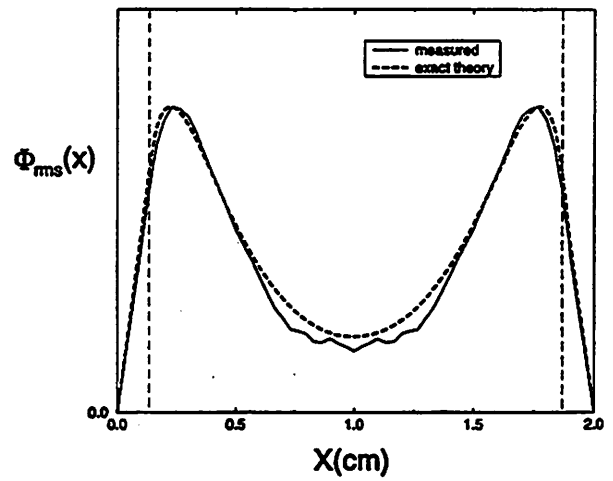


FIG. 8. Electrostatic potential perturbation, $\Phi_{ms}(x)$ [symmetric sheath wave, $k_y=5(2\pi)/8$ cm⁻¹].

titution theorem. It is a straightforward matter to calculate $\int dV E^2/\epsilon_0$, the electrostatic energy density associated with a particular eigenmode, from the data in Fig. 2. This has been done and the result is in reasonable agreement with the predicted value of $k_B T_e/2$ when one remembers that the real temperature as derived from the mean particle energy must be multiplied by the super-particle size.

C. Collisionless damping

Our linear Vlasov theory also contains results for the collisionless damping of the sheath and body waves found in our model. The expression for collisionless Landau damping of these waves is

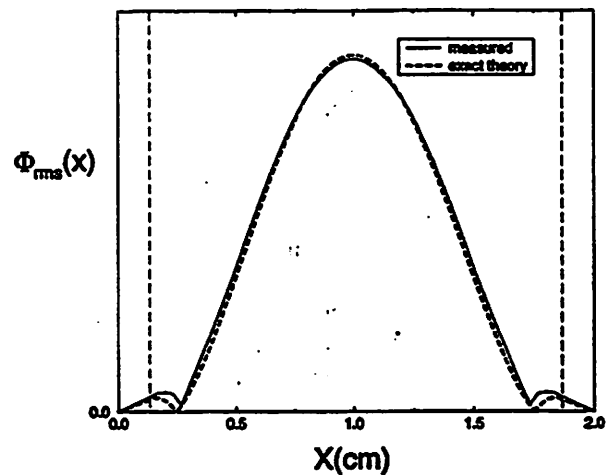


FIG. 9. Electrostatic potential perturbation, $\Phi_{ms}(x)$ [the first, symmetric, Bohm-Gross (body) wave, $k_y=5(2\pi)/8$ cm⁻¹]. Note, the cusps in the measured data result from plotting a rms signal and the potential should be thought of as smoothly crossing zero at these points. The theoretical data have been plotted with the same cusps to facilitate comparison.

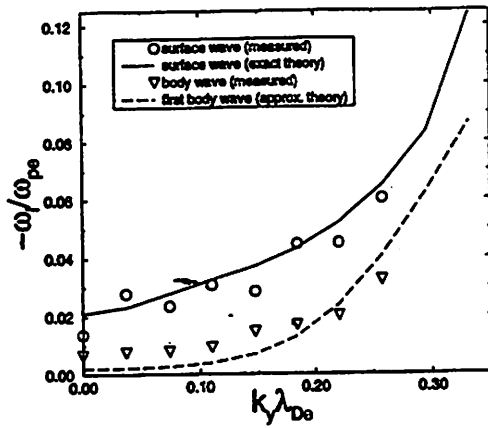


FIG. 10. Imaginary part of dispersion relations for the asymmetric surface wave and the first asymmetric Bohm-Gross branch.

$$\omega_i = \frac{-D_i(\omega_r, k_y)}{\left. \frac{\partial D_r(\omega, k_y)}{\partial \omega} \right|_{\omega_r}}$$

$$= \frac{\sum_{k_x}^{\infty} \frac{n\pi}{L} = -\infty \frac{\epsilon_i(\omega_r, k)}{k^2(\epsilon_r^2(\omega_r, k) + \epsilon_i^2(\omega_r, k))}}{\left. \frac{\partial}{\partial \omega} \left(\sum_{k_x}^{\infty} \frac{n\pi}{L} = -\infty \frac{\epsilon_r(\omega, k)}{k^2(\epsilon_r^2(\omega, k) + \epsilon_i^2(\omega, k))} \right) \right|_{\omega_r}} \quad (46)$$

This expression is evaluated numerically and compared with results from computer experiments in Fig. 10. No assumptions about ζ are used in evaluating the plasma dispersion function. The sheath wave damping is greater than the body wave damping because of the lower phase velocity (higher k_x) components which are present. Care has been taken to ensure that the number of computer particles per λ_{De}^2 is large enough to reduce the electron-electron Coulomb collision frequency well below the measured damping. (PIC simulation tends to minimize Coulomb collisions anyway, due to the finite spatial extent of the particles.) Error in the experimental measurements may be due to numerical fluctuations and finite sampling periods. Also, the data windowing technique tends to broaden resonance peaks.

D. Sheath without specular reflection

A further computer experiment was run in which the electrons and ions were initially given equal densities and loaded uniformly throughout the system. Still, the ions were immobile. After an initial transient in which electrons near the boundaries leave the system (i.e., sheaths are formed) the electron loss becomes negligible and surface/sheath waves are detected. This experiment more accurately represents the sheath dynamics of a laboratory plasma. Figure 11 shows the average density profiles for the specular reflection and self-consistent sheath experiments. Figures 12 and 13 show qualitative agreement between the self-consistent sheath experiment and the theoretical results based on specular reflection, but also indicate significant quantitative differences. We have chosen Δ for a best fit of Eqs. (36) and (37) to the

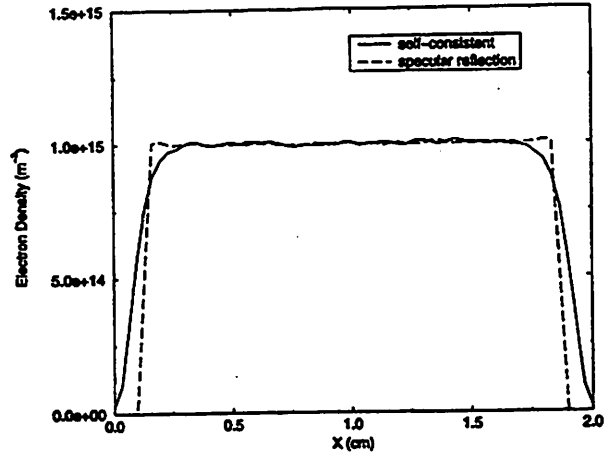


FIG. 11. Time averaged electron number density for self-consistent and matrix sheath computer experiments.

experimental data ($\Delta = 0.075$ cm). It should be noted that the reasonable fit achieved is somewhat fortuitous since we have pointed out the shortcomings of Eqs. (36) and (37). Not shown are results for the collisionless Landau damping in this simulation. The damping of both body and sheath waves was reduced from the respective values in the matrix sheath simulation. We suspect that the loss of the "tail" electrons whose \hat{x} directed energy exceeds the voltage drop across the sheath is the cause for the reduced damping. The absence of a distinct plasma/sheath boundary may also "smooth" out and decrease contributions to the $\Phi(x)$ eigenfunctions from higher (and more strongly damped) k_x components.

In a succeeding article, we will consider the effects of a nonuniform plasma density and show that a new set of waves can be observed.

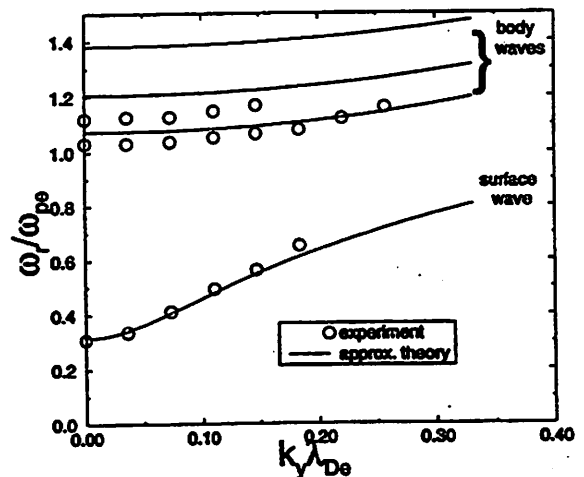


FIG. 12. Dispersion relations for self-consistent sheath simulation showing the asymmetric surface wave (lower) and asymmetric Bohm-Gross branches (upper). ω_{pe} is peak value.

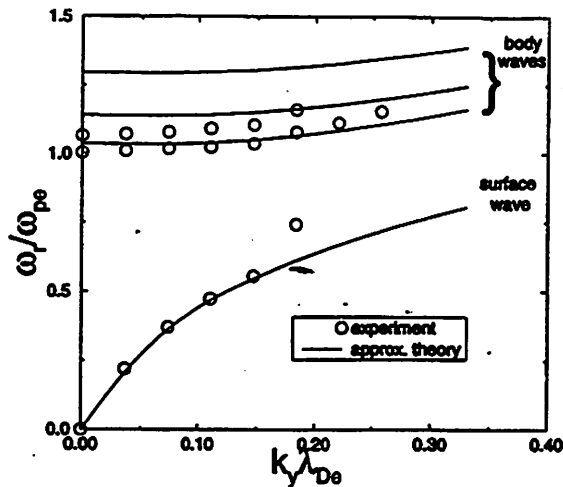


FIG. 13. Dispersion relations for self-consistent sheath simulation showing the symmetric surface wave (lower) and symmetric Bohm-Gross branches (upper). ω_{pe} is peak value.

V. CONCLUSIONS

We have shown theoretically and experimentally (by PIC simulation) that waves in a metal bound uniform plasma with matrix sheaths can propagate in the quasineutral body of the plasma as well as along the sheath plasma boundary. The electric field energy for the former is localized to the central region while the latter has stronger fields at the sheath-plasma boundary. We have shown that the dispersion relations for both real and imaginary ω describing these waves are well predicted by a linear Vlasov treatment and that significant contributions to the surface wave modes are made at $k\lambda_{De} \geq 1$. The eigenfunctions, $\Phi(x)$, for various points on the dispersion diagrams have been measured and are also in good agreement with theory. When the matrix sheath is replaced by a more self-consistent sheath model (ions still immobile), the dispersion relations can be fit to the theoretical results presented.

ACKNOWLEDGMENTS

The author thanks Professor C. K. Birdsall for suggesting the study which has formed the basis of this paper and also for his continued encouragement and guidance. The author would also like to thank X. Q. Xu for the helpful discussions of his related work. The technical assistance offered by V. Vahedi in adapting XDPD2 for this work is also greatly appreciated.

This work was supported in part by Office of Naval Research ONR-ASSERT N100014-93-1-1389.

- ¹A. W. Trivelpiece and R. W. Gould, *J. Appl. Phys.* **30**, 1784 (1959).
- ²A. W. Trivelpiece, *Slow-Wave Propagation in Plasma Wave Guides* (San Francisco Press, Inc., San Francisco, 1967).
- ³V. K. Decyk, Ph.D. thesis, University of California at Los Angeles, 1977.
- ⁴M. Moisan and Z. Zakrzewski, *J. Phys. D* **24**, 1025 (1991).
- ⁵C. K. Birdsall and A. B. Langdon, *Plasma Physics Via Computer Simulation* (Adam Hilger, Bristol, 1991).
- ⁶See AIP Document No. PAPS PHPAEN-5-038804-28 for 28 pages of X. Q. Xu, G. DiPeso, V. Vahedi, and C. K. Birdsall, Electronics Research Lab UCB/ERL M92/148 (1992). Order by PAPS number and journal reference from American Institute of Physics, Physics Auxiliary Publication Service, Carolyn Gehlbach, 500 Sunnyside Boulevard, Woodbury, New York 11797-2999. Fax: 516-576-2223, e-mail: paps@aip.org. The price is \$1.50 for each microfiche (98 pages) or \$5.00 for photocopies of up to 30 pages, and \$0.15 for each additional page over 30 pages. Airmail additional. Make checks payable to the American Institute of Physics.
- ⁷C. C. Cheng and E. G. Harris, *Phys. Fluids* **12**, 1262 (1968).
- ⁸R. W. Gould, *Phys. Lett.* **11**, 236 (1964).
- ⁹R. S. Harp and F. W. Crawford, *J. Appl. Phys.* **35**, 3436 (1964).
- ¹⁰P. E. Vandenplas, *Electron Waves and Resonances in Bounded Plasmas* (Interscience, New York, 1968).
- ¹¹A. Dattner, *Phys. Rev. Lett.* **10**, 205 (1963).
- ¹²J. V. Parker, J. C. Nickel, and R. W. Gould, *Phys. Fluids* **7**, 1489 (1964).
- ¹³J. P. Verboncoeur, M. V. Alves, V. Vahedi, and C. K. Birdsall, *J. Comput. Phys.* **104**, 321 (1993).
- ¹⁴W. H. Press, B. P. Flannery, S. A. Teukolsky, and W. T. Vetterling, *Numerical Recipes in C: The Art of Scientific Computing* (Cambridge University Press, New York, 1988).

Electron surface waves in a nonuniform plasma slab

D. J. Cooperberg

Department of Electrical Engineering and Computer Science, University of California, Berkeley, Berkeley, California 94720

(Received 11 August 1997; accepted 10 October 1997)

Electron surface waves in a nonuniform, metal bound, thermal plasma slab have been analyzed and detected. Measurements of the dispersion relations of these waves, as well as the eigenstructure of the perturbed electron density, reveal a spectrum of waves with frequencies above and below the peak electron plasma frequency in the slab. These waves are analogous to the Gould–Trivelpiece and Tonks–Dattner waves found in dielectric bound plasma columns. Measurements have been made using particle-in-cell simulation of an argon plasma and are compared with linear fluid theory in which the adiabatic approximation is made for the perturbed pressure. The presence of the metal boundary leads to regions near the plasma sheaths in which the fluid theory breaks down; we explore the differences between theory and measurement in this region. © 1998 American Institute of Physics. [S1070-664X(98)03904-4]

I. INTRODUCTION

The model of a uniform plasma with matrix sheaths, developed in a previously submitted article,¹ provided insight as to the behavior of “sheath sustained” surface waves. However, it failed to describe the full range of surface modes that we may expect to find in a self-consistent planar metal bound plasma. In a manner similar to that of Parker *et al.*^{2,3} in work on resonances in dielectric bound plasma columns, we now allow nonuniformity in the unperturbed electron and ion densities. This nonuniformity (in the direction perpendicular to the walls) allows for a new set of surface modes analogous to the secondary or Tonks–Dattner modes (associated with transverse resonances) observed in dielectric bound cylindrical dc discharges.^{4–7}

The resonance spectrum associated with plasma columns has been observed as early as 1931 by Tonks.^{8,9} A more detailed investigation of these resonances, which included data on the electron densities in the plasma column, was performed by Dattner.¹⁰ Both authors detected a main dipole resonance and higher resonances with frequencies found to lie between that of the main dipole resonance and the peak plasma frequency. These higher secondary resonances are known as Tonks–Dattner resonances. Vandenplas¹¹ outlines the evolution of the theoretical efforts employed to explain the observed resonance spectrum. A cold homogeneous fluid calculation predicted the main dipole resonance (at $\omega_{pe}/\sqrt{2}$); a warm homogeneous fluid model predicted additional resonances, but with different spacing and location than observed in experiment. Finally, good agreement was achieved by Parker *et al.*^{2,3} with a numerical calculation based on a warm inhomogeneous fluid model. Baldwin¹² examined the validity of this fluid approach and developed an alternate kinetic theory that was intended to represent better the Tonks–Dattner resonance spectrum of afterglow plasmas, where $r_w \gg \lambda_{De}$ (r_w is the plasma radius).

The main dipole resonance represents the $k_y=0$ cutoff for the dipole Gould–Trivelpiece surface wave¹³ and is

analogous to the series resonance in a metal bound plasma slab, which is the $k_y=0$ cutoff for the asymmetric sheath wave.¹ In addition to the main dipole resonance, experiments have shown that the Tonks–Dattner resonances are also *cut-offs* for electrostatic surface waves that propagate *along* the column axis.^{4–7}

It is the goal of this work to investigate the spectrum of electrostatic surface waves that can be found in the unmagnetized metal bound plasma slab. We will use the previous studies of the resonance spectrum and waves in dielectric bound plasma columns to assist in our work. Our use of metal boundaries, rather than dielectric boundaries used in previous work, emphasizes the importance of the sheath regions in determining the nature of the observed waves. The sheaths have often been omitted from previous theoretical treatments, where the dielectric boundary plays a more significant role in determining wave behavior. Additionally, in this work we will analyze the validity of the fluid approach and the assumption of a perturbed scalar pressure as made by Parker *et al.*³ It is hoped that this investigation may lead to a better understanding of sheath physics, and to applications such as bulk plasma control via surface wave excitation.

We will present a fluid theory here and compare the results with those of particle-in-cell (PIC) computer simulations.¹⁴ These simulations enabled the measurement of the wave dispersion relations and the structure of the surface waves (spatial variation) in the linear regime by the same means employed in our companion paper.¹ A description of the model is given in Sec. II. A linearized fluid theory is presented in Sec. III. In Sec. IV the PIC (particle-in-cell) simulation is discussed and, in Sec. IV, results from both theory and simulation are presented and analyzed. Conclusions are made in Sec. VI.

II. MODEL DESCRIPTION

The undriven, $2d3v$ (two spatial and three velocity components), thermal, plasma slab bound by conducting

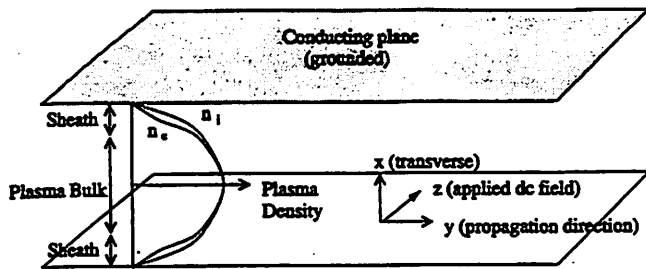


FIG. 1. Schematic of the plasma slab simulation.

grounded planes will be the subject of our theoretical analysis and PIC simulations (see Fig. 1). The \hat{x} direction is perpendicular to the walls and the \hat{y} is the propagation direction (parallel to the walls). The two species plasma consists of argon ions and electrons. Both species are mobile and warm. The steady-state plasma density is self-consistently determined from simulation by applying an electric field in the unresolved spatial dimension (\hat{z}) with a strength inversely proportional to the plasma density averaged in \hat{x} and \hat{y} . This model is equivalent to fixing a dc discharge current in \hat{z} since we also include a background of neutral argon atoms to model electron-neutral collisions. The use of a Monte Carlo collision algorithm,¹⁵ which models electron elastic and inelastic collisions, ion elastic collisions, and charge exchange, then allows a self-consistent dc discharge to form. This model allows for the formation of self-consistent electron density profiles (Fig. 2) and sheaths along the metal walls. The inelastic collision frequency is taken to be $\nu = \langle n_g \sigma(v) v \rangle = 1.2e7 \ll \omega_{pe}$, which is low enough to allow approximating this plasma as "collisionless" in our theoretical analysis. The presence of inelastic collisions causes some decrease in the electron energy probability function (EEPF) at higher energies (> 12 eV), as seen in Fig. 3, which displays the EEPF (from simulation) in each dimension. A more pronounced effect is the depletion of the electron population at the highest v_x , which results from the highest-energy (in \hat{x}) electrons escaping to the walls. How-

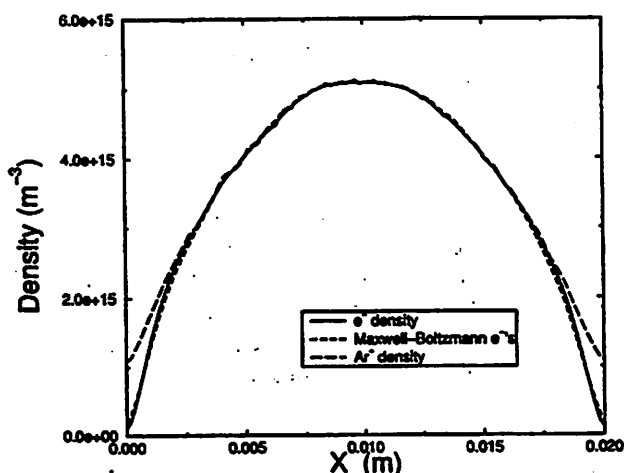


FIG. 2. Electron and ion density profiles averaged in the time and axial (\hat{y}) direction. Also shown is the electron density predicted by a Maxwell-Boltzmann distribution at $T_e = 6.02$ eV ($L_x = 2.0$ cm $\approx 78\lambda_{De}$).

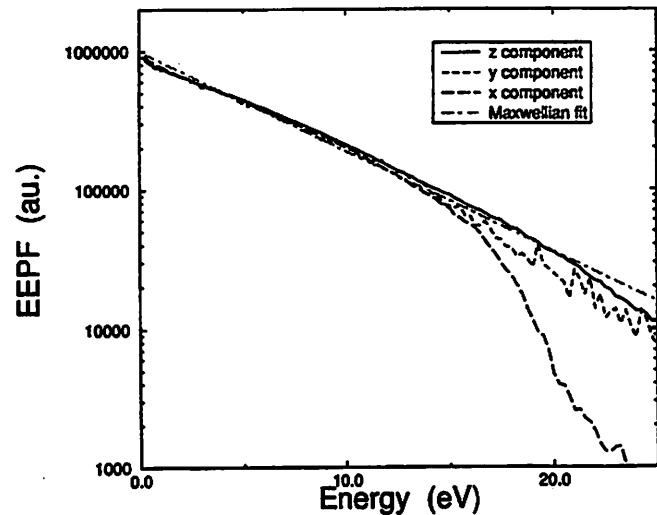


FIG. 3. Electron energy probability functions (EPPFs) in each velocity dimension. Also shown is the EEPF resulting from a Maxwellian distribution at $T_e = 6.02$ eV.

ever, since the plasma is nearly Maxwellian out to ~ 15 eV (the ionization energy), we shall consider the EEDF to be well represented by an isotropic Maxwellian at $T_{e0} = 6.02$ eV $= \langle m_e v^2 \rangle / 3$ (also shown in Fig. 3). Care is taken to subtract the drift velocity along the \hat{z} direction before computing the average kinetic energy. A plot of the electron density profile predicted by assuming a Boltzmann distribution at $T_{e0} = 6.02$ eV is shown to be in excellent agreement with the measured value (Fig. 2).

We have shown that the electrons in our computer experiment can be approximated as collisionless and Maxwellian, as desired. However, it would have been more desirable to maintain a lower electron temperature, since this would have further minimized the effect of depletion of the EEPF at high energies. The electron temperature in our dc discharge is self-consistently determined by (i) the neutral gas pressure, which unfortunately could not be further increased without loss of our collisionless assumption; and (ii) the discharge width (in \hat{x}), that could not be increased without the loss of computational efficiency. A compromise was reached in choosing these parameters.

III. LINEARIZED FLUID THEORY

The model described above forms a self-consistent sheath with a nonuniform density profile (Figs. 1 and 2). This system can be compared to the results of a linearized fluid calculation similar to that of Parker *et al.*,³ who described transverse resonances in an inhomogeneous thermal plasma column. We extend their analysis to include waves propagating along the wall in a plasma slab.

We will find main symmetric and antisymmetric modes that are analogous to azimuthally symmetric and dipole Gould-Trivelpiece¹³ waves in a dielectric bound plasma column, as well as secondary branches analogous to those studied by O'Brien *et al.*,^{4,5} Kerzar *et al.*,^{6,7} and others. The observed cutoff ($k_y = 0$) frequencies for these waves appear to result from standing longitudinal waves that are trapped in a

surface layer defined by a metal boundary on one side and some critical distance inside the plasma at which the local plasma frequency equals the wave frequency.³ Exponential decay of the mode is expected beyond this critical distance, toward the interior of the plasma. (These descriptions will be supported by the simulations in Sec. V.)

We proceed with the linearized fluid model as follows. First we write the electron density, fluid velocity and scalar pressure, and the electrostatic potential as the sums of steady-state and perturbation terms,

$$\begin{aligned} n_e &= n_{e0}f(x) + \bar{n}_1, & v_e &= v_{e0}(x) + \bar{v}_1, \\ p &= p_{e0}(x) + \bar{p}_1, & \Phi &= \Phi_0(x) + \bar{\Phi}_1, \end{aligned} \quad (1)$$

where the first-order terms are of the form $\bar{\Psi}_1 = \Psi_1(x)e^{i(k_y y - \omega t)}$. The function $f(x)$ represents the normalized steady-state electron density profile, which equals unity at the slab center and decreases monotonically toward the plasma boundaries. Here $f(x)$ is determined self-consistently by allowing the particles in our computer experiment (simulation) to reach an equilibrium. This approach is in contrast to the calculation by Parker *et al.*,³ who utilized an analytic approach for finding $f(x)$, using the model of Tonks and Langmuir.¹⁶ Since we are looking for solutions with $\omega \leq \omega_{pe0}$, we approximate the ions as an infinitely massive species. Therefore, we do not need to consider the ion dynamics in the analysis that follows. (The simulation used argon ions with $M_{Ar}/m_e = 73\,800$.) The steady-state ion density, $n_{i0}(x)$, is derivable from Poisson's equation using $\Phi_0(x)$ and $n_{e0}f(x)$.

Next we insert these linearized expressions into the electron continuity, electron momentum, and Poisson's equations, producing a set of zeroth- and first-order equations.

The resulting zeroth-order equations are

$$\nabla \cdot [n_{e0}f(x)v_{e0}(x)] = 0, \quad (2)$$

$$\begin{aligned} m_e n_{e0} f(x) [v_{e0}(x) \cdot \nabla] v_{e0}(x) \\ = -e n_{e0} f(x) \nabla \Phi_0(x) - \nabla p_{e0}(x), \end{aligned} \quad (3)$$

$$\nabla^2 \Phi_0(x) = -\frac{|e|}{\epsilon_0} [n_{i0}(x) - n_{e0}f(x)], \quad (4)$$

where m_e is the electron mass and e the signed electron charge. The quasistatic limit is justified since the slow-wave results we will obtain contain wavelengths much shorter than those in free space at the same frequency. Collision terms have been dropped with the assumption that $\nu_{col} \ll \omega$.

In order to obtain an equation for the potential, $\Phi_0(x)$, we proceed by assuming an isotropic, isothermal zeroth-order velocity distribution that allows us to write

$$\nabla p_{e0}(x) = k_B T_{e0} \nabla n_{e0} f(x). \quad (5)$$

Since there is a v_z drift in our model, we consider our analysis to take place in the rest frame of the plasma. Since there is no variation in \hat{z} , our final solution will have no \hat{z} dependence and we are free to apply the result in the lab frame. Inserting Eq. (5) into Eq. (3) produces

$$\begin{aligned} m_e n_{e0} f(x) [v_{e0}(x) \cdot \nabla] v_{e0}(x) \\ = -e n_{e0} f(x) \nabla \Phi_0(x) - k_B T_{e0} \nabla n_{e0} f(x). \end{aligned} \quad (6)$$

Dividing through by m_e , n_{e0} , and $f(x)$ leaves

$$[v_{e0}(x) \cdot \nabla] v_{e0}(x) = -\frac{e}{m_e} \nabla \Phi_0(x) - \frac{v_{Te0}^2}{2} \frac{\nabla f(x)}{f(x)}, \quad (7)$$

where we have used $v_{Te0}^2 = 2k_B T_{e0}/m_e$. For the one-dimensional variation of zeroth-order quantities considered here, $v_{e0} = v_{e0} \hat{x}$, and Eq. (7) becomes

$$\frac{1}{2} v_{e0}^2(x) = -\frac{e}{m_e} [\Phi_0(x) - \Phi_0(x_{mid})] - \frac{v_{Te0}^2}{2} \ln[f(x)] \quad (8)$$

(where x_{mid} marks the midplane of the slab). In the limit $v_{e0}^2(x) \ll v_{Te0}^2 \ln[f(x)]$, which is easily achieved for the profiles and temperatures of interest, we may set the term on the left-hand side to zero. We may then simplify Eq. (6), leading to

$$\nabla \Phi_0(x) = -\frac{k_B T_{e0}}{e} \frac{\nabla f(x)}{f(x)}, \quad (9)$$

which is the governing equation for $\Phi_0(x)$, with $f(x)$ obtained from simulation.

The first-order equations are

$$\begin{aligned} -i\omega \bar{n}_1 + n_{e0} f(x) \nabla \cdot \bar{v}_1 + \bar{n}_1 \nabla \cdot v_{e0}(x) + v_{e0}(x) \cdot \nabla \bar{n}_1 \\ + \bar{v}_1 \cdot \nabla n_{e0} f(x) = 0, \end{aligned} \quad (10)$$

$$\begin{aligned} -i\omega m_e n_{e0} f(x) \bar{v}_1 + m_e n_{e0} f(x) \{(\bar{v}_1 \cdot \nabla) v_{e0}(x) \\ + [v_{e0}(x) \cdot \nabla] \bar{v}_1\} + m_e n_1 [v_{e0}(x) \cdot \nabla] v_{e0}(x) \\ = -e n_{e0} f(x) \nabla \bar{\Phi}_1 - e \bar{n}_1 \nabla \Phi_0(x) - \nabla \bar{p}_1, \end{aligned} \quad (11)$$

$$\nabla^2 \bar{\Phi}_1 = \frac{|e|}{\epsilon_0} \bar{n}_1. \quad (12)$$

Second-order terms have been dropped.

We now proceed to obtain an equation in $\bar{\Phi}_1(x)$. We begin by eliminating the terms including v_{e0} . We can do so with the same assumption $v_{e0}^2(x) \ll v_{Te0}^2 \ln[f(x)]$ used previously, along with the assumptions $\partial_x v_{e0}(x)/\omega \ll 1$ (which roughly states that the electrons may not drift a substantial fraction of the length of the system in a wave period) and $v_{e0}(x) \partial_x \bar{v}_1 / (\bar{v}_1 \omega)$, $v_{e0}(x) \partial_x \bar{n}_1 / (\bar{n}_1 \omega) \ll 1$ (which roughly states that the drift velocity must be much less than the phase velocity of the wave in the perpendicular, \hat{x} direction). Actually, v_{e0} may be estimated from the ion flux (in \hat{x}) through the system that is not zero (as in the infinite mass limit), but varies from zero at the midplane to some value on the order of $n_{i0} u_B = n_{i0} \sqrt{k_B T_{e0}/m_i}$ at the sheath edge. The ion flux must be equal to the steady-state electron flux, $n_{e0} f(x) v_{e0}(x)$, in order to preserve charge. This equality can be used to estimate $v_{e0}(x)$ from which the soundness of the limits taken above is supported.

We also need to choose some approximation (a closure scheme) in order to evaluate the last term on the right-hand side of Eq. (11). We chose, as is regularly done for an un-

magnetized collisionless plasma, the adiabatic approximation where the heat flux vector is set to zero. In this case it has been shown⁵ that [for $p_{e0} = n_{e0}f(x)k_B T_{e0}$, $v_{e0} = 0$]

$$(\nabla \bar{p}_1)_j = 3k_B T_{e0} \frac{\partial \bar{n}_1}{\partial x_j} + \frac{k_B T_{e0}}{i\omega} \sum_{k=i,j,k} \frac{\partial}{\partial x_k} \times \left(-n_{e0}f(x) \frac{\partial \bar{v}_{1j}}{\partial x_k} + 2\bar{v}_{1k} \frac{\partial n_{e0}f(x)}{\partial x_j} + n_{e0}f(x) \frac{\partial \bar{v}_{1k}}{\partial x_j} \right). \quad (13)$$

This expression can be simplified somewhat, given our 2d3v model in which \bar{v}_1 lies in the x - y plane and that the zeroth-order electron density is only a function of x . The resulting expression is

$$(\nabla \bar{p}_1) = 3k_B T_{e0} \nabla \bar{n}_1 + \frac{k_B T_{e0}}{i\omega} \left\{ \left[2 \frac{\partial n_{e0}f(x)}{\partial x} \nabla \cdot \bar{v}_1 + 2\bar{v}_{1x} \frac{\partial^2 n_{e0}f(x)}{\partial x^2} + n_{e0}f(x) \frac{\partial}{\partial y} \times \left(-\frac{\partial \bar{v}_{1x}}{\partial y} + \frac{\partial \bar{v}_{1y}}{\partial x} \right) \right] \hat{x} + \frac{\partial}{\partial x} \times \left(-n_{e0}f(x) \frac{\partial \bar{v}_{1y}}{\partial x} + n_{e0}f(x) \frac{\partial \bar{v}_{1x}}{\partial y} \right) \right\}. \quad (14)$$

This equation is still prohibitively complex. If we define $L(x)^{-1} \equiv \partial \ln[n_{e0}f(x)]/\partial x$ and assume $L(x)$ to be of the order of the slab thickness, except in the plasma sheath region, we may greatly simplify Eq. (14) with the further assumptions that (i) $\bar{v}_{1y} \ll \bar{v}_{1x}$, which is roughly equivalent to requiring that axial variations (in \hat{y}) occur over a longer wavelength than in the perpendicular (\hat{x}) direction (nearly one dimensional); and that (ii)

$$L(x) \frac{\nabla \cdot \bar{v}_1}{|\bar{v}_1|} \gg 1 \quad (15)$$

(the variation of the waves in \hat{x} must be on a scale much smaller than the slab thickness). In this limit we simply have

$$(\nabla \bar{p}_1) = 3k_B T_{e0} \nabla \bar{n}_1. \quad (16)$$

In the sheath region, the scale length, $L(x)$, of the steady-state density profile is no longer on the order of the slab thickness, but on the order of the electron Debye length, and Eq. (15) may not hold if the perturbation wavelength in the sheath region is too large. We examine the validity of Eq. (15) when analyzing our results (Sec. V).

Finally, after dropping terms with $v_{e0}(x)$ and making the adiabatic assumption for \bar{p}_1 , we use Eqs. (10), (12), and (9) in the divergence of Eq. (11) to produce an equation in $\bar{\Phi}_1$,

$$\nabla^2 \nabla^2 \bar{\Phi}_1 - \frac{1}{\gamma} \left(\frac{\nabla f(x)}{f(x)} \cdot \nabla \right) \nabla^2 \bar{\Phi}_1 + \left[\frac{1}{\gamma \lambda_{De}^2} \left(\frac{\omega^2}{\omega_{pe0}} - f(x) \right) - \frac{1}{\gamma} \nabla \cdot \left(\frac{\nabla f(x)}{f(x)} \right) \right] \nabla^2 \bar{\Phi}_1 - \frac{1}{\gamma \lambda_{De}^2} \nabla f(x) \cdot \nabla \bar{\Phi}_1 = 0. \quad (17)$$

After using our assumption, $\bar{\Phi}_1 = \Phi_1(x)e^{i(k_y y - \omega t)}$, we then obtain

$$\frac{\partial^4 \Phi_1(x)}{\partial x^4} - 2k_y^2 \frac{\partial^2 \Phi_1(x)}{\partial x^2} + k_y^4 \Phi_1(x) - \frac{1}{\gamma} \left(\frac{\partial_x f(x)}{f(x)} \right) \times \left(\frac{\partial^3 \Phi_1(x)}{\partial x^3} - k_y^2 \frac{\partial \Phi_1(x)}{\partial x} \right) + \left[\frac{1}{\gamma \lambda_{De}^2} \left(\frac{\omega^2}{\omega_{pe0}} - f(x) \right) - \frac{1}{\gamma} \frac{\partial}{\partial x} \left(\frac{\partial_x f(x)}{f(x)} \right) \right] \left(\frac{\partial^2 \Phi_1(x)}{\partial x^2} - k_y^2 \Phi_1(x) \right) - \frac{1}{\gamma \lambda_{De}^2} \frac{\partial f(x)}{\partial x} \frac{\partial \Phi_1(x)}{\partial x} = 0. \quad (18)$$

This fourth-order differential equation [Eq. (18)] is solved numerically in order to produce the dispersion relations and the eigenfunctions $\Phi_1(x)$ for the range of electrostatic waves existing in the frequency range ω_{pi} , $\nu_c \ll \omega \leq \omega_{pe0}$. In Eq. (18), ω_{pe0} and λ_{De} [Eq. (18)] are defined as their values at the midplane.

In order to obtain numerical solutions, we need appropriate boundary conditions. We assume that solutions have either even or odd symmetry about the midplane. First, we require that the perturbed electron current density in the \hat{x} direction,

$$i\omega m_e \hat{J}_{1x}(x) \equiv -i\omega m_e |e| n_{e0} f(x) v_{1x}(x) = e^2 n_{e0} f(x) \frac{\partial \Phi_1(x)}{\partial x} + k_B T_{e0} \epsilon_0 \times \left(\frac{\partial^2 \Phi_1(x)}{\partial x^2} - k_y^2 \Phi_1(x) \right) \frac{\partial_x f(x)}{f(x)} - 3k_B T_{e0} \epsilon_0 \left(\frac{\partial^3 \Phi_1(x)}{\partial x^3} - k_y^2 \frac{\partial \Phi_1(x)}{\partial x} \right), \quad (19)$$

vanishes at the boundaries.³ This requirement is equivalent to assuming specular reflection of the perturbed electron current density at the plasma boundary (metal wall). Second, we require that the potential must be zero at the grounded walls. We are now able to solve Eq. (18) for $\Phi_1(x)$ to within an arbitrary constant.

We consider the solution of either the even or odd mode to be the linear combination of two modes giving $\Phi_1(x) = 0$ at the wall. The two modes chosen for the even (odd) solution have either the zeroth (first) or second (third) derivative of $\Phi_1(x_{\text{midplane}})$ set to a constant with all other derivatives set to zero, in order that the numerical solution of Eq. (18) may proceed from x_{midplane} toward the wall. These conditions are met only at discrete values of ω/ω_{pe0} , which are located by finding the zeros of the perturbation current density [Eq. (19)] at the wall (as derived from the numerical solutions described above) versus ω/ω_{pe0} .

We end our theoretical analysis with a further discussion of the limits of its applicability. In addition to the restrictions associated with neglecting electron drift and reducing the perturbed pressure [Eq. (13)] to a manageable form, we also must examine the limits of the adiabatic approximation and

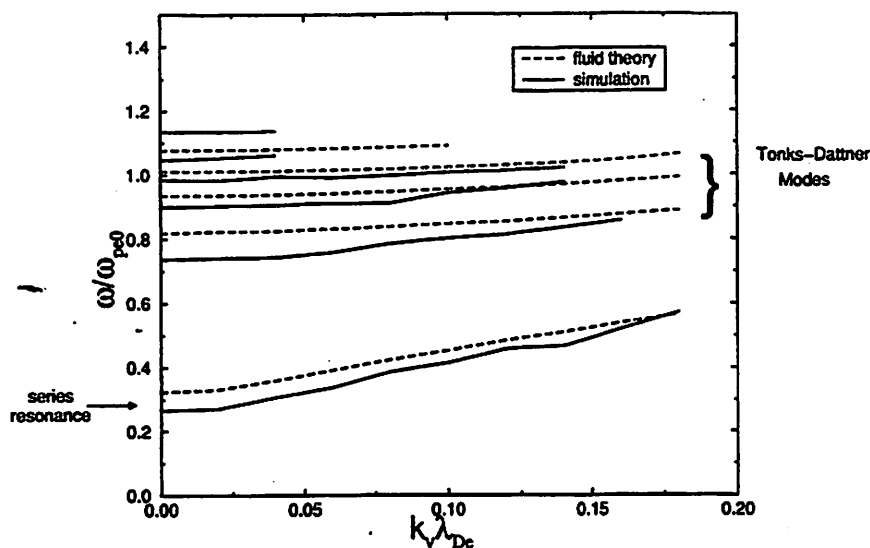


FIG. 4. Dispersion relations for asymmetric modes, giving wave frequency as a function of the wave number in the propagating dimension (\hat{y}). A main (lowest frequency) and secondary branches with $\omega < \omega_{pe}$ are shown. Body modes with $\omega > \omega_{pe}$ are also shown. Here ω_{pe} is defined as the peak value. The cutoff ($k_y = 0$) for the main surface wave is known as the series resonance.

the restrictions imposed by linearity. It has been pointed out by Baldwin¹² (for afterglow plasma columns, where the electron Debye length is especially short), that the fluid representation breaks down, since $k_r \lambda_{De}$ (k_r being the local wave vector perpendicular to the column axis and to the walls) can approach and exceed unity. Beyond this point, the waves are heavily Landau damped and the adiabatic approximation breaks down. In our slab model there is also a region (typically within the sheath) where, due to a decreasing $n_{e0} f(x)$, $k_x \lambda_{De}$ can approach unity and the adiabatic fluid model will be violated. However, since in this study we focus on the steady-state discharge with $T_{e0} \sim 6$ eV, the length over which $k_x \lambda_{De} \sim 1$ is small, as will be discussed further in Sec. V, and we are able to use the fluid theory.

Our assumption of linearity further imposes the restraint that $(\nabla \cdot \mathbf{v}_1 + v_{1x}/L)/\omega \ll 1$, as can be derived from the linearized continuity equation. This roughly indicates that the perturbation velocity is much smaller than the local phase velocity and the bounce velocity $L\omega$. The linearized momentum equation further requires that $v_1 \ll v_{Te}^2 / [\omega \nabla \ln(n_1)]$.

The dispersion (ω vs k_y) and eigenfunctions (in \hat{x}) will be shown in the next section, compared with results from simulation (which has far fewer assumptions and approximations).

IV. SIMULATION DESCRIPTION

The particle-in-cell code XPDP2¹⁷ was used for the simulation of the $2d3v$ plasma slab described in Sec. II. The simulation time step, Δt , is chosen to resolve frequencies up to the peak electron plasma frequency. The grid spacing in \hat{x} is chosen to resolve the electron Debye length so that the sheaths and Landau damping are well resolved. The slab thickness (in \hat{x}) is chosen to be 2 cm and the periodic length (in \hat{y}) is 8 cm. A standard leap-frog particle advance is used along with a bilinear particle and field weighting scheme and a Poisson solver that reduces to a tridiagonal matrix solver.¹⁴

The physical parameters describing the plasma slab simulation include peak electron density $n_{e0} = 5.1 \times 10^{15} \text{ m}^{-3}$, electron temperature $T_e = (2/3) \langle mv^2/2 \rangle = 6.02$ eV, Debye length at the midplane $\lambda_{De} = 0.0255$ cm, slab thickness (equal to wall spacing) $L_x = 2.0$ cm $= 78 \lambda_{De}$, plasma midpotential $V_{\text{mid}} = 39.5$ V, and peak electron plasma frequency $\omega_{pe0} = (2\pi) 6.41 \times 10^8$ rad/s.

Figures 4 and 5 show the theoretical and experimental results for the dispersion relation $\omega(k_y)$ of symmetric and asymmetric modes, whose frequencies lie below and above ω_{pe} . The experimental measurements are obtained from peaks in the power spectral density, $|\Phi(k_y, \omega)|^2$, in the same

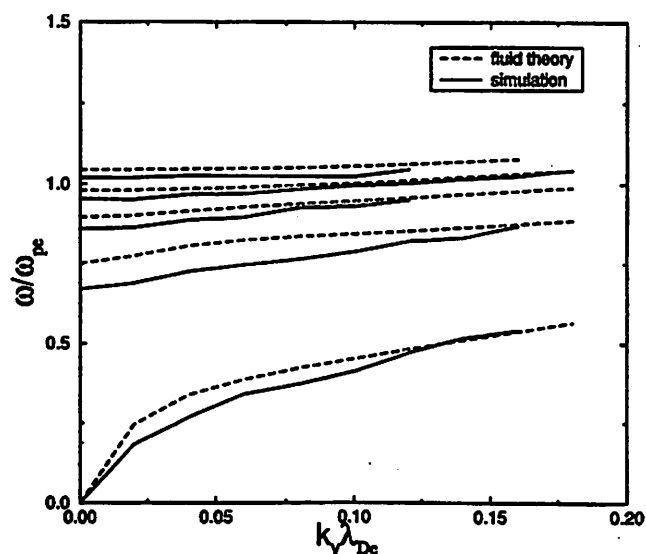


FIG. 5. Dispersion relations for symmetric modes giving the wave frequency as a function of the wave number in the propagating dimension (\hat{y}). A main (lowest frequency) and secondary branches with $\omega < \omega_{pe}$ are shown. Body modes with $\omega > \omega_{pe}$ are also shown. Here ω_{pe} is defined as the peak value.

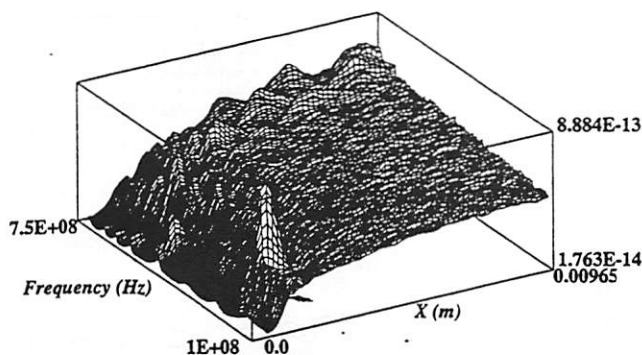


FIG. 6. The sample output for the power spectral density (PSD) of the asymmetric charge density perturbation $|\rho(x, f, k_y = 0)|^2$. The normal modes are clearly differentiated from the noise (metal wall at $x = 0$ m; midplane at $x = 0.01$ m).

fashion as described in a previously submitted article.¹ These peaks are generated by thermal (particle) fluctuations; the full width at half-maximum is measured and taken to be approximately equal to the electron-neutral collision frequency. Higher “body” modes are only weakly detected because the summing technique employed in deriving $|\Phi(k_y, \omega)|^2$ poorly detects potential signals with zero crossings (other than at the midplane). A more sophisticated scheme could have been employed; however, these higher modes are well known and are not the focus of our study.

In addition to the dispersion relations, we have measured the eigenmode structure, $n_1(x)$, of these waves. The results are derived from $|\rho(k_y, \omega, x)|^2$, the power spectral density (PSD) of the charge density. A sample output of $|\rho(k_y, \omega, x)|^2$ is given for the odd modes at $k_y = 0$ in Fig. 6. The waves are easily identified by the enhanced signal at discrete frequencies that coincide with those found from $|\Phi(k_y, \omega)|^2$, and arise from thermal fluctuations. The electron density perturbation at the frequency corresponding to a particular wave mode, at a given k_y , is derived from these PSD measurements by subtracting a background noise signal (proportional to the steady-state electron density profile) from the $|\rho(k_y, \omega, x)|^2$ signal. The constant of proportionality has a frequency dependence that might be determined explicitly, but in our results we have chosen the value necessary to ensure that the perturbation amplitude goes to zero at the midplane. This fitting is reasonable for all but the highest symmetric mode, which may have a significant perturbation at the midplane. For these modes the proportionality constant may be alternatively determined by fitting the detected signal minima as closely as possible to zero amplitude. In the above discussion, we have made the assumption that, for the frequencies of interest $\sim \omega_{pe}$, the contribution to the PSD of the charge density from ions is negligible so that the charge density PSD represents the electron density PSD (multiplied by the electron charge).

Additional measurement of $|v_{1x}(k_y, \omega, x)|^2$ has been made; the data provides verification of the theoretical boundary condition requiring that the perturbed flux to the walls equal zero.

The signal detection scheme described here is realizable because PIC simulation allows the fine spatial detail in elec-

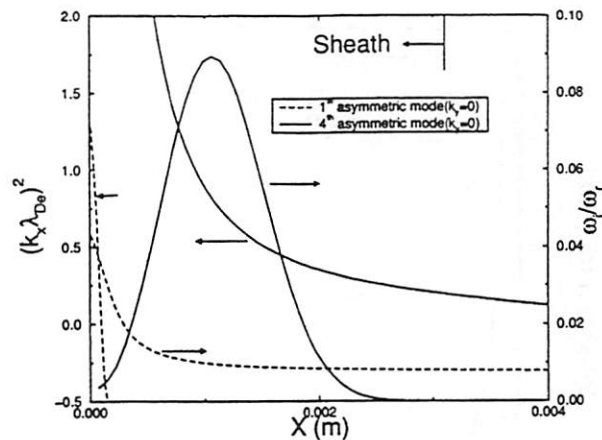


FIG. 7. The local wave number and local Landau damping for the main asymmetric mode and the last detected asymmetric Tonks–Dattner mode (long-wavelength limit, $k_y = 0$, metal boundary at $x = 0$ m). Negative $(k_x \lambda_{De})^2$ corresponds to exponential decay into the plasma, at $x > x_c$.

tron density and electrostatic potential to be measured accurately and nonintrusively. This provides distinct advantages over laboratory experiments that require launching and detecting antennae that require exciting waves to higher energies and can allow for coupling to extraneous signals. For example, in the work of O’Brien⁵ on slow wave measurements in a plasma column, waves were launched and detected with a variety of azimuthally symmetric and dipole antennae. Phase coherent detectors were used to measure the axial wave number. However, coupling to unwanted symmetries and closely spaced neighboring Tonks–Dattner modes severely limited the range of detectable wave phenomenon. As a final consideration, the metal bound plasma slab studied in this work cannot easily be studied in the laboratory in the same fashion as the dielectric bound plasma cylinder since the coupling from outside the plasma volume is not possible.

V. RESULTS

The theoretical and measured values for the dispersion relations $\omega(k_y)$ of asymmetric and symmetric electrostatic waves shown in Figs. 4 and 5 represent surface waves with $\omega < \omega_{pe0}$ and body waves with $\omega > \omega_{pe0}$. While the spacing and approximate location are well captured by the linearized fluid theory described in Sec. III, the theoretical results are at consistently higher frequencies than those of the observed waves. We consider two possible reasons for the discrepancy.

The first is that the adiabatic assumption for the perturbation, which requires $\omega/k_x \gg v_{Te}$, breaks down near the boundaries. Figure 7 shows the local wave number ($k_y = 0$) in \hat{x} for the first and fourth asymmetric modes. The adiabatic assumption fails in the region where $k_x \lambda_{De} \ll 1$ no longer holds. In this region we can also expect significant Landau damping; the local collisionless damping frequency, ω_i , is also plotted in Fig. 7. The local wave number in \hat{x} and damping rate are approximated by the long-wavelength limits,

$$k_x \lambda_{De}(x) = \sqrt{\left(\frac{\omega^2}{\omega_{pe}(x)^2} - 1\right)} / 3 \quad (20)$$

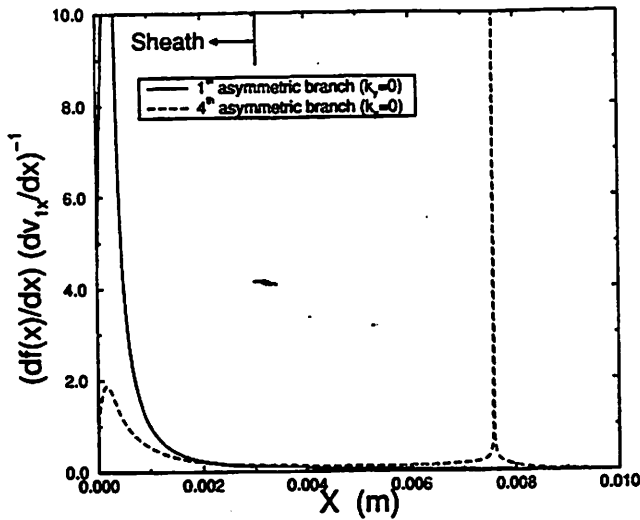


FIG. 8. The region and degree of validity for Eq. (15) is illustrated for the main asymmetric mode and the last detected asymmetric Tonks–Dattner mode ($k_y=0$). The solutions to Eq. (18) have been used to calculate the ordinate.

and

$$\frac{\omega_i}{[\omega]_r}(x) = \sqrt{\frac{\pi}{8}} \frac{1}{[k_x \lambda_{De}(x)]^3} \times e^{(-3/2)} e^{\{(1+3[k_x \lambda_{De}(x)]^2)/2[k_x \lambda_{De}(x)]\}}, \quad (21)$$

where Eq. (20) reduces to the dispersion relation for Langmuir waves, $\omega_{pe}(x)^2 = n_{e0} f(x) e^2 / (\epsilon_0 m_e)$ and $\lambda_{De}(x)^2 = \epsilon_0 k_B T_{e0} / [n_{e0} f(x) e^2]$. Figure 7 shows that the adiabatic approximation is more severely violated for the higher resonances, yet our dispersion data shows a greater error in the theory for the lowest modes.

The second reason offered for the error in the theory is that the inequality given by Eq. (15) is not sufficiently satisfied. The region of strongest variation in $f(x)$ occurs in the plasma sheath. Figure 8 shows a plot of $\{\partial_x \ln[f(x)]\} / [\partial_x \ln(v_{1x})]$ for the first and fourth asymmetric resonances. The lower-frequency mode is shown to be more poorly represented by Eq. (15). Thus, we consider the simplifications in the fluid derivation made by neglecting terms resulting from the plasma inhomogeneity as the more likely source of error in the theoretical dispersion relations.

The first symmetric and asymmetric branches (occurring at lowest frequencies in Figs. 4 and 5), which are present even in the cold, uniform plasma model, provided that a dielectric region exists between the plasma and metal boundary, are known as the main surface wave branches and are analogous to the $m=0$ and $m=1$ (m equals the azimuthal mode number) Gould–Trivelpiece surface modes in the plasma cylinder and also to the “sheath” modes in the uniform plasma slab described in a previously submitted paper,¹ while the higher modes with $k_y=0$ cutoffs below ω_{pe}^{4-27} are analogous to the propagating Tonks–Dattner modes.

Next we discuss the results for the perturbed electron density, $n_1(x)$. Figures 9–16 show the theoretical and measured values for the symmetric and asymmetric modes identified in Figs. 4 and 5 for $k_y \lambda_{De} = 0$ and $k_y \lambda_{De} = 0.08$. Theo-

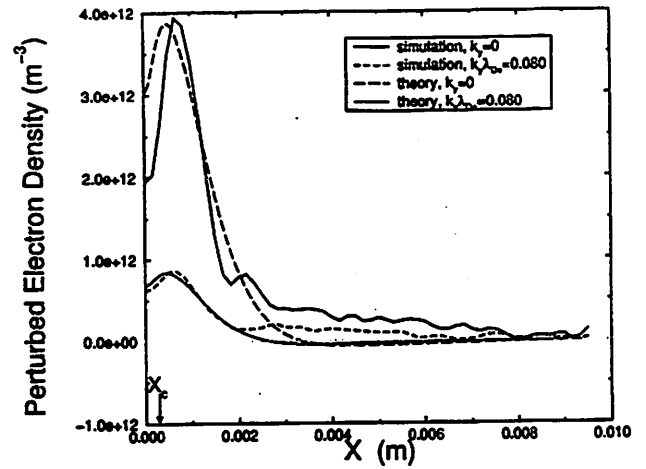


FIG. 9. The amplitude of the electron density perturbation of the first (main) asymmetric surface mode from a metal boundary ($x=0$ m) to the midplane ($x=0.01$ m) of the system. Theory and experiment at two different values of k_y are shown.

retical curves are computed at the frequencies of the observed resonances rather than at the theoretical frequencies. Although the resolution of the experiment is not as high as the theoretical data (due to computational limits), the agreement is satisfactory. We observe that the measured eigenfunctions tend to oscillate more rapidly toward the edge than the theoretical curves and this phase difference at the wall is most pronounced for the first and second symmetric and asymmetric branches. This observation is consistent with the differences between the theoretical and measured dispersion relations, which showed the largest disagreement at these same two lowest modes, and may be attributed mainly to an unjustified simplification of terms relating to the plasma inhomogeneity.

The qualitative picture presented by Parker *et al.*,³ in which Tonks–Dattner resonances are considered to represent Langmuir waves trapped between an overdense region and the plasma boundary, is clearly illustrated by the $n_1(x)$ data. The critical point, x_c , shown in Figs. 9–16 for the $k_y=0$

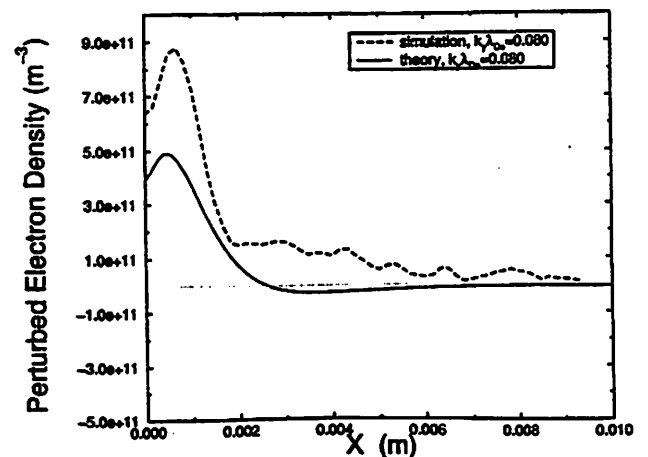


FIG. 10. The amplitude of the electron density perturbation of the first (main) symmetric surface mode from the metal boundary ($x=0$ m) to the midplane ($x=0.01$ m) of the system. This mode has no $k_y=0$ cutoff.

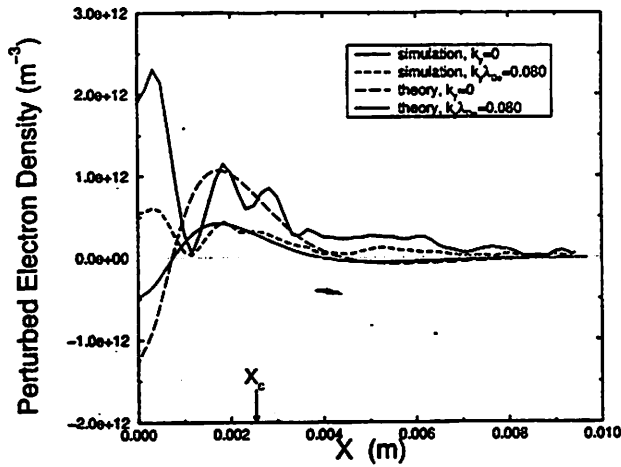


FIG. 11. The amplitude of the electron density perturbation of the second asymmetric surface (Tonks–Dattner) mode from a metal boundary ($x = 0$ m) to the midplane ($x = 0.01$ m) of the system. Theory and experiment ($|n_1|$ shown from simulation; n_1 shown from theory) at two different values of k_y , are shown.

modes, marks the location at which the oscillation frequency equals the local plasma frequency. We expect a decaying solution for $\Phi_1(x)$ from this point toward the center. From x_c toward the plasma edge, a Langmuir wave may propagate in \hat{x} with the wavelength decreasing as the electron density decreases. It is in this region that Baldwin¹² correctly questioned the validity of the fluid calculation and develops a kinetic theory that allows for the kinetic effects of Landau damping, as well as reflection from the sheath. He argued that one can expect that, as the electron density approaches zero at the wall, the propagating Langmuir wave will eventually enter a region where $k_x \lambda_{De} \geq 1$, and the kinetic effect of Landau damping should take effect. Baldwin suggested that this Landau damping should have a more pronounced effect in afterglow plasmas since the λ_{De} is greatly reduced due to a decrease in T_{e0} . Ignat¹⁸ performed experiments in which he attempted to verify the theoretical work of Bald-

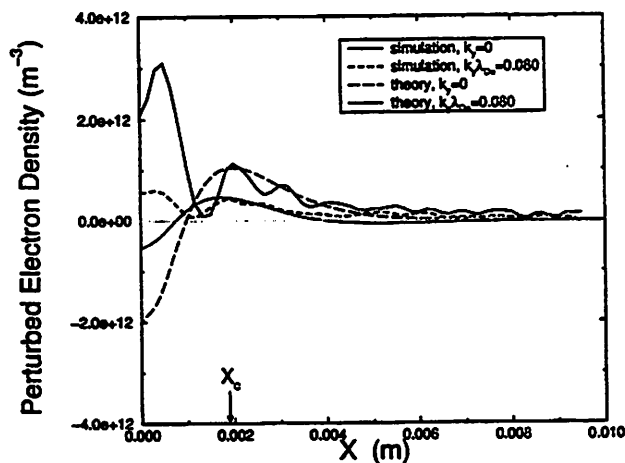


FIG. 12. The amplitude of the electron density perturbation of the second symmetric surface (Tonks–Dattner) mode from the metal boundary ($x = 0$ m) to the midplane ($x = 0.01$ m) of the system. Theory and experiment ($|n_1|$ shown from simulation; n_1 shown from theory) at two different values of k_y , are shown.

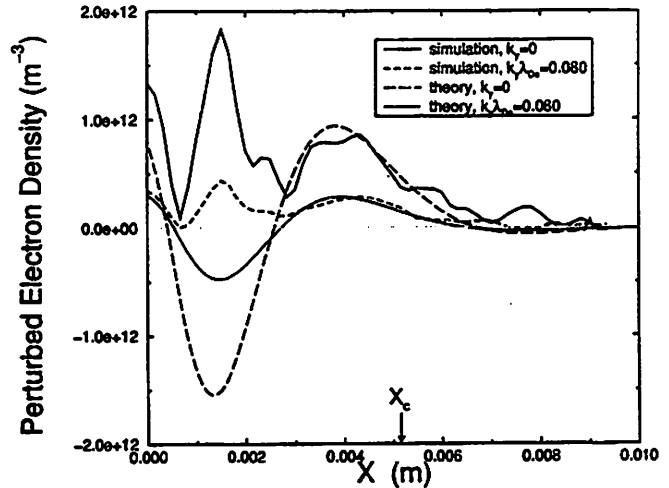


FIG. 13. The amplitude of the electron density perturbation of the third asymmetric surface (Tonks–Dattner) mode from the metal boundary ($x = 0$ m) to the midplane ($x = 0.01$ m) of the system. Theory and experiment ($|n_1|$ shown from simulation; n_1 shown from theory) at two different values of k_y , are shown.

win; however, the agreement between his experimental data and the Baldwin theory seemed to be worse than that obtained with fluid theory. In our simulation, the violation of $k_x \lambda_{De} \ll 1$ is most significant for higher modes and occurs only in a thin region starting near the plasma/sheath boundary and extending to the wall (see Fig. 7). The plasma/sheath boundary is defined as the point where the steady-state potential has dropped by $k_B T_{e0}/2$ from its peak value (at the center). This point is experimentally determined in our simulation to be at $0.0031 \text{ m} = 12 \lambda_{De0}$ from either metal wall. Even though the fluid theory breaks down in this region, the waves are clearly shown to have a well-defined eigenmode structure all the way to the metal wall (in Figs. 9–18), and the resulting inaccuracy does not seem to interfere with the qualitative results.

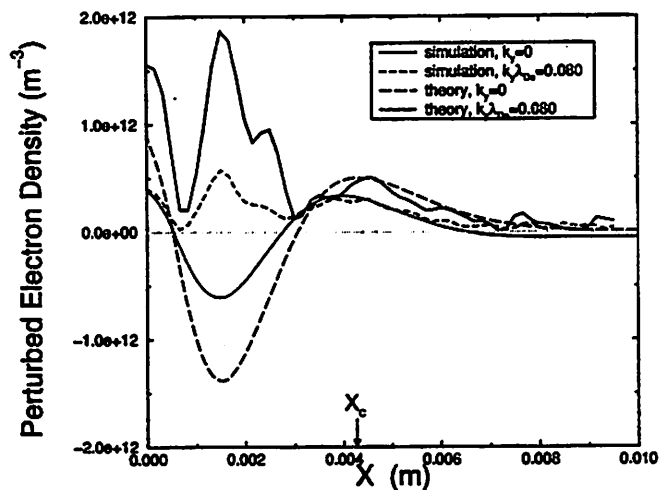


FIG. 14. The amplitude of the electron density perturbation of the third symmetric surface (Tonks–Dattner) mode from the metal boundary ($x = 0$ m) to the midplane ($x = 0.01$ m) of the system. Theory and experiment ($|n_1|$ shown from simulation; n_1 shown from theory) at two different values of k_y , are shown.

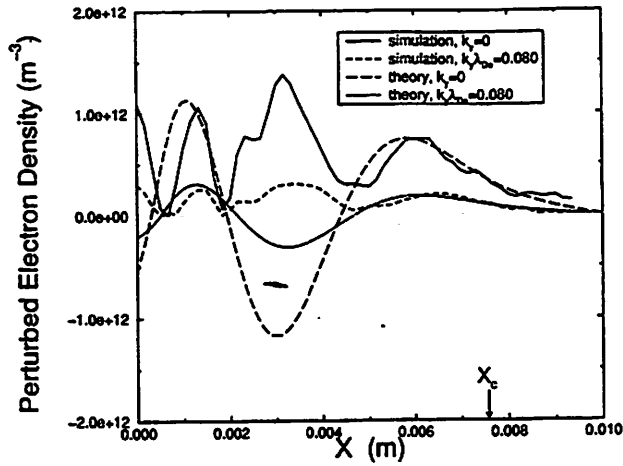


FIG. 15. The amplitude of the electron density perturbation of the fourth asymmetric surface (Tonks–Datner) mode from the metal boundary ($x=0$ m) to the midplane ($x=0.01$ m) of the system. Theory and experiment ($|n_1|$ shown from simulation; n_1 shown from theory) at two different values of k_y , are shown.

We may make some crude estimations of the expected effect of Landau damping, which is significant in a thin region near the plasma walls. In Figs. 19 and 20 we have crudely estimated the perturbation function, $n_1(x)$ of the first and fourth asymmetric modes at $k_y=0$ between the critical point, x_c , and the wall by

$$\Psi_{\text{osc}}(x) = \sin\left(\int_{x_c}^x k_x(x') dx' + \phi\right) \quad (22)$$

and

$$\Psi_{\text{damp}}(x) = e^{-\int_{x_c}^x (\omega_i/\omega_r)(x') k_x(x') dx'}, \quad (23)$$

where the phase, ϕ , at x_c is chosen as a best fit to the measured perturbation, $k_x(x)$ and $\omega_i(x)$ are derived from Eqs. (20) and (21), respectively. This representation neglects any slow variation in the wave amplitude, and further is not valid

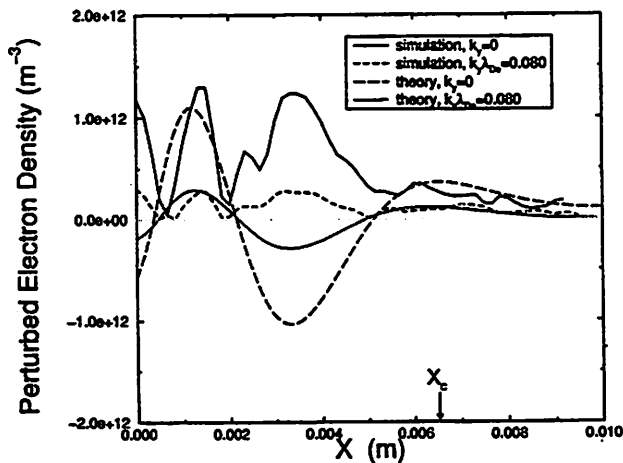


FIG. 16. The amplitude of the electron density perturbation of the fourth symmetric surface (Tonks–Datner) mode from the metal boundary ($x=0$ m) to the midplane ($x=0.01$ m) of the system. Theory and experiment ($|n_1|$ shown from simulation; n_1 shown from theory) at two different values of k_y , are shown.

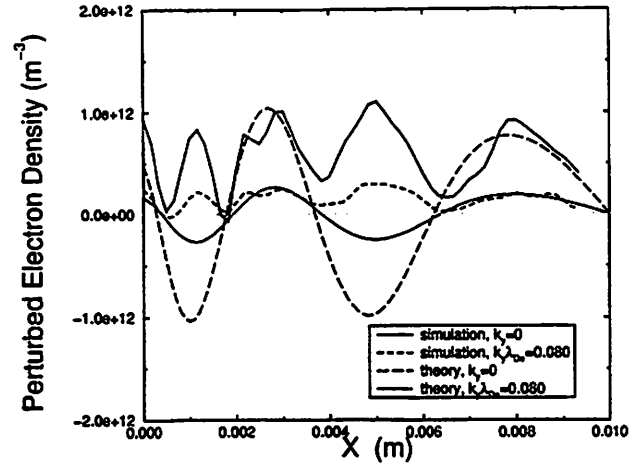


FIG. 17. The amplitude of the electron density perturbation of the first asymmetric body mode from the metal boundary ($x=0$ m) to the midplane ($x=0.01$ m) of the system. Theory and experiment ($|n_1|$ shown from simulation; n_1 shown from theory) at two different values of k_y , are shown.

near x_c . Reflection is also neglected. Still the resulting wave form $\Psi_{\text{osc}}(x)$ (at least for the higher modes) is in qualitative agreement with the simulation and theoretical data. For the fourth mode, the net damping of the wave after reaching the wall is considerably greater than for the first mode; however, it is not severe enough to destroy the resonance. This analysis may help explain the success of the fluid theory. For the higher modes we see that Landau damping occurs in a finite region in the \hat{x} dimension determined by the steady-state plasma density profile. This damping may become more significant in higher Tonks–Datner modes, which are not present for the simulation parameters chosen. As described by Baldwin,¹² the resulting perturbation of the EEPF may reflect off the sheath¹⁹ and interfere constructively or destructively with the standing Langmuir wave.

The above discussion focuses on the one-dimensional case. However, as is clear from our observed density pertur-

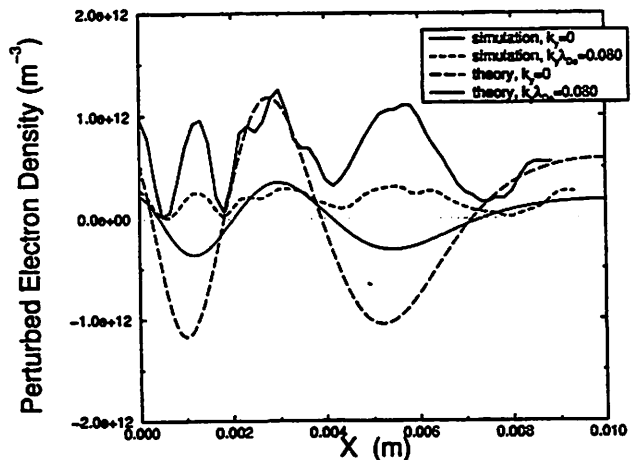


FIG. 18. The amplitude of the electron density perturbation of the first symmetric body mode from the metal boundary ($x=0$ m) to the midplane ($x=0.01$ m) of the system. Theory and experiment ($|n_1|$ shown from simulation; n_1 shown from theory) at two different values of k_y , are shown.

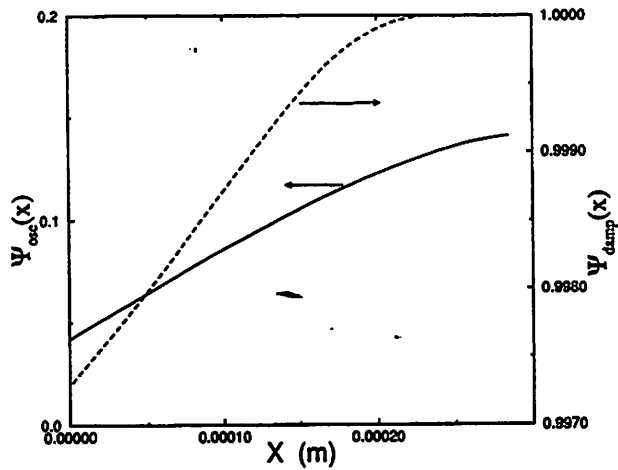


FIG. 19. Approximate solutions for the oscillatory and evanescent parts of the solution for the main asymmetric branch ($k_y=0$).

bations, the addition of axial variation does not greatly alter the picture of trapped Langmuir waves, provided $k_y \lambda_{De}$ is sufficiently small. The axial variation gives the wave vector of the trapped Langmuir wave a component in the axial direction.

Figures 17 and 18 describe waves whose $k_y=0$ cutoff frequencies are above the peak electron plasma frequency. As a result, there is no region of evanescent behavior in $n_1(x)$. We consider these modes to be bulk or body modes. To further justify the distinction between surface and body waves, Figs. 21 and 22 show the measured values of $\Phi_1(x)$ for the first five asymmetric and symmetric modes at $k_y=0$. The fields derived from these profiles are strongest at the plasma edge for the lower modes and stronger toward the central, bulk, region for higher modes.

VI. CONCLUSIONS

In this work we have analyzed and measured a spectrum of thermally excited, electrostatic slow waves that propagate

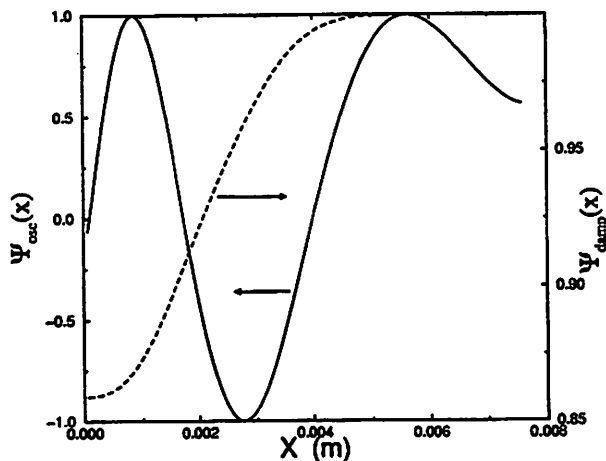


FIG. 20. Approximate solutions for the oscillatory and evanescent parts of the solution for the last detected asymmetric Tonks-Dattner mode ($k_y=0$).

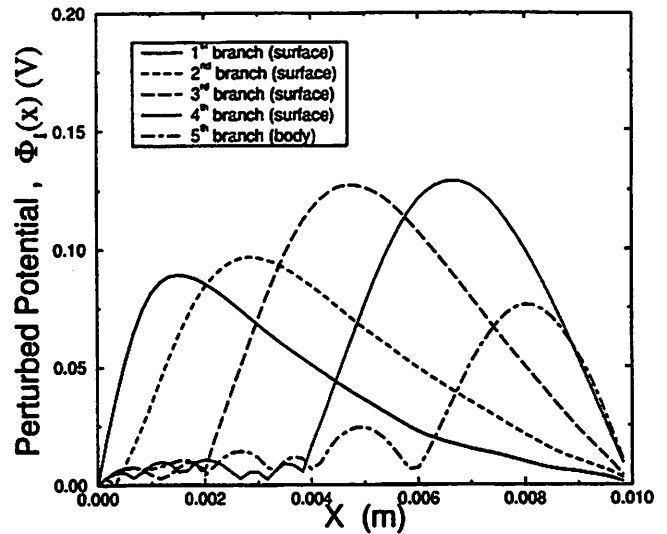


FIG. 21. Amplitude of the electrostatic potential perturbation for the asymmetric surface modes and first asymmetric body mode, $k_y=0$.

along the edge of a nonuniform, thermal, metal bound plasma. The plasma slab is represented by a dc discharge, and is modeled self-consistently via fully kinetic, $2d3v$ PIC simulation with Monte Carlo collisions. The measured dispersion relations are in fair agreement with a linearized, scalar pressure, fluid calculation, although this representation is shown to be invalid over a region of the slab near the plasma sheaths.

Disagreement between the measured and theoretical results, especially for the lower-frequency modes, is most likely due to the approximations made in treating the plasma inhomogeneity, which were used in order to make the theory more tractable.

We have shown that, for our simulation parameters ($T_{e0}=6.02$ eV and $L_x/\lambda_{De}=78$), kinetic effects, which lead to Landau damping, and the breakdown of the adiabatic ap-

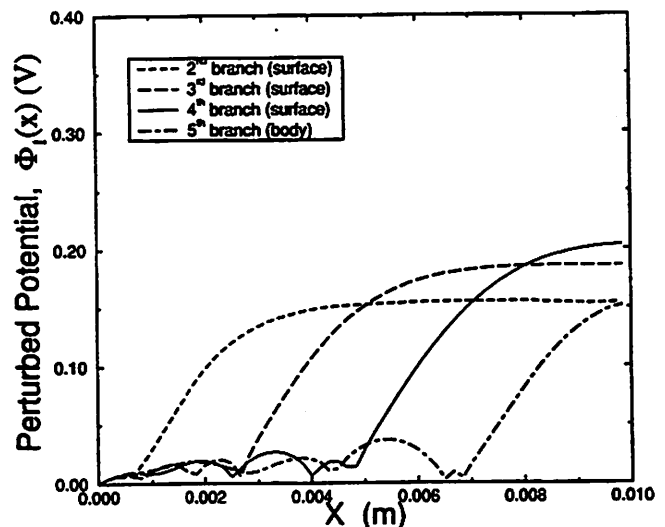


FIG. 22. Amplitude of the electrostatic potential perturbation for the symmetric surface modes and first asymmetric body mode, $k_y=0$.

proximation near the plasma sheath (which has been made in our fluid analysis), do not substantially degrade the usefulness of the perturbed scalar pressure, fluid theory. The fluid theory may be less accurate in describing higher Tonks-Dattner modes that would appear at higher plasma densities and lower electron temperatures (increasing L_x/λ_{De}), since the region over which Landau damping occurs will increase. Future simulation in this regime might shed light on the source of the apparent inaccuracy of Baldwin's kinetic theory.

Simulation at lower neutral pressures might also allow for a direct measurement of the collisionless damping of thermally excited surface modes by examining the linewidths of the PSD measurements. For the neutral pressure and species chosen in our simulation, this effect cannot be observed.

ACKNOWLEDGMENTS

The author thanks Professor C. K. Birdsall for suggesting the study, which has formed the basis of this paper, and also for his continued encouragement and guidance. The technical assistance offered by V. Vahedi in adapting XDPD2 for this work is also greatly appreciated.

This work was supported in large part by ONR-ASSERT N100014-93-1-1389.

- ¹D. J. Cooperberg, Companion paper Phys. Plasmas 5, 853 (1998).
- ²J. C. Nickel, J. V. Parker, and R. W. Gould, Phys. Rev. Lett. 11, 183 (1963).
- ³J. V. Parker, J. C. Nickel, and R. W. Gould, Phys. Fluids 7, 1489 (1964).
- ⁴B. O'Brien, R. W. Gould, and J. Parker, Phys. Rev. Lett. 14, 630 (1965).
- ⁵B. B. O., Jr., Plasma Phys. 9, 369 (1967).
- ⁶B. Kerzar, K. Abrahamsen, and P. Weissglas, Appl. Phys. Lett. 7, 155 (1965).
- ⁷B. Kerzar and P. Weissglas, J. Appl. Phys. 36, 2479 (1965).
- ⁸L. Tonks, Phys. Rev. 37, 1458 (1931).
- ⁹L. Tonks, Phys. Rev. 38, 1219 (1931).
- ¹⁰A. Dattner, Phys. Rev. Lett. 10, 205 (1963).
- ¹¹P. E. Vandenplas, *Electron Waves and Resonances in Bounded Plasmas* (Interscience, New York, 1968).
- ¹²D. E. Baldwin, Phys. Fluids 12, 279 (1969).
- ¹³A. W. Trivelpiece and R. W. Gould, J. Appl. Phys. 30, 1784 (1959).
- ¹⁴C. K. Birdsall and A. B. Langdon, *Plasma Physics Via Computer Simulation* (Adam Hilger, Bristol, England, 1991).
- ¹⁵V. Vahedi and M. Surendra, Comput. Phys. Commun. 87, 179 (1995).
- ¹⁶L. Tonks and I. Langmuir, Phys. Rev. 34, 876 (1929).
- ¹⁷V. Vahedi, G. DiPeso, T. D. Rognien, and C. Birdsall, Phys. Fluids B 5, 2719 (1993).
- ¹⁸D. W. Ignat, Phys. Fluids 13, 1771 (1970).
- ¹⁹H. L. Berk, C. W. Horton, M. N. Rosenbluth, D. E. Baldwin, and R. N. Sudan, Phys. Fluids 11, 365 (1968).

Series resonance sustained plasmas in a metal bound plasma slab

D J Cooperberg and C K Birdsall

Department of Electrical Engineering and Computer Science,
University of California, Berkeley, Berkeley, CA 94720, USA

Received 22 August 1997, in final form 20 January 1998

Abstract. The characteristics of series resonance sustained argon plasmas are measured by particle-in-cell Monte Carlo simulation and analysed with various theoretical models. These measurements include discharge gap impedance which is shown to be nearly pure resistive, EEPFs, electron heating profiles, electric field structure and electron density profiles over a range of applied frequencies (110–470 MHz) and neutral gas pressures (2–300 mTorr). The scaling laws, which predict the density and sheath width dependence on operating frequency as ω_p^3 and ω_p^{-1} respectively, are verified. These resonant discharges are driven with low applied voltages ($\sim T_e$) and are shown to produce low-voltage plasmas. A heating mode transition between a high-pressure collisional regime and a low-pressure collisionless regime is discussed. Also the self-tuning of the discharges, needed to maintain resonance, is explained.

1. Introduction

This study is directed toward the understanding of resonantly sustained RF and high-frequency parallel-plate discharges which are shown to exhibit attractive qualities for materials processing. Conventional capacitively coupled, parallel-plate RF discharges tend to require high applied voltages and/or high neutral pressures which make them unattractive for some current fabrication processes.

The resonance exhibited by this metal bound plasma is often referred to as the *series resonance* and arises from the balancing of the capacitance of the sheaths with the inductance of the plasma bulk. The series resonance is also the cut-off for a main asymmetric surface wave which propagates along and near the metal/plasma boundary [1, 2].

It is observed via simulation that an applied signal of fixed frequency can maintain a discharge whose density profile yields a series resonance near the applied frequency. Since the plasma impedance approaches a pure resistance at this frequency, exceptionally low applied voltages can be used by comparison with conventional capacitively coupled discharges where the diode impedance is nearly pure capacitive.

A detailed review of early work on resonance sustained, radio frequency gas discharges was given by Taillet [3]. In this work the enhancement, at resonance, of the RF electric field in a planar capacitively driven discharge is emphasized. A simple model of a collisional homogeneous plasma slab between two sheath regions in which the electron density, $n_e = 0$, is developed from previous theoretical work summarized by Vandenplas [4]. Justification for extending the results to inhomogeneous plasmas was based on a variational calculation of Crawford

and Kino [5], which showed that the plasma density could be replaced by the average plasma density in an expression for the internal fields at resonance. Taillet's analysis assumes that the resonance enhanced field strength remains in the linear regime while still providing sufficient electron heating to sustain the plasma. A relation, which equates the ohmic power absorbed by the plasma electrons to the energy lost due to ionization, excitation, and diffusion characterizes the discharge. It is shown that stable and unstable equilibria exist when the discharge is driven with a constant-amplitude RF voltage. Some experimental results given by Taillet [3] include measurement of the plasma electric field using electron beam probing. The electric field is observed to be approximately ten times greater in magnitude than the vacuum field and the phase of the field in the plasma bulk is opposite to that at the plasma edge. Measurements of the plasma profile deduced from photometric data, along with density measurements taken from a Langmuir probe, were used to verify further that the discharges were indeed operating at the series resonance.

The study of resonance sustained discharges was significantly advanced by the theoretical and experimental work of Godyak [6]. A homogeneous model for steady-state low-pressure rf discharges has been developed [7] which is used to predict the total impedance across a discharge gap. This impedance is taken to be the sum of plasma, space-charge sheath and stochastic (interaction with moving sheath walls) impedances. The total impedance is then used in combination with an energy balance equation to predict the internal properties of the rf discharge including the current–voltage characteristic and the dependence of plasma density and discharge voltages on applied frequency. An important result is that the

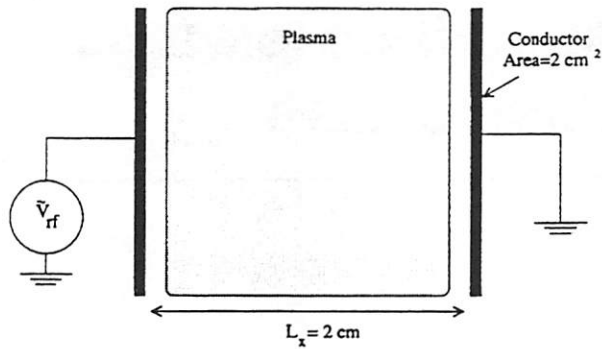


Figure 1. Schematic diagram of the simulation model.

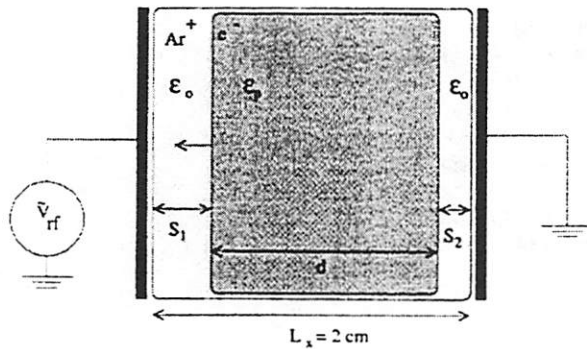


Figure 2. Schematic diagram of the homogeneous model.

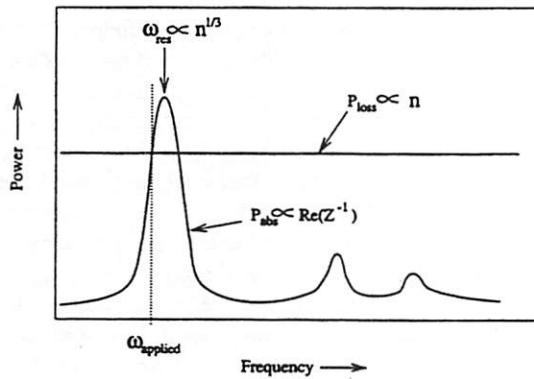


Figure 3. Sketch of absorbed power as a function of frequency. Stable operation (with respect to density and electron temperature fluctuations) occurs at ω_{applied} with an external voltage source. Stable operation occurs at the other intersection of P_{abs} and P_{loss} with an external current source.

plasma density is a double-valued function of the applied voltage signal, and that a minimum applied voltage exists. Experimental verification of this double-valued behaviour was presented by Godyak and Popov [8]. In further experiments by Godyak and Popov [9], resonant discharges are maintained at a theoretically predicted minimum applied voltage and resonant frequency. Scaling laws including $n \propto \omega_{rf}^3$ and $s/T_e \propto \omega_{rf}^{-1}$, where n is the peak plasma density and s is the average sheath thickness, are also verified. The homogeneous analysis has been extended to the inhomogeneous plasma model [9–11] which results in the appearance of form factors and scaling factors which

do not greatly effect the qualitative predictions of the model.

Here we use particle-in-cell Monte Carlo (PIC–MCC) simulation [12] to continue the study of these resonantly sustained discharges. This self-consistent method, which, because it is based on first principles, is able to capture kinetic and non-local effects which are difficult to model with a fluid approach, has been used in prior studies to model RF discharges which are used in materials processing. For example, Vahedi *et al* [13] shows excellent agreement between the electron energy distribution functions (EEDFs) measured by Godyak *et al* [14] and those produced by PIC–MCC simulation. Electron heating profiles were also measured, showing enhanced heating in the sheath regions. In another work, Vahedi *et al* [15] verified the frequency scaling laws for capacitive RF discharges using two-dimensional PIC–MCC simulation. Surendra and Graves [16] used PIC–MCC simulation to study RF glow discharges in helium over a range of conditions. Their findings included the relative importance of stochastic and ohmic sheath heating versus ohmic bulk heating in different operating regimes, and the detection of a hot-electron tail. The effects of secondary electron emission are also investigated.

Our PIC–MCC simulation will focus on resonantly sustained parallel-plate discharges (in argon) operated over a range of frequencies and neutral gas pressures. In this study we will present measurements of the steady-state sheath potential, discharge gap impedance, scalings of plasma density and sheath width with frequency, field structure at the fundamental and higher harmonics, plasma density profiles, electron energy probability functions (EEDFs) both averaged and as a function of space and time and electron heating profiles. We will compare with Godyak's theory [6] and fluid theory [2] where possible.

Of particular interest is a set of computer experiments in which p_{argon} is varied with a fixed ω_{rf} . The mechanism of electron heating is studied in these simulations. A transition is seen between the low- ($\lesssim 100$ mTorr) and high-pressure regimes in which the time averaged $J_{\text{electron}} \cdot E$ profile changes forms. In the high-pressure regime, these $J_{\text{electron}} \cdot E$ profiles are in agreement with a modified fluid calculation [2] which includes an electron momentum transfer collision term. At these higher pressures, the plasma is well modelled by the collisional fluid equations and the heating is ohmic.

At lower pressures, which are desirable for many etching processes, the heating cannot be modelled as ohmic. The electron heating profiles show a wavelike structure as a result of the strong resonant surface wave fields located at the plasma edge. These strong surface fields produce a hot-electron population. Particle–wave interactions are especially demonstrated by regions of negative heating. A detailed study of the electron heating mechanism at low pressure helps us determine and understand electron energy distribution functions which are essential in determining plasma composition.

This work is structured as follows. We begin, in section 2, with a description of the 1d3v model used to study the parallel plate discharge at RF and high frequencies

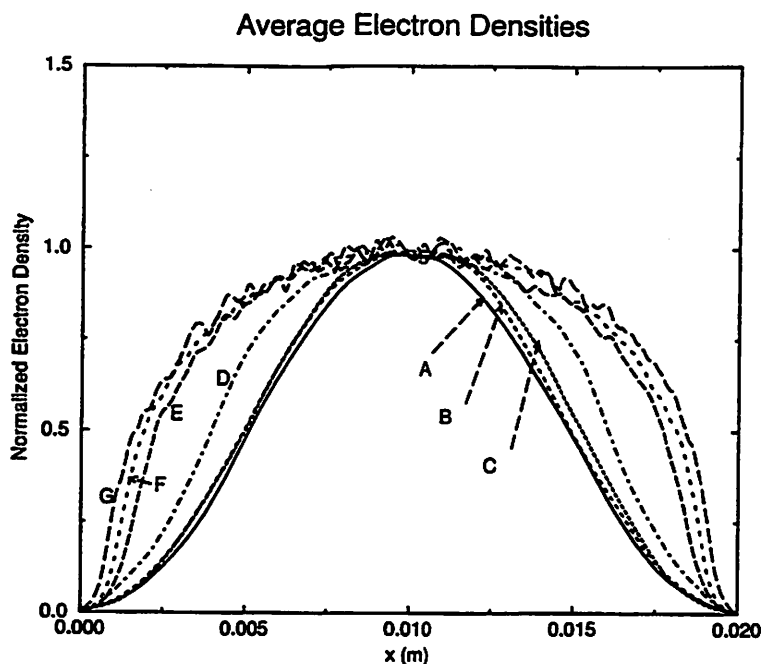


Figure 4. Time-averaged normalized electron densities for cases A–G of table 1.

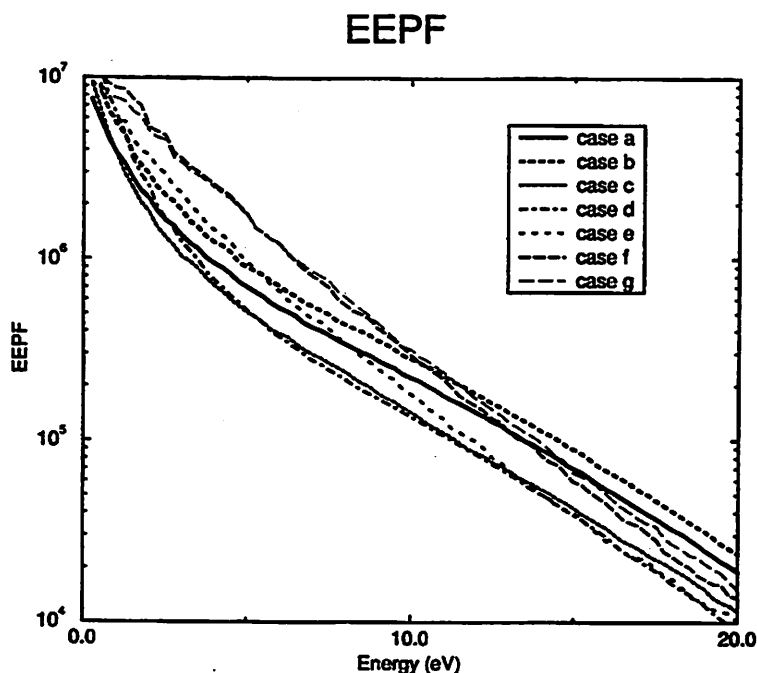


Figure 5. Electron energy probability function (au) for cases A–G of table 1. Note the presence of a bi-Maxwellian distribution at lower frequencies (which correspond to lower plasma densities) ($\rho_{\text{argon}} = 10$ mTorr).

(HF). Next, in section 3 we briefly review the theoretical model of Godyak and also the fluid model used to compare with measured electron heating profiles and discharge gap impedances. A brief discussion of discharge stability will also be given. The results obtained from simulation are presented in section 4. Further results and a discussion of the electron heating at low pressures are given in section 5. Comparison with theory is made where possible. Conclusions are presented in section 6.

2. Simulation model

In this study an argon discharge (1d3v) is sustained by applying a RF (or HF) driving voltage. The steady-state discharge which forms is shown to exhibit a series resonance at, or near, the applied frequency. The electrostatic PIC–MCC code, XPDP1 [17], is used for this study. This code allows for 1d3v simulation of a plasma with metal boundaries and an external driving circuit.

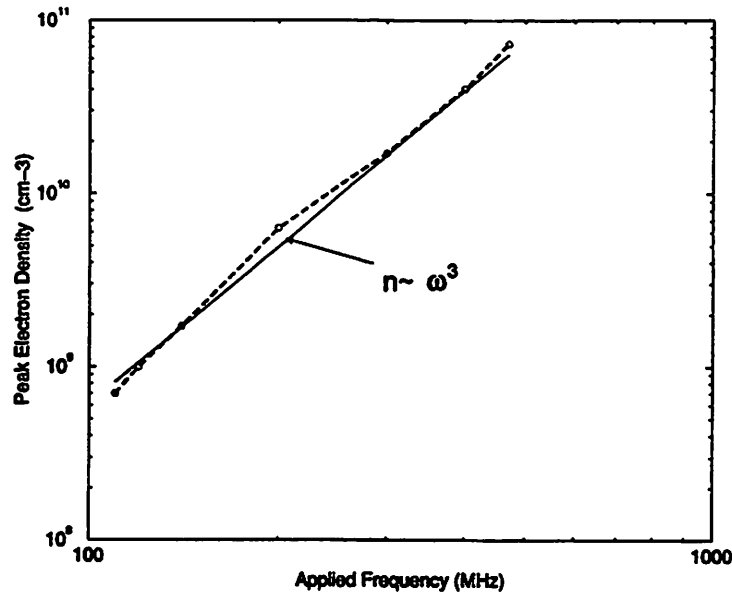


Figure 6. ω_{rf} against $n_{e,peak}$ for fixed $p_{argon} = 10$ mTorr.

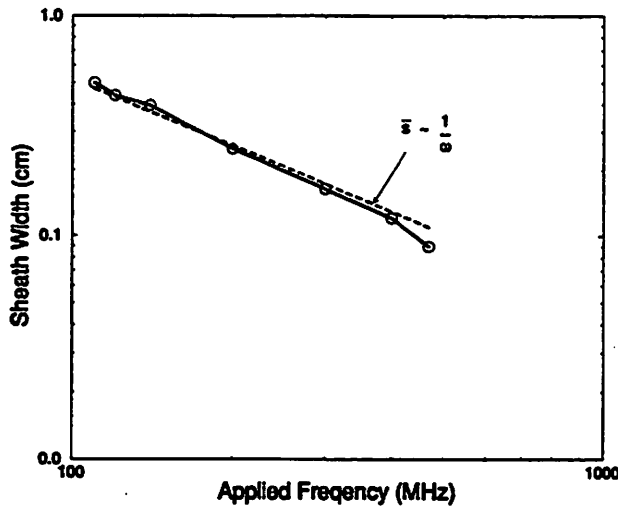


Figure 7. ω_{rf} against \bar{s} , average sheath width, for fixed $p_{argon} = 10$ mTorr.

Secondary emission is permitted in this code, but, for this study, the secondary-emission coefficients have been set to zero in anticipation of the low-voltage discharges achieved in which secondary emission is negligible.

The simulations incorporate a Monte Carlo collision (MCC) package [18] which allows for the self-consistent formation of the discharge. The following reactions are included.

- (1) $e + Ar \rightarrow e + Ar$ (momentum transfer)
- (2) $e + Ar \rightarrow e + Ar^*$ (excitation)
- (3) $e + Ar \rightarrow e + Ar^+ + e$ (ionization)
- (4) $Ar^+ + Ar \rightarrow Ar + Ar^+$ (charge exchange)
- (5) $Ar^+ + Ar \rightarrow Ar^+ + Ar$ (scattering).

A schematic diagram of our model is shown in figure 1. The separation between the metal plates, as shown, is

2.0 cm. The area of the discharge is chosen to be 2.0 cm². We have chosen to drive the discharge with an ideal voltage source for simplicity, although more sophisticated circuit elements may be modelled. Neutral pressures reported on vary from 2–300 mTorr. Applied frequencies range from 110–470 MHz; higher frequencies are computationally expensive to model because of the smaller simulation time-step needed and the resulting higher plasma densities which require the use of more computer particles.

The simulation time-step is chosen to satisfy $\omega_{pe}\Delta t < 0.2$ [19]. An explicit time integration is used since frequencies near the electron plasma frequency must be resolved. The simulation grid size is chosen to ensure resolution of the plasma sheaths with $\lambda_{De}/\Delta x \gtrsim 1$.

In order to arrive at steady-state discharges, an initial uniformly loaded plasma is used to start the simulation. The initial density is chosen to be on the order of the final (average) plasma density. This scheme, while not easily duplicated in the laboratory, has the advantage (over starting from zero plasma density) of decreasing the run-time needed to reach equilibrium and allows for the use of an ideal voltage source operating at a fixed low voltage ($\sim T_e$).

3. Theoretical analysis

3.1. The homogeneous plasma model

We will discuss two theoretical models for the resonant RF discharge, gaining insight from both. First we consider the steady-state RF discharge theory developed by Godyak [6] and Lieberman and Lichtenberg [20]. Here we will re-derive some of the important results from this theory using the homogeneous plasma approximation. A similar analysis for the inhomogeneous plasma introduces form factors into the results [6], which do not affect the qualitative behaviour.

The homogeneous model assumes uniform ions with $\omega_{pi}^2 \ll \omega_{rf}^2$, no electrons in the sheath regions and $n_e =$

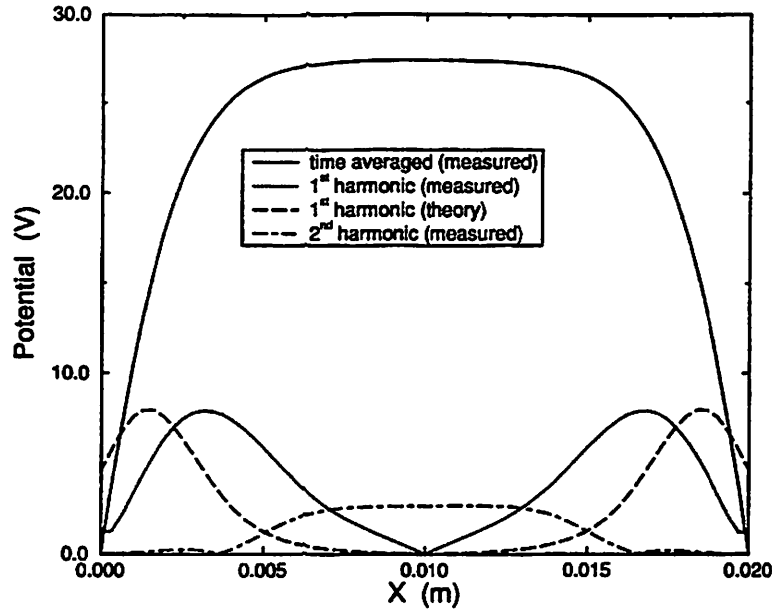


Figure 8. Simulation results for the spatial dependence of the time averaged (DC), fundamental, and second-harmonic potential signal amplitude. A theoretical prediction, based on the fluid model (section 3.2) for the amplitude of the potential signal at the fundamental frequency, is also shown (experiment C).

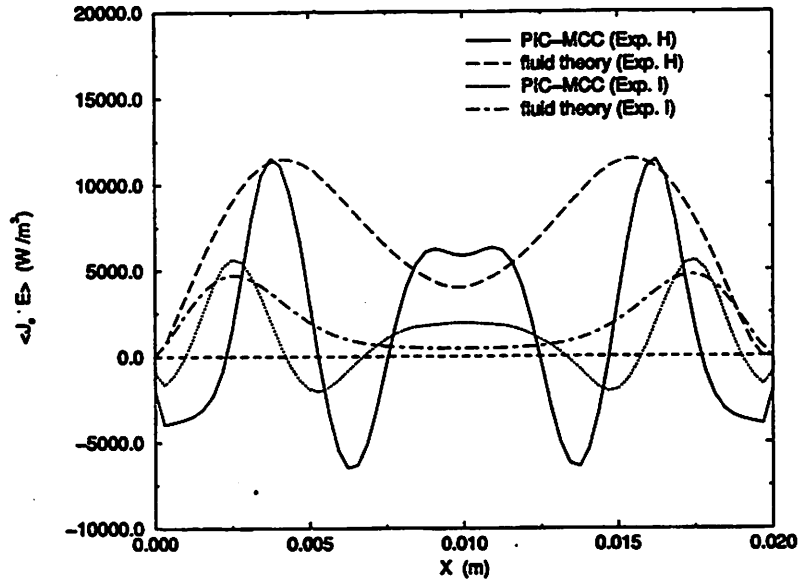


Figure 9. Electron heating profile, $J_e \cdot E$ (case H, $p_{argon} = 2$ mTorr; and case I, $p_{argon} = 10$ mTorr).

$n_i = n_0$ in the central region (figure 2). Current is constant through the discharge and is approximately equal to the electron conduction current in the neutral region, with the assumption

$$\frac{\omega_{pe}^2}{\omega_{rf}^2} \gg \left(1 + \frac{\nu_m^2}{\omega_{rf}^2}\right)^{1/2} \quad (1)$$

where ν_m is the electron momentum collision frequency, and is equal to the displacement current in the sheath regions. The inhomogeneous extension of the model makes the same assumptions except that it allows for a nonuniform equilibrium plasma density profile. The discharge gap

impedance (neglecting low-frequency ion contributions), as seen by the voltage source, is then

$$\begin{aligned} Z(\omega) &= \frac{s_1}{i\omega A\epsilon_0} + \frac{s_2}{i\omega A\epsilon_0} + \frac{d}{i\omega A\epsilon_p} \\ &= \frac{2\bar{s}}{i\omega A\epsilon_0} + \frac{d}{i\omega A\epsilon_p} \end{aligned} \quad (2)$$

with

$$\epsilon_p = \epsilon_0 \left[1 - \frac{\omega_{pe}^2}{\omega(\omega - i\nu_m)}\right] \quad (3)$$

and

$$s_{1,2}(t) = \bar{s} \pm a \cos(\omega t) \quad (4)$$

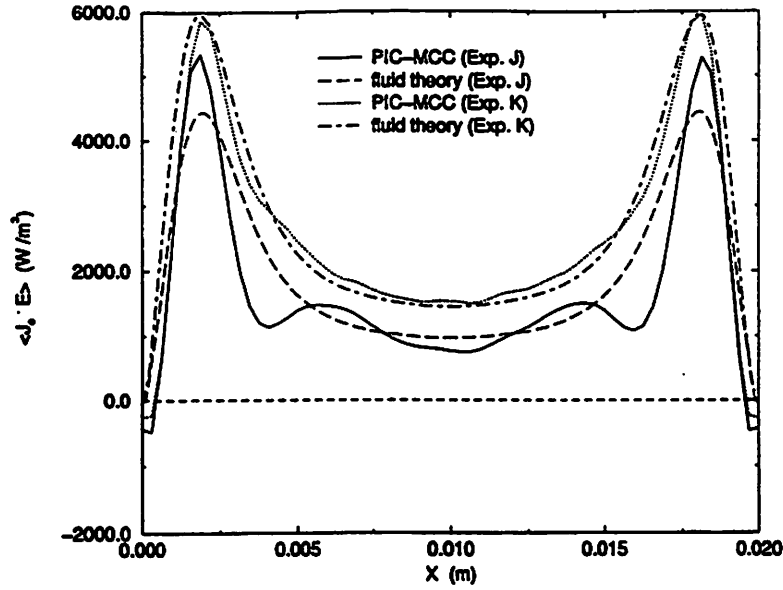


Figure 10. Electron heating profile, $J_e \cdot E$ (case J, $p_{\text{argon}} = 100$ mTorr; and case K, $p_{\text{argon}} = 300$ mTorr).

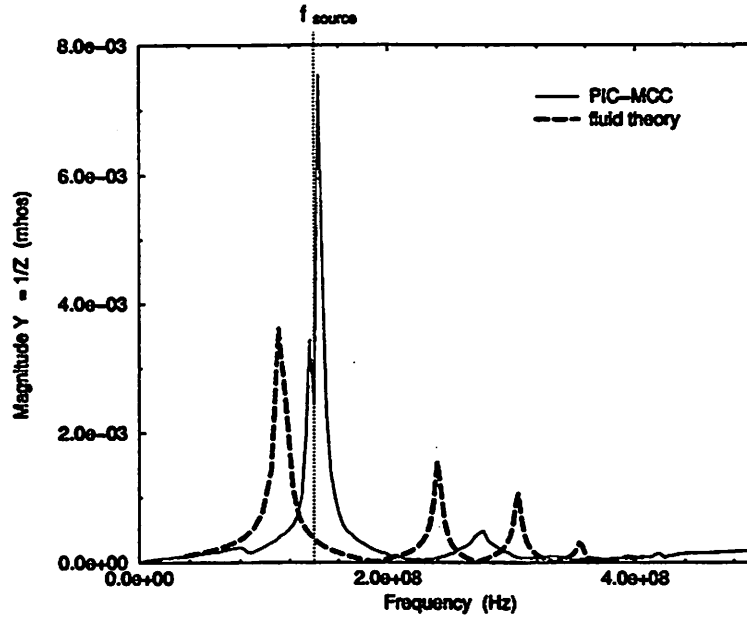


Figure 11. Magnitude of discharge gap admittance (case I, $f_{\text{rf}} = 1.4 \times 10^8$ Hz).

where $s_{1,2}(t)$ describes the position of the sheaths at either side of the discharge (figure 2) and a is the amplitude of the sheath oscillations. Setting $Z(\omega) = 0$ defines the series resonance (or current resonance, $Y(\omega) \rightarrow \infty$)

$$\omega_{sr} \equiv \omega_p \left(\frac{2\bar{s}}{L} \right)^{1/2} \quad \text{for } v_m \rightarrow 0. \quad (5)$$

Using equation (2), one can readily express the power supplied by the external voltage source as $\text{Re}(\bar{V}^2/Z)/2$. Next, an expression for the power loss in the plasma is needed, which can be equated to the power supplied in order to derive an expression relating the plasma density to the applied voltage. To find the power absorbed by the plasma,

we need to know the electron temperature. Balancing the outgoing particle flux with ionization gives the condition [20]

$$2n_s u_B(T_e) A = K_{iz}(T_e) n_s n_0 A d \quad (6)$$

$$\frac{v_{iz}(T_e)}{u_B(T_e)} = \frac{1}{n_s d e^{-1/2}} \quad (7)$$

which determines the electron temperature (n_s is the plasma density at the sheath edge; the sheath edge is defined by the position at which the plasma potential drops by $k_B T_e/2$ from the mid-potential; u_B is the Bohm velocity, defined by $\sqrt{k_B T_e/m_i}$; n_s is the neutral gas density, and $v_{iz} = K_{iz} n_s$ is the ionization frequency). A Maxwell-Boltzmann distribution is assumed for the electrons. We

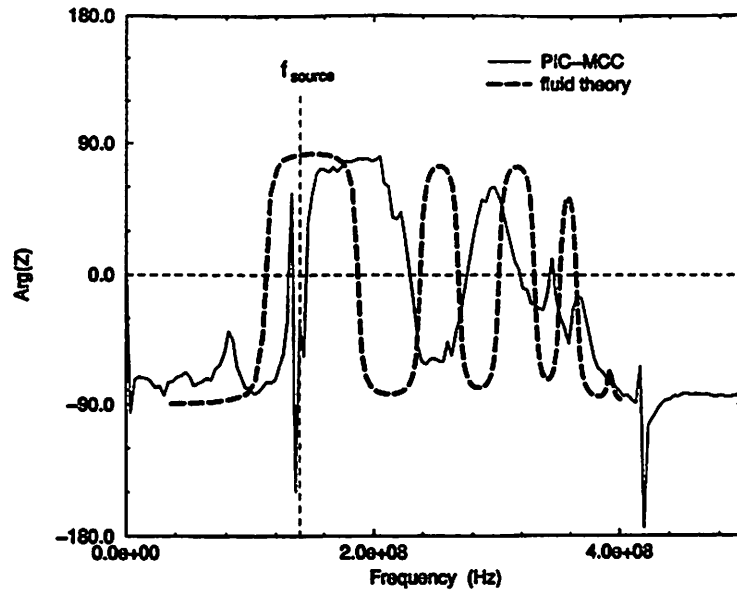


Figure 12. Phase of discharge gap impedance (case I, $f_d = 1.4 \times 10^8$ Hz).

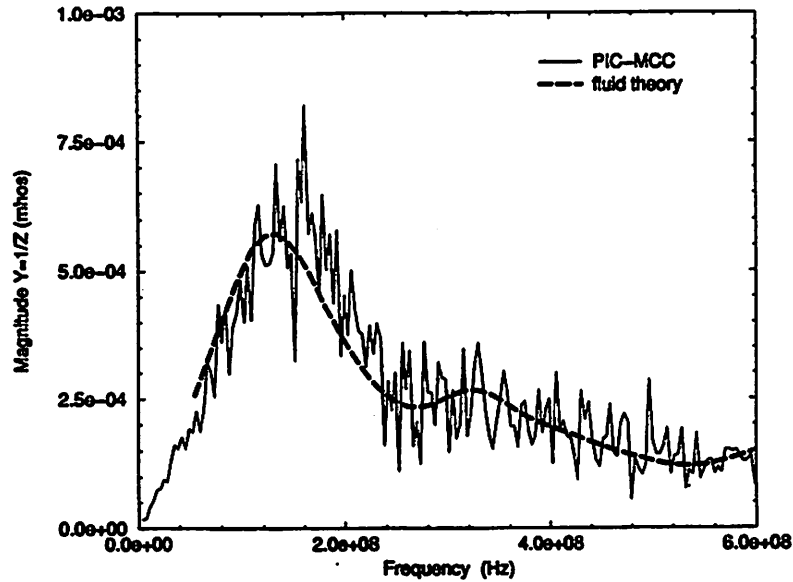


Figure 13. Magnitude of discharge gap admittance (case K, $f_d = 1.4 \times 10^8$ Hz).

may then write an expression for the power loss as

$$P_{loss} = 2en_s u_B A \mathcal{E}_T(T_e) \quad (8)$$

where \mathcal{E}_T includes collisional losses and ionization loss in the plasma bulk, and electron and ion kinetic energy loss at the walls. \mathcal{E}_T is independent of plasma density provided nonlinear processes such as stepwise ionization and recombination can be ignored. Balancing the supplied power, $\text{Re}(\tilde{V}^2/Z)/2$, with the power loss produces

$$\frac{\omega_{pe}^2}{\omega^2} = \frac{L}{2\bar{s}} \left[1 \pm \frac{v_m}{\omega} \left(\frac{\tilde{V}^2}{V_{min}^2} - 1 \right)^{1/2} \right]$$

where $V_{min}^2 = \frac{4e^{-0.5} v_m u_B L^2 m_e \mathcal{E}_T}{ed}$. (9)

V_{min} is the minimum operating voltage which will sustain the plasma and is dependent on discharge dimensions, T_e (through u_B and \mathcal{E}_T) and gas pressure (through v_m). For sufficiently high- Q plasmas (i.e. low pressures) and low applied voltages we find that the peak plasma density is determined by the applied drive frequency and not the drive amplitude. Note that when $\tilde{V} = V_{min}$ or $v_m = 0$, the frequency is $\omega = \omega_{pe} \sqrt{2\bar{s}/L} \equiv \omega_{sr}$.

As yet undefined is the time average sheath width, \bar{s} . A derivation by Godyak [6, 7] is based on enforcing zero time averaged conduction current through the sheath. This is reasonable due to the symmetry of the driving signal and the desire for a steady-state solution. To summarize, the

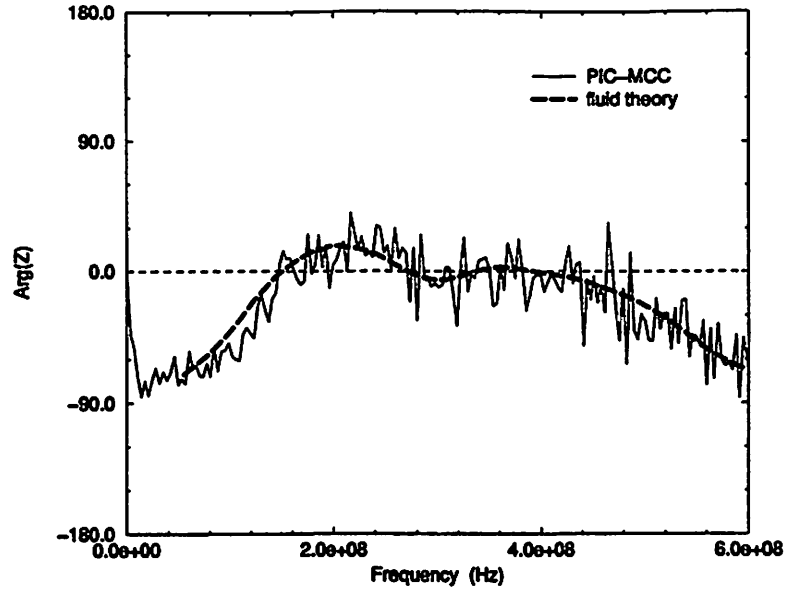


Figure 14. Phase of discharge gap impedance (case K, $f_{rf} = 1.4 \times 10^8$ Hz).

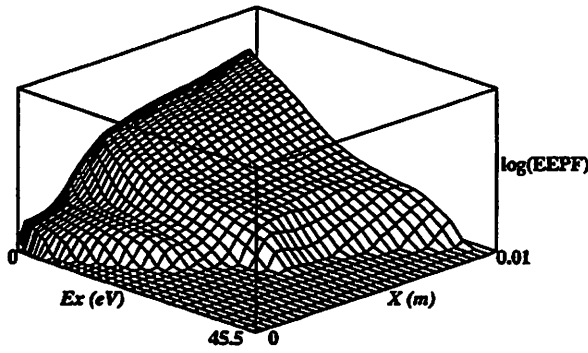


Figure 15. Time-averaged electron energy probability function (au), EEPF, as a function of x from the midplane ($x = 0.01$ m) to the wall ($x = 0$ m). The electron kinetic energy in x is $E_x = m_0(v_x - \langle v_x \rangle)^2/2$. The EEPF is shown over three-orders of magnitude. (Experiment H, $p_{\text{Argon}} = 2$ mTorr.)

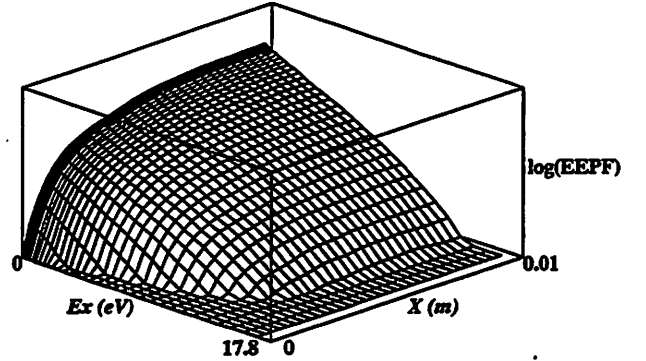


Figure 16. Time-averaged electron energy probability function (au), EEPF, as a function of x from the midplane ($x = 0.01$ m) to the wall ($x = 0$ m). The EEPF is shown over four orders of magnitude. (Experiment K, $p_{\text{Argon}} = 300$ mTorr.)

conduction currents through the sheaths are

$$J_i = en_0 u_B \quad \text{and} \quad J_e = en_0 u_B \left(\frac{m_i}{2\pi m_e} \right)^{1/2} e^{eV_s(t)/k_B T_e} \quad (10)$$

where $V_s(t)$ is the voltage drop across a sheath. Poisson's equation may be used to relate $V_s(t)$ to $s_{1,2}(t)$ with the result that

$$V_{s_{1,2}}(t) = \frac{en_0}{\epsilon_0} s_{1,2}^2(t). \quad (11)$$

We may now write the time average conduction current leaving either sheath as

$$\begin{aligned} 0 &= \int_0^{2\pi/\omega} dt (J_i + J_e) \\ &= \int_0^{2\pi/\omega} dt \left[en_0 u_B + en_0 u_B \left(\frac{m_i}{2\pi m_e} \right)^{1/2} e^{-s_{1,2}^2(t)/\lambda_{De}^2} \right] \end{aligned} \quad (12)$$

(where $\lambda_{De}^2 = \epsilon_0 k_B T_e / (n_0 e^2)$) which, after substituting (4) for $s_{1,2}(t)$ and making the change of variable, $\theta = \omega t$, leads to

$$2\pi = \int_0^{2\pi} d\theta \left[\left(\frac{m_i}{2\pi m_e} \right)^{1/2} e^{-[(\bar{s} \pm a \cos(\theta))^2 / \lambda_{De}^2]} \right]. \quad (13)$$

This equation has been evaluated numerically by Godyak [6, 7]. The result can be summarized as follows. As $a \rightarrow 0$, \bar{s} approaches the DC sheath value, $\lambda_{De} (\ln(m_i / (2\pi m_e)))^{1/2}$. At larger a , \bar{s} asymptotes to a .

In the approximation $\bar{s} \approx a$, we equate conduction current and the driving current which produces

$$\bar{I} = -en_0 A \frac{ds_{1,2}}{dt} = en_0 A \omega \bar{s} \sin(\omega t) = \text{Re} \left(\frac{\bar{V}}{Z} \right). \quad (14)$$

With $Z(\omega_{sr}) = v_m m L \epsilon_0 / n_0 e^2 A$ from equations (2) and (3), we can solve for \bar{s} . The result is

$$\bar{s} = \frac{e V_{min}}{\omega v_m m_e L \epsilon_0} \quad (15)$$

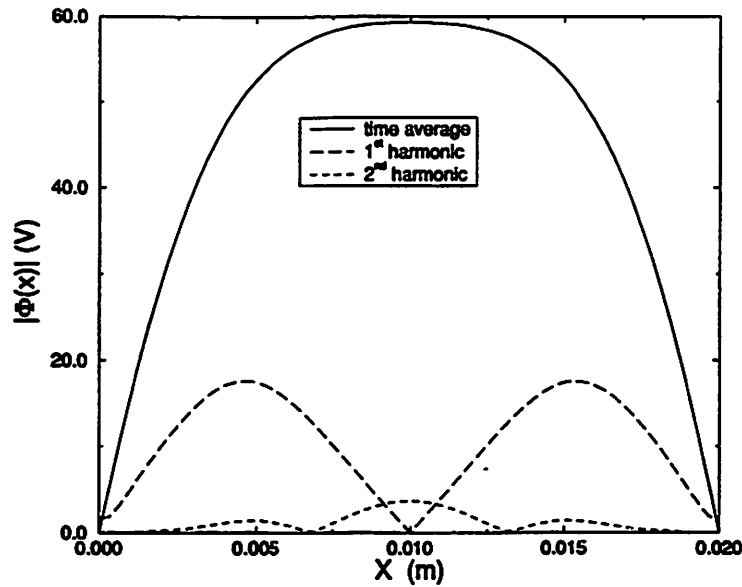


Figure 17. Simulation results for the spatial dependence of the time averaged (DC), fundamental, and second-harmonic potential signal amplitude (experiment H). The phases of these signals are nearly constant in x .

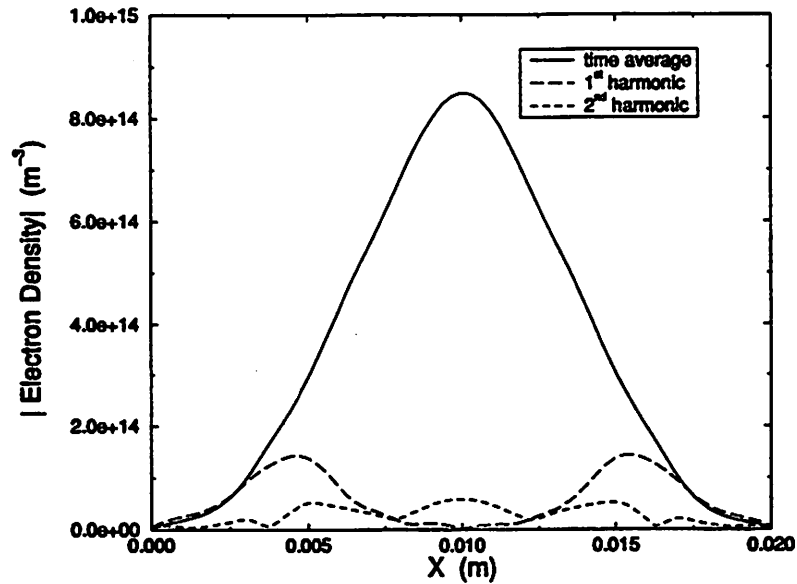


Figure 18. Simulation results for the spatial dependence of the time averaged (DC), fundamental, and second-harmonic electron density signal amplitude (experiment H). The phases of these signals are nearly constant in x .

which may be inserted into our expression for the series resonance to give

$$\omega = \omega_{pe} \sqrt{\frac{2(eV_{min}/\omega v_m m_e L \epsilon_0)}{L}} \quad (16)$$

which produces the scaling law,

$$n \sim \omega_{rf}^3. \quad (17)$$

This is in contrast to the capacitively coupled RF discharge scaling, $n \sim \omega_{rf}^2$.

3.2. The Inhomogeneous fluid model

In the homogeneous model described above (and the extension of this theory to account for plasma inhomogeneity), the plasma is dynamically modelled as a cold fluid with dielectric constant given by equation (3). The sheath voltages are also assumed large enough to completely expel electrons from the sheath regions, and the displacement current in the plasma is considered negligible (which is justified for $\omega \ll \omega_{pe}$). These approximations are of increased validity when the equilibrium sheath width is much larger than the undriven sheath width, because the region over which the electron density drops to zero (on the order of a few λ_{De}) can be neglected.

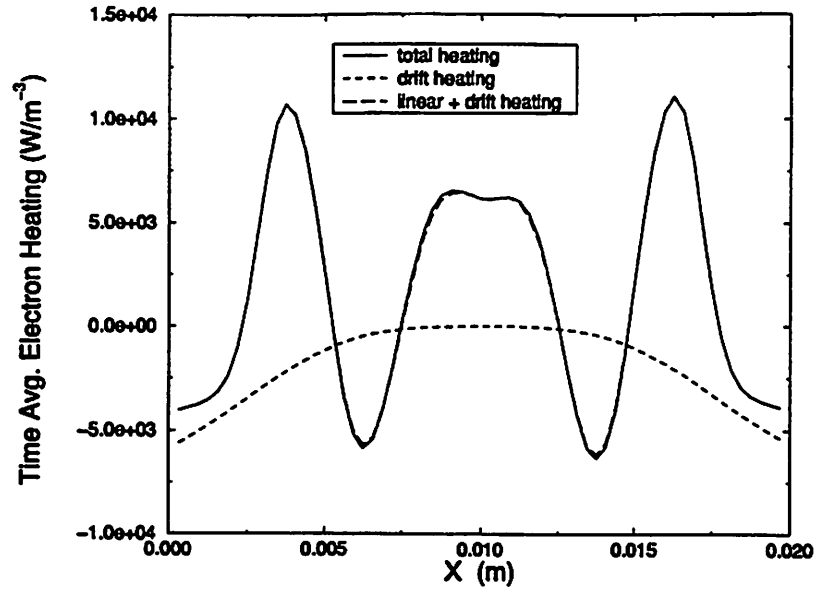


Figure 19. Total, 'linear', and drift electron heating for experiment H. The total electron heating is calculated as $\langle J_e \cdot E \rangle_t$, the drift heating is calculated as $\langle J_e \rangle_t \cdot \langle E \rangle_t$, and the 'linear' heating is computed from a v -space integration of $(m_e v^2/2)(\theta/m)(\hat{e}_i \cdot \delta f_i / \partial v)_t$ (see section 5.2).

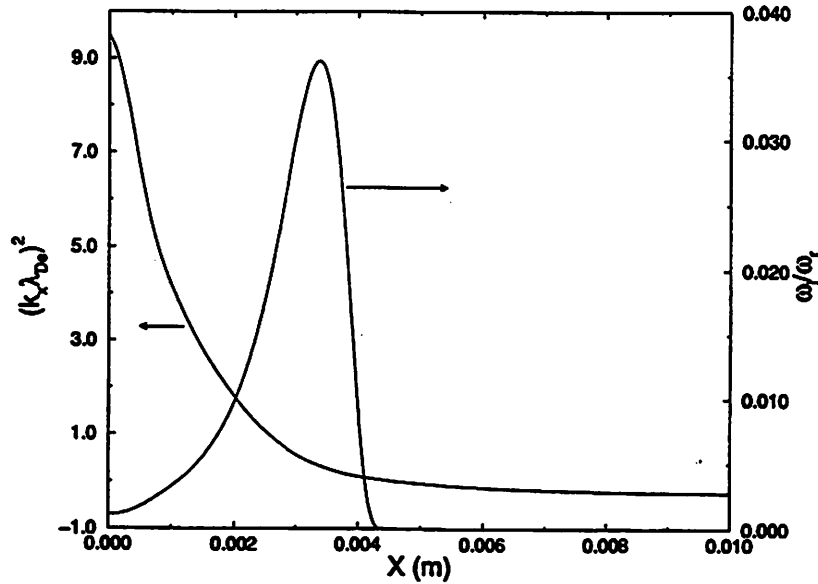


Figure 20. Local wavenumber, k_x (in the long-wavelength limit), and the associated linear Landau damping rates predicted for Maxwellian distributions are plotted from the mid-plane ($x = 0.01$ m) to the wall ($x = 0$ m). (Experiment H.)

These approximations, which helped lead to analytic expressions for the current-voltage characteristic and various scaling laws, are not needed if we alternately use a linearized fluid model of the inhomogeneous metal bound plasma slab [2] which is similar to that used by Parker *et al* [21] in describing the electron resonances of dielectric bound cylindrical plasmas. This model allows for surface fields to penetrate into the plasma and is most useful when considering sheath widths which are on the order of a few λ_{De} . A derivation of this model is given by Cooperberg [2] for the collisionless 2d3v plasma slab. Here we include an electron collision term in the perturbed electron momentum equation (and simplify to 1d). This leads to a modification of the governing equation for the

perturbed plasma potential, which becomes

$$\begin{aligned} \nabla^2 \nabla^2 \Phi_1 - \frac{1}{\gamma} \left(\frac{\nabla f}{f} \cdot \nabla \right) \nabla^2 \Phi_1 - \frac{1}{\gamma} \nabla f \cdot \nabla \Phi_1 \\ + \left[\frac{1}{\gamma \lambda_{De}} \left(\frac{\omega^2}{\omega_{pe0}^2} - \frac{i v_m \omega}{\omega_{pe0}^2} - f \right) \right. \\ \left. - \frac{1}{\gamma} \nabla \cdot \left(\frac{\nabla f}{f} \right) \right] \nabla^2 \Phi_1 = 0 \end{aligned} \quad (18)$$

where ω_{pe0}^2 and λ_{De} are the peak electron plasma frequency and peak Debye length, and f describes the steady-state electron density profile and can be modelled theoretically, as by Parker *et al* [21], or obtained directly from simulation [2]. The new expression for the electron current density

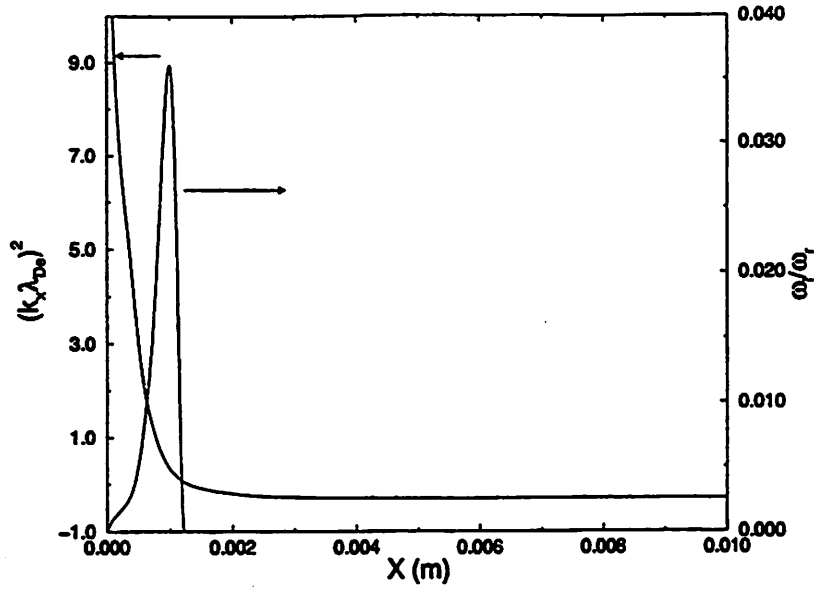


Figure 21. Local wavenumber, k_x (in the long-wavelength limit), and the associated linear Landau damping rates predicted for Maxwellian distributions are plotted from the mid-plane ($x = 0.01$ m) to the wall ($x = 0$ m). (Experiment L.)

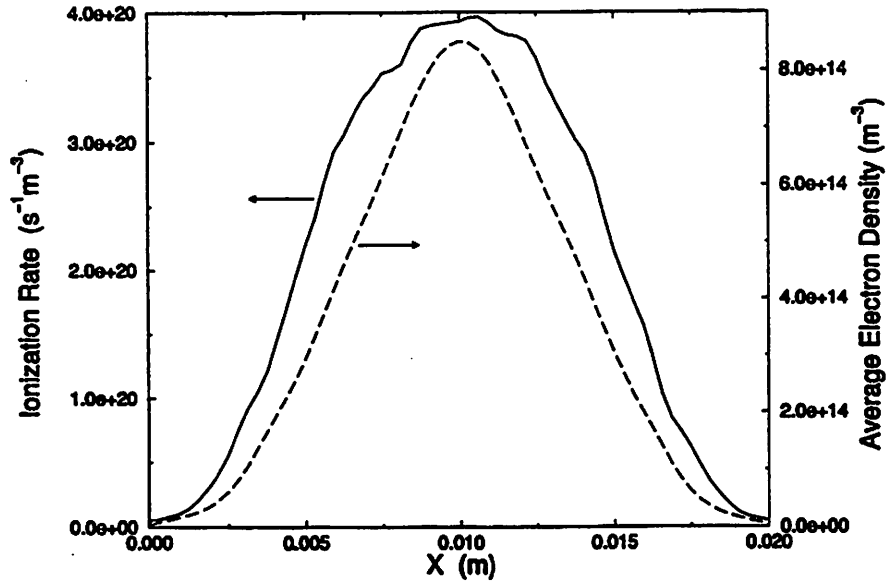


Figure 22. The time averaged ionization rate and electron density for experiment H ($p_{\text{argon}} = 2$ mTorr).

perpendicular to the walls is

$$\begin{aligned}
 (i\omega - \nu_m)m_e \hat{J}_1(x) &\equiv -(i\omega - \nu_m)m_e |e| n_{e0} f(x) v_{e1}(x) \\
 &= e^2 n_{e0} f(x) \frac{\partial \Phi_1(x)}{\partial x} + k_B T_{e0} \epsilon_0 \left(\frac{\partial^2 \Phi_1(x)}{\partial x^2} \right) \frac{\partial_x f(x)}{f(x)} \\
 &\quad - 3k_B T_{e0} \epsilon_0 \left(\frac{\partial^3 \Phi_1(x)}{\partial x^3} \right) \quad (19)
 \end{aligned}$$

where T_{e0} is derived from $3k_B T_{e0}/2 = \langle m_e v_e^2/2 \rangle$. Setting $\hat{J}_1(x=0)$ equal to zero locates the normal modes of the system.

Using these equations, we can solve numerically (as in [2]) for the location of the series resonance by computing the discharge gap impedance (equal to $e\Phi_1$ divided by the

displacement current, at the wall), and for the eigenmode structure and electron heating profiles associated with these modes. Results from this calculation are presented in section 4.

3.3. Stability

A main question is: how does the plasma adjust its density and sheath width in order to achieve resonance with the applied signal? Here we present a qualitative explanation for the stability and self-tuning as observed in these resonant discharges. To start our discussion we point out that in all simulations (to be presented in section 4), the applied voltage lagged the discharge current by between 10° and 25° in the steady-state. We also find that the

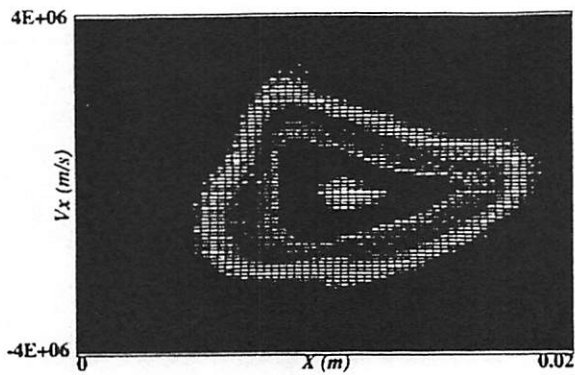


Figure 23. Snapshot of the electron distribution function, $f_e(x, v_x, t = 0)$, for experiment H. f_e is peaked at the centre and decreases to zero at the edges.

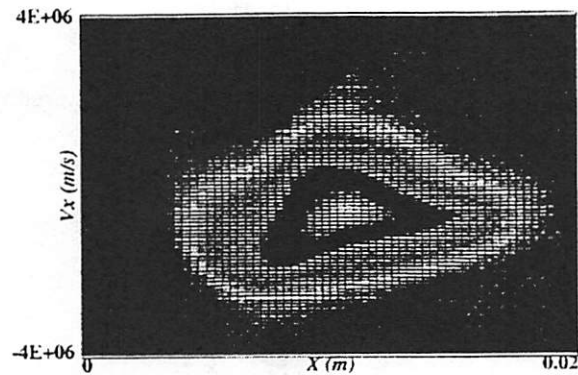


Figure 24. Snapshot of the electron distribution function, $f_e(x, v_x, t = T/8)$, for experiment H. T is the period of the applied signal.

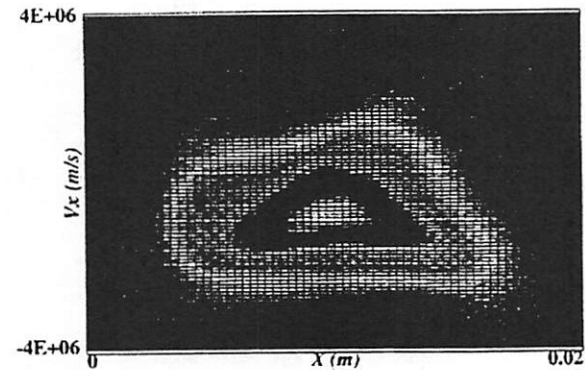


Figure 25. Snapshot of the electron distribution function, $f_e(x, v_x, t = T/4)$, for experiment H.

driving frequencies are very close to the series resonance as will also be shown in section 4. Examination of the homogeneous model impedance ((2), section 3.1) and the inhomogeneous fluid calculations described in section 3.2 indicates that the driving frequency must then be near but slightly less than the series resonance. With this point established we can quickly explain the stability of these discharges.

To proceed we make the further argument that the ion density profile (and also the electron profile under the assumption of quasi-neutrality) can be described by

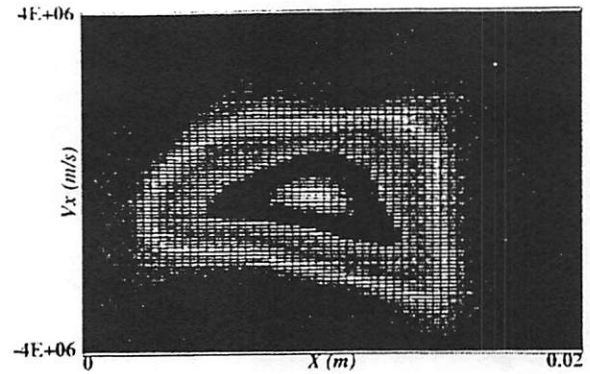


Figure 26. Snapshot of the electron distribution function, $f_e(x, v_x, t = 3T/8)$, for experiment H.

ambipolar diffusion for $\lambda_i \ll L$, where L is the width of the system and λ_i is the mean free path of the ions for ion-atom collisions, or at lower pressures by a variable-mobility model or a Langmuir solution [20]. In each case the normalized density profile, $n(x)/n_{mid}$, is given as a function of only $n_{neutral}$, T_e and T_i . T_i can be approximated by the neutral temperature and T_e is determined by $n_{neutral}$ and discharge length as a result of particle conservation [20]. The result we are after is that the steady-state normalized density profile, $n(x)/n_{mid}$, is independent of the power absorbed by the plasma. This means, for a discharge sustained by a fixed voltage source in which $P_{abs} \propto \text{Re}(Z^{-1})$ (see figure 3), that an increase (decrease), due to fluctuations, in absorbed power will bring an increase (decrease) in n_{mid} and, by equation (5), a proportional increase (decrease) in ω_{sr} (since the geometric factor $\sqrt{2\bar{s}}/L$ remains constant). Because we have established (through measurement of the I - V phase angle) that these discharges are being operated just below the series resonance (see figure 3), the increase (decrease) in ω_{sr} is followed by a decrease (increase) in the power dissipated in the plasma (since the resonance has moved further from the drive frequency) which produces a corrective decrease (increase) in n_{mid} . The result is a discharge in stable equilibrium whose density is determined by the driving frequency and T_e (where T_e is determined by the neutral gas pressure, size and shape of the system [20]). If we had chosen to drive the discharge with a fixed amplitude current signal, then the discharge would be stable at frequencies just above the resonance since $P_{abs} \propto \text{Re}(Z)$.

It should be mentioned that these discharges are also stable to high-frequency fluctuations. The result for ω_{sr} in the uniform density, thermal, matrix sheath model of Cooperberg [1] is

$$\omega_{sr} = \omega_{pe} \sqrt{\frac{2\bar{s}}{2\bar{s} + d}} \left(1 + \sqrt{\frac{3\lambda_{De}^2}{2\bar{s}d}} \right) \equiv \omega_{sr} \quad (20)$$

where \bar{s} represents the sheath width and can be taken to be a linear function of λ_{De} , which shows that an increase (decrease) in T_e leads to an increase (decrease) in ω_{sr} as before and consequently a stabilizing decrease (increase) in T_e .

Table 1. Varying ω_{rf} , fixed neutral density. Parameters for computer experiments A–G. v_m (Hz) $\approx 10^7 T_e$ (eV). V lags I by less than 25° in cases A–G. $\lambda_{ion\ mid}$ (cm) $\approx 1/330 p_{gas}$ (Torr) [20], $k_y = 0$, $L_x = 2$ cm for experiments A–G. n_e , f_{pe} and V_{mid} represent peak time averaged values. Applies to figures 4–8.

Experiment	f_{rf} (MHz)	P_{argon} (mTorr)	V_{source} (V)	n_e (cm $^{-3}$)	f_{pe} (MHz)	V_{mid} (V)	T_e (V)	P (mW cm $^{-2}$)	Q
A	110	10.0	2.5	7.2×10^8	241	26	3.4	1.9	7.5
B	120	10.0	2.5	1.0×10^9	284	27	3.4	2.6	7.9
C	140	10.0	2.5	1.7×10^9	370	27	2.9	3.6	8.9
D	200	10.0	2.5	6.2×10^9	706	25	2.3	11	13
E	300	10.0	3	1.36×10^{10}	1050	32	2.8	35	16
F	400	10.0	3	4.0×10^{10}	1800	38	2.8	103	13
G	470	10.0	3	7.2×10^{10}	2420	39	3.0	180	14

Table 2. Varying neutral density, fixed ω_{rf} . Parameters for experiments H–L. $\lambda_{ion\ mid}$ (cm) $\approx 1/330 p_{gas}$ (Torr) [20], $k_y = 0$. n_e , f_{pe} and V_{mid} represent peak time averaged values. ν_m and λ_{me} are the electron momentum collision frequency and mean free path for electron–neutral collisions respectively.

Exp.	f_{rf} (MHz)	P_{argon} (mTorr)	V_{source} (V)	n_e (cm $^{-3}$)	f_{pe} (MHz)	V_{mid} (V)	ν_m (MHz)	λ_{me} (cm)	T_e (eV)	P (mW cm $^{-2}$)	Q
H	140	2.00	3.4	8.2×10^8	256	59	13	14	7.1	7.0	31.5
I	140	10.0	2.5	1.7×10^9	370	27	30	3.8	2.9	3.44	16.3
J	140	100	3.8	3.0×10^9	490	17.4	260	0.41	2.5	3.9	3.24
K	140	300	6.0	3.7×10^9	545	16.6	780	0.14	2.5	5.35	1.37
L	400 ^a	2	4.6	2.0×10^{10}	1270	66	13	13	6.8	98.9	40.9

^a Experiment L run at higher frequency and low pressure to assist in analysis of collisionless electron heating (section 5).

4. Simulation results

In this section we show the results for several computer experiments over varying frequencies and gas pressures in which plasma discharges are resonantly sustained. In order to ensure that the discharges are indeed at or near resonance, we use the theoretical analysis in section 3 which predicts that (for low pressures) the plasma is in a resonant state when a minimum voltage, V_{min} , is applied. In order to achieve this condition through simulation, a discharge is first built up at $V_{rf} > V_{min}$. The amplitude of the applied voltage signal is then incrementally lowered until the plasma extinguishes in order to find the minimum operating voltage. Error associated with the finite decrement can be estimated to lead measured values of V_{min} no more than 5% above the actual values.

4.1. Fixed argon pressure, varying frequency

A series of computer experiments at varying ω_{rf} and fixed P_{argon} are described in table 1 and figures 4–8. Some of the notable features common to each of these discharges are summarized here. Applied V lags I by less than 25° so the impedance seen by the external circuit is essentially resistive. Also, $\nu_m \approx 10^7 T_e$ (eV) Hz $\ll \omega_{rf}$, where T_e is average kinetic energy of electrons. A mid-potential $V_{mid} \sim 10V_{source} > V_{ioniz.}$ (≈ 15 eV) is observed with peak time-dependent potentials near the plasma boundaries $V_{peak} \lesssim 2V_{mid}$ (figure 8). Figure 8 also shows the eigenfunction, $\Phi(x)$, predicted by the fluid theory of section 3.2. A partial reason for the differences between the measured and theoretical profiles is the inadequacy of the

fluid model to capture kinetic effects such as collisionless damping as will be discussed in section 5. The scalings $n \propto \omega^3$ (figure 6), $s \propto 1/\omega$ (figure 7) are followed. An extrapolation to $f_{rf} = 2450$ MHz produces $n_{epeak} \approx 10^{13}$ cm $^{-3}$. The sheath widths are in the range of $10\lambda_{De}$ to $20\lambda_{De}$ where λ_{De} is measured at the mid-plane. The Debye length near the plasma edge is larger due to a decreased plasma density. This characteristic allows for field penetration into the bulk plasma which cannot be neglected.

4.2. Fixed frequency, varying argon pressure

Another series of simulations was conducted in which P_{argon} was varied with a fixed ω_{rf} . The data are shown in table 2. The discharge gap impedance and the mechanism of electron heating are studied in these simulations. A transition is seen between the low- ($\lesssim 100$ mTorr) and high-pressure regimes. Figures 9 and 10 of the time averaged $J_{electron} \cdot E$ illustrate this transition. The ‘theory’ curve in these plots is generated by modifying the fluid calculations of section 3.2 to include an electron momentum transfer collision term. At lower pressures, the electron heating profiles show a wavelike structure as a result of the strong resonant surface wave fields; the low-pressure heating cannot be modelled as ohmic. At higher pressures, the plasma is well modelled by the collisional fluid equations and the heating is primarily ohmic.

Figures 11–14 show the amplitude of the gap admittance and phase of the gap impedance for experiments I and K. The admittance is measured by measuring the response to an applied, low-amplitude ($V_{probe} \ll V_{rf}$),

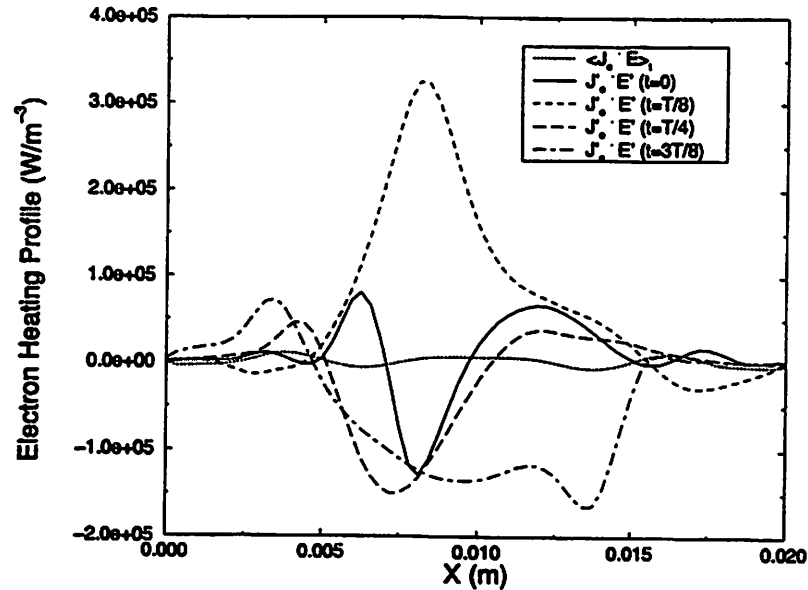


Figure 27. Snapshots of $J_e \cdot E'$ (experiment H). The prime indicates that the average value has been subtracted from the signal to facilitate analysis.

probe signal. The main (series) resonance and alternating symmetric and asymmetric secondary resonances are observed [2] as alternating maxima and minima in the admittance plots. The theoretical curves are derived from the fluid theory described previously. We could also use equation (2) but that would require an accurate determination of the sheath width which is difficult. The series resonance is observed to be very closely matched to the source frequency. The quality (as derived from the full width at half maximum of the impedance spectrum) clearly degrades with increasing neutral pressure.

The additional secondary or Tonks–Dattner resonances in the admittance (figures 11 and 13), which are located at frequencies above ω_{sr} and below the peak ω_{pe} , may also be used to sustain a plasma. Experimental work by Messiaen and Vandeplass [22] shows that the secondary resonances in a dielectric lined plasma cylinder can be used to sustain a plasma.

5. Collisionless electron heating

5.1. Description and discussion

The density and sheath scaling laws predicted by Godyak [6,7] are in good agreement with our simulation, and the measured wave eigenstructures and gap impedance are in reasonable agreement with the inhomogeneous fluid theory discussed in section 3.2. However, the actual mechanism for electron heating (ohmic plus stochastic in the (in)homogeneous model, and ohmic in the inhomogeneous fluid model) is not sufficient to describe the results observed in simulations.

Our computer experiments at low argon gas pressures show spatial oscillations in the electron heating, $J_e \cdot E$, and regions of electron cooling (figure 9) which we interpret as resulting from particle–wave interactions which produce a hot-electron population (figures 5 and 15). The adiabatic,

inhomogeneous fluid model and the (in)homogeneous model are both inadequate for predicting the electron heating profiles at low pressures which have been observed here. This is because wave–particle heating is a kinetic effect.

Electron heating profiles generated from PIC–MCC modelling are reported by other authors [13,16,23]. In these works, the conventional (high voltage, low frequency, moderate neutral pressures $\gtrsim 50$ mTorr) capacitively coupled discharges have been studied. The oscillation of $\langle J_e \cdot E \rangle_t$ at the edges, shown in figure 9 and also in figures 19 and 29, is not observed in these earlier works.

There are two commonly cited mechanisms for electron heating in parallel-plate discharges. The first is ohmic heating which can be derived from a fluid model with a collision term, or by assuming a plasma permittivity of the form given in (3) in the cold (in)homogeneous model. From these models, only positive time averaged electron heating is predicted.

The second heating mechanism is stochastic heating [20,24,25], which is often described as electron heating resulting from collisions with a moving sheath potential wall. In the early work [24], a slowly moving sheath (compared to v_{Te}) with $\omega \ll \omega_{pe}$ was considered and an effective collision frequency was derived. This effect was incorporated into the (in)homogeneous model by adding a stochastic resistance term into an expression for the discharge gap impedance [7]. In more recent work, solutions for fast- and slow-moving sheaths (compared to $v_{thermal}$) have been found [25]. In the work of Wood *et al* [25] the model of Lieberman and Lichtenberg [20] is used to describe the plasma in which the sheaths are considered to be electron free so that the sheath/plasma boundary is sharp. The case of $v_{sheath} \sim v_{Te}$ is not directly handled. Also, in the fast-sheath limit, the effect of electron cooling against the collapsing sheath is not modelled. Such approximations were necessary to obtain analytic results.

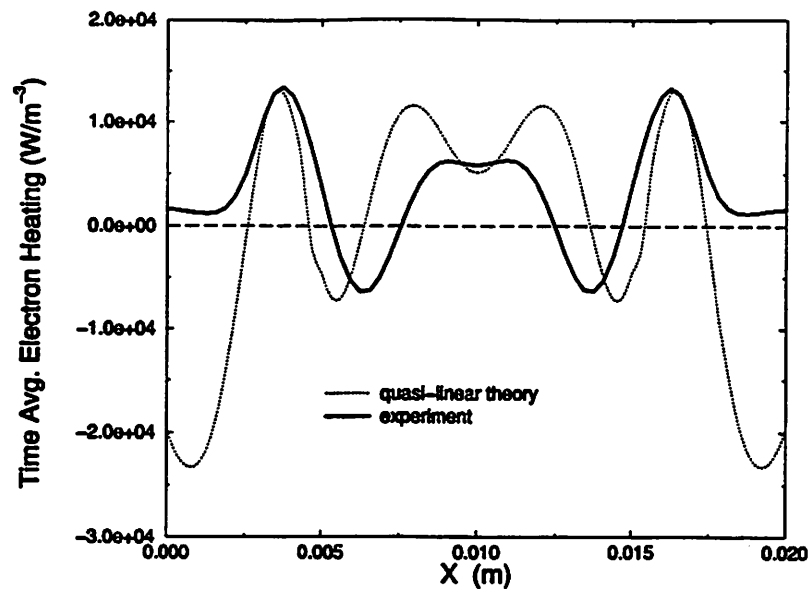


Figure 28. The electron heating profile, $J_e \cdot E(x)$, measured in experiment H is compared to a simplified expression for quasi-linear heating derived in section 5.2.

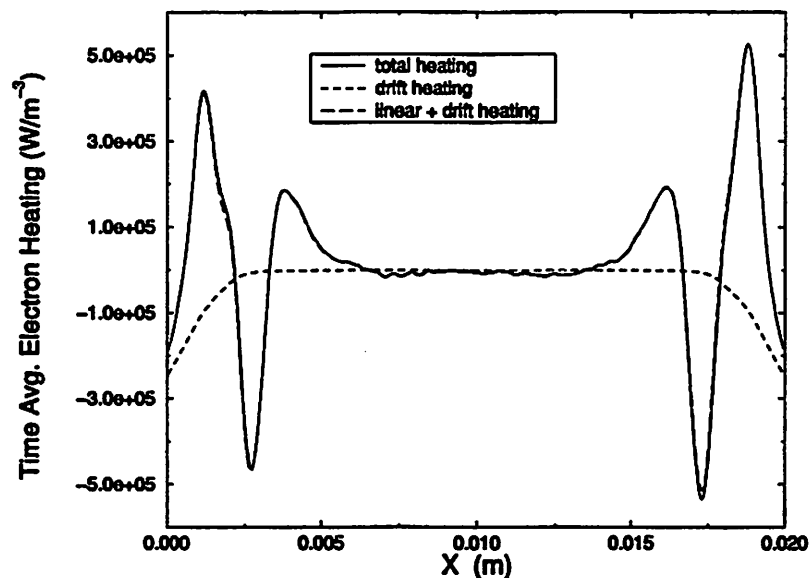


Figure 29. Total, 'linear' and drift electron heating for experiment L computed as in figure 19 ($n_{e,peak} = 2 \times 10^{10} \text{ cm}^{-3}$, $P_{argon} = 2 \text{ mTorr}$). The slight asymmetry about $x = 0$ is likely due to an insufficient averaging interval.

In this study we find that the series resonant discharge sustains a longitudinal wave which is bound by the overdense central plasma region and the metal boundary (for wave structures see figures 8 and 17). This resonance can also be thought of as the cutoff (for propagation in a direction parallel to the metal boundaries) of a propagating surface (sheath) wave [1,2]. We think of these resonant discharges as supporting standing surface waves in contrast to the (in)homogeneous model in which the electron density at the edges exhibits a sharply defined jump from zero to a value prescribed by the local ion density, and the electric field similarly drops sharply from a large sheath value to a negligible bulk value. These waves appear partly because the equilibrium sheath widths in our computer experiments

are short, on the order of undriven sheath widths, and the decay length of electron density and fields is not negligible. The perturbed electron density is shown in figure 18 for a representative discharge. The wavelength of the standing wave decreases towards the walls and the phase velocity of the standing wave (in either direction), which is associated with the sheath velocity of the (in)homogeneous model, will be $\sim v_{thermal}$ over some region. These observations suggest that significant collisionless Landau damping may occur in which particles may resonantly interact with portions of the standing wave where the resonance condition ($\omega - k_x v_x = 0$) is satisfied. Figures 20 and 21 show the local wavenumber, k_x (in the long-wavelength limit), and the associated linear Landau damping rates predicted for

Maxwellian distributions. Since the wave amplitudes are large (leading to large bounce frequencies) and the electron distributions are observed to be highly non-Maxwellian, the Landau damping (here considered linear, though present in a nonlinear regime) is only meant to give a crude estimate of the damping mechanism and rate. Since, in the case of the series resonant discharges studied here, we have $v_{\text{phase}} \approx 2\pi\omega/\bar{s} \sim v_{\text{thermal}}$ (\bar{s} is average sheath width), and low sheath voltages and sheath widths are obtained (as compared to the non-resonant discharge), we can think of heating in a wave fashion rather than as a discrete moving sheath wall with an electron free sheath which results from larger applied signals and larger sheath width oscillations. Although resonant electrons only see the standing wave for roughly one wave period (half in each direction), the large wave amplitude allows for significant perturbation of the steady-state distribution.

The benefit of the wave approach is that it captures the significant effects of electron cooling in a self-consistent manner. In the stochastic model, electrons can be cooled locally during sheath collapse by approximating the sheath as a retreating potential barrier. In the standing surface wave model, the electrons are accelerated and decelerated by the surface wave resulting in a strongly perturbed EEPF (figures 23–26). The perturbations at velocities toward the walls undergo reflection and then interact again with the surface wave fields. Inverse Landau damping can then occur. This inverse damping may be responsible for the time average electron cooling regions observed in simulation at low pressure.

The electron bunches reflected by the sheath travel towards the plasma bulk at approximately v_{Te} (since the Landau damping approaching the sheath had been strongest at $\sim v_{Te}$). These bunches can lead to ‘anomalous’ currents which fall out of phase with the surface wave fields since the wave phase velocity increases as the plasma density increases toward the bulk. This description is similar to that given by Godyak and Piejak [26] in explaining their measurements of current density and electric field in an inductively coupled plasma (ICP). Godyak and Piejak measured regions along the direction of electromagnetic field propagation where the electric field and current density become approximately 180° out of phase at low pressures (electron mean free path less than skin depth). They attribute this to an ‘anomalous skin effect’ where currents generated near the coil are translated into the plasma by electron thermal motion. The capacitive system is more complicated because density perturbations accompany the current perturbations and self-consistently determine the field structure. Also the EEPF can be severely non-Maxwellian and higher harmonics are also not negligible.

The downside of the standing surface wave model is the difficulty it presents in developing an analytic treatment which accurately captures this collisionless damping. Also, the internal fields are large enough to draw into question a linear treatment of the problem.

A purely analytic model which captures the electron heating (and steady-state EEPFs) is beyond the scope of this paper. Instead we take advantage of simulation results for the cycle averaged quantities, $E(x, t)$ and $F(x, v, t)$,

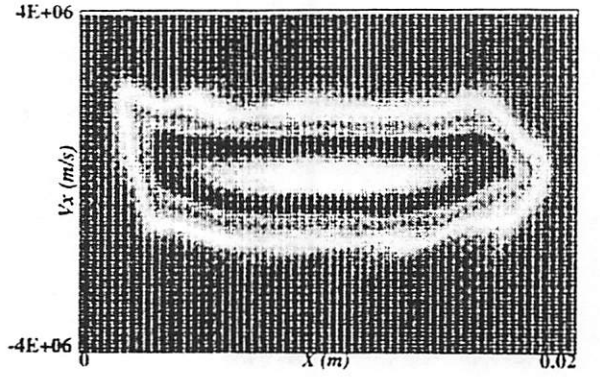


Figure 30. Snapshot of the electron distribution function, $f_e(x, v_x, t)$, for experiment L. f_e is peaked at the centre and decreases to zero at the edges.

in drawing some conclusions about what approximations might be made in developing such an analytic model.

5.2. Approximate theory for heating and cooling

First, we would like to verify that the electron heating profiles can be derived from a Boltzmann model which includes Landau damping. To do so we start from Boltzmann’s equation,

$$\frac{\partial F(\mathbf{r}, \mathbf{v}, t)}{\partial t} + \mathbf{v} \cdot \frac{\partial F(\mathbf{r}, \mathbf{v}, t)}{\partial \mathbf{r}} + \frac{e}{m} E(\mathbf{r}, t) \cdot \frac{\partial F(\mathbf{r}, \mathbf{v}, t)}{\partial \mathbf{v}} = S(F) \quad (21)$$

where $S(F)$ represents all collisions. We write the total distribution and electric field (understood to be a vector in the \hat{x} direction) as sums of steady-state and time varying parts,

$$F = \langle F \rangle_\tau + \hat{f} \quad E = \langle E \rangle_\tau + \hat{e}. \quad (22)$$

The steady-state equation is then

$$\frac{\partial \langle F(\mathbf{r}, \mathbf{v}, t) \rangle_\tau}{\partial t} + \mathbf{v} \cdot \frac{\partial \langle F(\mathbf{r}, \mathbf{v}, t) \rangle_\tau}{\partial \mathbf{r}} + \frac{e}{m} \langle E(\mathbf{r}, t) \rangle_\tau \cdot \frac{\partial \langle F(\mathbf{r}, \mathbf{v}, t) \rangle_\tau}{\partial \mathbf{v}} + \frac{e}{m} \left\langle \hat{e}(\mathbf{r}, t) \cdot \frac{\partial \hat{f}(\mathbf{r}, \mathbf{v}, t)}{\partial \mathbf{v}} \right\rangle_\tau = \langle S(F) \rangle_\tau. \quad (23)$$

Solving for the perturbation \hat{f} , with the assumption of linearity ($\hat{f} \ll \langle F \rangle_\tau$) and further assuming that the electron mean free path is longer than the scale length of perturbation variation [27] (table 2 shows that, at low pressures, the mean free path is indeed longer than the system), we have

$$\frac{\partial \hat{f}(\mathbf{r}, \mathbf{v}, t)}{\partial t} + \mathbf{v} \cdot \frac{\partial \hat{f}(\mathbf{r}, \mathbf{v}, t)}{\partial \mathbf{r}} + \frac{e}{m} \hat{e}(\mathbf{r}, t) \cdot \frac{\partial \langle F(\mathbf{r}, \mathbf{v}, t) \rangle_\tau}{\partial \mathbf{v}} + \frac{e}{m} \langle E(\mathbf{r}, t) \rangle_\tau \cdot \frac{\partial \hat{f}(\mathbf{r}, \mathbf{v}, t)}{\partial \mathbf{v}} = 0. \quad (24)$$

If we drop the $\langle E \rangle_\tau \partial \hat{f} / \partial v$ term, we can solve for \hat{f} in terms of \hat{e} and $\langle F \rangle_\tau$ and arrive at a typical expression for

the quasi-linear term in equation (23),

$$\begin{aligned} \text{Q.L. term} &\equiv \frac{e}{m} \left\langle \hat{e}(\mathbf{r}, t) \cdot \frac{\partial \hat{f}(\mathbf{r}, v, t)}{\partial v} \right\rangle_{\mathbf{r}} \\ &= -\frac{e^2}{m^2} \frac{1}{4} \left\langle \left(\hat{e}(x, t) e^{i\omega t} + \text{cc} \right) \cdot \partial_v \left(\int_{-\infty}^{\infty} dk \right. \right. \\ &\quad \left. \left. \times e^{ikx} \frac{\int_{-\infty}^{\infty} (dx'/2\pi) e^{-ikx'} e(x, t) (F(x, v, t))_{\mathbf{r}}}{i(\omega - v_x k)} + \text{cc} \right) \right\rangle_{\mathbf{r}} \end{aligned} \quad (25)$$

where we have reduced the equation to 1D in space. As a first approximation one might assume $(F)_{\mathbf{r}} \propto n(\mathbf{r}) e^{-v^2/v_{Te}^2}$, so we may perform the velocity integration. We use the \hat{e} , $n(\mathbf{r})$ and v_{Te} determined by simulation. The result is a spatially resolved, collisionless electron heating term, which, when multiplied by $m_e v^2/2$ and integrated over velocity space to produce an electron heating term, does exhibit oscillations (regions of electron heating and cooling, figure 28). However, the agreement with actual heating profiles is poor. There are two reasons likely for the discrepancy. First is use of a Maxwellian electron distribution which is acceptable at high pressures (figure 16) but not in agreement with the measured distributions at low pressure (see figures 15 and 5). Second is the dropping of the $(E)_{\mathbf{r}} \partial \hat{f} / \partial v$, term in arriving at (25).

An alternative numerical approach, in which we use the \hat{e} and \hat{f} measured in simulation, allows us to solve for the quasi-linear heating term directly. Of course, the result is equivalent to the $J_e \cdot E$ measured from simulation. In order to determine whether an assumption of linearity can be made, we can construct \hat{e}_1 and \hat{f}_1 (where the subscript indicates the component oscillating at the applied frequency) from the simulation data and again compute the electron heating profile. Results of this calculation are shown in figures 19 and 29, which show that $J_e \cdot E$ profiles are well modelled by the linearized \hat{e} and \hat{f} . Further evidence that this resonant system remains in a linear regime comes from measurements of the harmonic signal strength of the electrostatic potential and electric field (see figures 17 and 18) which indicate a small contribution from the second harmonic. Signals at higher frequencies are negligible. An analytic approach could be derived from first principles with the linearized, inhomogeneous Boltzmann equation and Poisson's equation (given the steady-state quantities F and E). This step is not attempted here.

Convincing evidence that strong collisionless Landau damping is occurring is given in figures 23–27. (Note, data for only one half period is shown because the electron distribution function during the second half period is the same except for a reflection across the midplane in x). These figures show the time evolution of $F(x, v_x, t)$ and electron heating, during a half wave period. Here, the perturbation of $F(x, v_x, t)$ is clearly recognized as electron bunches or beams which are accelerated and retarded by the strong edge fields. At $t = 3T/8$ (figure 26, T is the wave period) the electron distribution function has two peaks (at $x = 0.0137$ m) and the fast-moving reflected electrons are cooled as shown in figure 27. The other regions of electron cooling are due to electron expansion into the

sheath regions. Not considered here are the possibility (for low bulk collisionality, i.e., low pressure and low density) of correlation effects associated with electron bunches, which may have multiple interactions with the edge fields. The frequency of bunches leaving the walls is equal to the applied frequency.

A further simulation, listed as experiment L in table 2, which has not been explicitly mentioned yet, was performed at a higher frequency and plasma density while keeping the same neutral pressure of 2 mTorr as experiment H. This simulation shows that complex edge heating persists at higher densities. The electron heating profile is given in figure 29 and a snapshot of $F(x, v_x, t)$ is shown in figure 30. Electron heating and cooling is again observed at the edges, and electron bunching is found in $F(x, v_x, t)$.

With this understanding of the dynamics of the electron heating in resonant discharges one might develop a non-local approach [28–31] in order to solve Boltzmann's equation in the hopes of obtaining an analytic model for $(F)_{\mathbf{r}}$. This is an essential quantity in determining plasma composition. Evidence of the non-local behaviour of the low-pressure resonant discharge is shown in figure 22 which shows the ionization rate in space to be more similar to the electron density profile than electron heating profiles. One might adapt the theory of Aliev *et al* [32, 33] for quasi-linear heating due to local resonances in a travelling surface wave discharge with a dielectric boundary. In the resonant discharges described in our work, the scale length of the steady-state fields and resonant fields are similar (on the order of the sheath thickness); hence, it is predicted that this will require modification to Aliev's theory in modelling the series resonant discharge. Another point of concern is the high degree of anisotropy (at low pressures) in $F(x, v_x, v_y, v_z, t)$ (bunching is only observed in the \hat{x} direction along the electric field) which is not treated in the cited works.

Before leaving our discussion of electron heating, we comment on the quality factors, Q , shown in table 2 (and table 1). The quality factor, calculated for each resonant discharge, is given by

$$Q = \frac{2\pi \text{ stored energy}}{T \text{ power dissipated}} = \frac{\omega}{\Delta\omega_{fwhm}}$$

where T is the wave period. The energy density stored in the resonant oscillation is taken to be

$$\begin{aligned} \text{stored energy} &= \int_0^T dt \int_{\text{volume}} dV \left(\frac{\epsilon_0}{2} (E(x, t) - \bar{E}(x))^2 \right. \\ &\quad \left. + \frac{m_e v^2}{2} (f(x, v, t) - \bar{f}(x, v))^2 \right) \end{aligned} \quad (26)$$

where bars indicate time averaged quantities. The power loss is equal to the power supplied in the steady-state and is computed from the time averaged VI across the discharge gap.

We find, as can be expected, that Q approaches the value ω/v_m for increasing pressures, and is significantly lower than ω/v_m for lower pressures due to the enhanced role of collisionless damping. Similar trends are seen in transitions to stochastic heating for non-resonant discharges [34].

6. Conclusions

Parallel-plate discharges have been sustained at the series resonance. A nearly pure resistive load is seen by the drive circuit. Power can then be supplied with low applied voltages (2 and 3 volts) to sustain argon discharges with sheath potentials $\sim 10T_e$. Peak time-dependent internal voltages exceed this value. Densities up to $\sim 1 \times 10^{11} \text{ cm}^3$ have been simulated (higher densities requiring extensive computation time), with density increasing as the cube of the drive frequency. Results are compared with the predictions of various models with some success. Discharge stability has been analysed.

Heating profiles ($(J_e \cdot E)_i(x)$) at low pressures are distinct from other discharges, exhibiting regions of heating and cooling at the plasma edge. Heating mechanisms have been analysed. EEPFs have been measured showing the presence of a hot-electron tail at low pressures.

Acknowledgments

The authors would like to thank V Vahedi and J Verboncoeur for helpful discussions. Professor M A Lieberman's critical review of this material is also gratefully acknowledged. This work was supported in large part by ONR-ASSERT N100014-93-1-1389.

References

- [1] Cooperberg D J 1997 Electron surface waves in a plasma slab with uniform ion density *Phys. Plasmas* at press
- [2] Cooperberg D J 1997 Electron surface waves in a nonuniform plasma slab *Phys. Plasmas* submitted
- [3] Taillet J 1969 Resonance-sustained radio frequency discharges *Am. J. Phys.* **37** 423
- [4] Vandenplas P E 1968 *Electron Waves and Resonances in Bounded Plasmas* (New York: Interscience)
- [5] Crawford F W and Kino G S 1963 *C. R. Acad. Sci., Paris* **256** 1939
- [6] Godyak V A 1986 *Sov. RF Discharge Res.* (Falls Church, VA: Delphic)
- [7] Godyak V A 1976 Steady-state low-pressure rf discharges *Sov. J. Plasma Phys.* **12** 78
- [8] Godyak V A and Popov O A 1977 Double-valued behaviour of the parameters of an rf discharge as functions of the burning voltage *Sov. J. Plasma Phys.* **3** 238
- [9] Godyak V A and Popov O A 1979 Experimental study of resonant rf discharges *Sov. J. Plasma Phys.* **5** 227
- [10] Godyak V A, Popov O A and Ganna A Kh 1976 Effective electron collision frequency in rf discharges *Sov. J. Plasma Phys.* **2** 560
- [11] Godyak V A and Ganna A Kh 1980 Collisional rf discharge *Sov. J. Plasma Phys.* **6** 372
- [12] Birdsall C K 1991 Particle-in-cell charged-particle simulations, plus Monte Carlo collisions with neutral atoms, PIC-MCC *IEEE Trans. Plasma Sci.* **PS-19** 65
- [13] Vahedi V, Birdsall C K, Lieberman M A, DiPeso G and Rognlien T D 1993 Capacitive rf discharges modelled by particle-in-cell Monte Carlo simulation. ii. Comparisons with laboratory measurements of electron energy distribution functions *Plasma Sources Sci. Technol.* **2** 273
- [14] Godyak V A, Piejak R B and Alexandrovich B M 1992 Measurements of electron energy distribution in low-pressure rf discharges *Plasma Sources Sci. Technol.* **1** 36
- [15] Vahedi V, DiPeso G, Rognlien T D and Birdsall C K 1993 Verification of frequency scaling laws for capacitive rf discharges using two-dimensional simulations *Phys. Fluids B* **5** 2719
- [16] Surendra M and Graves D B 1991 Particle simulations of radio-frequency glow discharges *IEEE Trans. Plasma Sci.* **PS-19** 144
- [17] Verboncoeur J P, Alves M V, Vahedi V and Birdsall C K 1993 Simultaneous potential and circuit solution for 1d bounded plasma particle simulation codes *J. Comput. Phys.* **104** 321
- [18] Vahedi V and Surendra M 1995 A Monte Carlo collision model for the particle-in-cell method: applications to argon and oxygen discharges *Comput. Phys. Commun.* **87** 179
- [19] Birdsall C K and Langdon A B 1991 *Plasma Physics Via Computer Simulation* (Bristol: Hilger)
- [20] Lieberman M A and Lichtenberg A J 1994 *Principles of Plasma Discharges and Materials Processing* (New York: Wiley)
- [21] Parker J V, Nickel J C and Gould R W 1964 Resonance oscillations in a hot nonuniform plasma *Phys. Fluids* **7** 1489
- [22] Messiaen A M and Vandenplas P E 1967 Nonlinear resonance effect at high power in a cylindrical plasma *Phys. Lett.* **25A** 339
- [23] Nitschke T E and Graves D B 1994 A comparison of particle in cell and fluid model simulations of low-pressure radio frequency discharges *J. Appl. Phys.* **76** 5646
- [24] Godyak V A 1972 Statistical heating of electrons at an oscillating plasma boundary *Sov. Phys.-Tech. Phys.* **16** 1073
- [25] Wood B P, Lieberman M L and Lichtenberg A J 1995 Stochastic electron heating in a capacitive rf discharge with non-Maxwellian and time-varying distributions *IEEE Trans. Plasma Sci.* **PS-23** 89
- [26] Godyak V A and Piejak R B 1982 Electromagnetic field structure in a weakly collisional inductively coupled plasma *J. Appl. Phys.* **82** 5944
- [27] Aliev Yu M, Maximov A V, Bychenkov V Yu and Schlüter H 1992 High energy electron generation in surface-wave-produced plasmas *Plasma Sources Sci. Technol.* **1** 126
- [28] Bernstein I B and Holstein T 1954 Electron energy distributions in stationary discharges *Phys. Rev.* **9** 1475
- [29] Tsendin L D 1974 Energy distribution of electrons in a weakly ionized current-carrying plasma with a transverse inhomogeneity *Sov. Phys.-JETP* **39** 805
- [30] Kaganovich I D and Tsendin L D 1992 Low-pressure rf discharge in the free-flight regime *IEEE Trans. Plasma Sci.* **20** 86
- [31] Kaganovich I D and Tsendin L D 1992 The space-time-averaging procedure and modeling of the rf discharge, part ii: model of collisional low-pressure rf discharge *IEEE Trans. Plasma Sci.* **PS-20** 66
- [32] Aliev Yu M 1993 Some aspects of nonlinear theory of ionizing surface plasma waves *Microwave Discharges: Fundamentals and Applications (NATO Advanced Study Institute, Series B: Physics 302)* (New York: Plenum) p 105
- [33] Aliev Yu M, Maximov A V, Kortshagen U, Schlüter H and Shivarova A 1995 Modeling of microwave discharges in the presence of plasma resonances *Phys. Rev. E* **51** 6091
- [34] Popov O A and Godyak V A 1985 Power dissipated in low-pressure radio-frequency discharge plasmas *J. Appl. Phys.* **57** 53

Surface wave sustained plasmas in a metal bound plasma slab

D J Cooperberg and C K Birdsall

Department of Electrical Engineering and Computer Science,
University of California at Berkeley, Berkeley, CA 94720, USA

Received 11 August 1997, in final form 8 December 1997

Abstract. Standing electron surface waves have been used to naturally sustain a plasma discharge. This work differs from previous studies of surface wave discharges in that, here, we focus on surface waves excited in a metal bound plasma slab which propagate along the plasma/sheath boundary and sustain a discharge. Our 'experimental' results are obtained from electromagnetic particle-in-cell simulations with Monte Carlo collisions of a 2d3v plasma. Results are analysed for discharges operating over a range of frequencies, neutral gas pressures and antenna design.

1. Introduction

In early work [1–7] on resonantly sustained plasmas, the region of plasma generation is generally confined in space due to the method of excitation (within some cavity or between electrodes) [8]. As an example, Fehsenfeld *et al* [7] demonstrated a variety of microwave discharges in which a plasma is sustained in a glass tube by inserting the tube into a microwave cavity which is driven at one of the cavity resonant frequencies. The enhanced cavity fields start the plasma discharge after which the amplitude of the fields adjusts due to the introduction of the plasma load. The dimensions of the microwave resonant cavities are limited by design criteria at a given operating frequency, and are of the order of a few centimetres. These cavities produce plasma volumes of the order of tens of cubic centimetres. This limit prompted Moisan *et al* to develop a device called a surfatron in which a plasma column is sustained by a travelling surface wave launched from one end [8]. The launcher surrounds a gas filled dielectric tube which contains the plasma radially, but the plasma is not confined axially since the length of the discharge is proportional to the input power. Reported operation occurs over a wide range of neutral gas pressures and electron densities. Devices operate from a few hundred kHz to ~10 GHz with density ranges $5 \times 10^8 \text{ cm}^{-3}$ to a few 10^{15} cm^{-3} , gas pressures from 10^{-5} Torr to a few times atmospheric, and radii from 0.5 mm to 10 cm. Since these devices are electrodeless and can produce discharges over large volumes, they have been utilized in materials processing, ion sources, laser excitation, elemental analysis and lighting.

In a more recent work [9] Moisan and Zakrzewski give a review of the basic theory and various experimental designs for plasma sources based on the propagation of electromagnetic surface waves. The surfatron was the first

of these plasma sources and has inspired much subsequent research in the field. There also has been much theoretical work done to understand better these plasmas, with efforts mainly focusing on characterizing radial and axial profiles of the fields and plasma properties. Some of the early authors include Zakrzewski *et al* [10, 11], Glaude *et al* [12], Ferreira [13, 14] and Aliev *et al* [15, 16]. Recently, a new mechanism of electron heating has also been described [17].

In addition to the travelling surface wave sustained cylindrical discharges developed by Moisan, there has been an effort to develop standing and planar surface wave sustained plasmas. Some motivation for this effort comes from a desire for plasma uniformity which can be of use in laser sources and materials processing applications. Rakem *et al* [18] make a comparison between a simple model and experiment [19] on a cylindrical standing surface wave plasma where the far end of the column is shorted with a metal sleeve. For discharge (column) lengths less than some limit, the density remains nearly constant along the column axis (with some fraction of modulation due to the standing wave). An argon ion laser was built based on this structure.

Nonaka [20] reports on new devices similar to the surfatron, but with various cross-sections of which a rectangular one is of particular interest. A large area (up to 0.73 m \times 1.72 m) plasma is produced. Later analysis [21] of this planar travelling surface wave source led to determination of the axial density gradient in diffusion and recombination dominated regimes and electrostatic mode structure. The axial density gradient, although still linear in the propagation dimension, is predicted to be much less than in the cylindrical case.

Other efforts have led to the development of planar standing surface wave sources. A planar microwave standing surface wave device, developed by Komachi and Kobayashi [22], consists of a dielectric wave guide

(18 cm \times 30 cm) bound by metal and plasma on either side with a vacuum gap between the dielectric and the plasma. Microwave energy is fed into the dielectric guide and the fringe fields couple to and sustain the plasma. In the directions aligned with the dielectric plane, the plasma density is modulated about a nearly constant value by the standing wave. In the perpendicular (to the dielectric) direction the measured electron density decays rapidly. A simple model was presented based on a homogeneous plasma.

Another source similar to that of Komachi and Kobayashi [22] is presented by Nagatsu *et al* [23]. A planar source is operated at the end of a cylindrical cavity in which a slotted waveguide antenna is used to couple microwave power into a quartz window which separates the plasma chamber from the slot antenna. A standing surface wave pattern is observed in the optical emission intensity of the plasma, and the eigenmodes of the system are computed by Ghanashev *et al* [24]. The field strength of the electromagnetic surface wave modes is observed to decay into the overdense plasma in approximate agreement with the plasma skin depth.

We may categorize the variety of plasma sources discussed so far as follows. First, there are 1d metal bounded plasma sources (such as the capacitively coupled RF discharge) which can be operated at the series resonance (cutoff for the main asymmetric planar surface wave). There are cylindrical and planar dielectric bounded sources operating from the RF to the microwave regime in which both travelling and standing surface waves, which propagate along the plasma edge, sustain the plasma. Lastly, there are microwave sustained discharges in which a dielectric bound plasma is sustained by the fields of a resonant structure such as a cavity [7], a slow-wave structure [25,26], a fast-leaky-wave structure [27] or a dielectric waveguide [22,24]. In these latter devices the plasma is only weakly coupled to the sustaining structure and the plasmas are separated by open space or by dielectric containing vessels from the microwave sources. In other words, the sustaining structures (microwave cavity, slow-wave structure, fast-leaky-wave source or dielectric waveguide) in each of these sources is only weakly affected by the presence of the plasma as described by Zakrzewski and Moisan [28]. Because the structure of the applied fields is largely independent of the plasma these devices do not take full advantage of the normal surface modes of the bound plasma where the plasma becomes nearly a pure resistive load. Resonant excitation of these modes produces large currents in the plasma for small applied fields.

Prior surface wave discharges were maintained in dielectric bound columns. The surface waves associated with metal bound plasmas, which have been analysed in previous work [29,30] have not been considered as a means for sustaining a discharge. It may have been believed that such waves would be shorted out by the presence of conducting walls close to the plasma. This is not the case, as demonstrated previously [29,30], because the existence of the plasma sheaths enables surface slow-wave propagation. This is in agreement with prior experimental work by Napoli and Swartz [31] where detection of low-frequency forward waves in a conducting cylinder filled

with an annular plasma and a central solid dielectric rod were explained by incorporating a sheath capacitance between the conductor and the plasma in a planar plasma-guide model.

In this work we demonstrate a new type of plasma source, in which standing surface waves in a metal bound plasma slab are resonantly excited by an applied signal. The fields from these standing surface waves are used to heat the electrons which sustain the plasma. The work is performed via particle-in-cell (PIC) simulation [32] of an argon plasma in which a Monte Carlo collision algorithm [33] is used to model collisions with neutrals. A set of computer experiments have been performed with varying neutral pressures, excitation frequencies and antenna designs in order to characterize this type of source. Comparisons can be made with the resonantly sustained RF discharge in which RF power is applied at the series resonance [5,34] which arises from the balancing of the capacitance of the sheaths with the inductance of the plasma bulk in a 1D electrostatic model. Plasma density profiles, field structure, electron heating profiles, steady-state plasma parameters and electron energy probability functions (EPPFs) will be presented. The proposed source has the projected benefit of producing low-voltage plasmas in a wide range of gas pressures and plasma densities. Also the planar, standing wave configuration easily scales to large areas. Both of these features are desirable for many materials processing applications.

This work further introduces PIC simulation to the study of surface wave produced plasmas (SWPs) and it is hoped that this technique will provide added insight into the characterization of these types of source. In section 2 we describe our model and show schematics of the two different reactor configurations studied. Section 3 describes the simulation techniques used to represent our model. The results of several computer experiments (simulations) are presented in section 4. Conclusions follow in section 5.

2. Model description

In this work, we study the 2d3v (i.e. two displacement and three velocity dimensions) metal bounded argon plasma slab, which is sustained by standing surface waves. We choose the propagation direction to be along \hat{y} , and the direction perpendicular to the slab to be \hat{x} . We will consider both the infinite (periodic in \hat{y} and bound by metal walls in \hat{x}) slab, and the double-bounded cavity in which the slab is bound by metal walls in both \hat{x} and \hat{y} . The surface waves are excited by varying arrays of current loops of infinitesimal thickness as shown in figures 1 and 2. These designs have been chosen to excite an asymmetric surface wave [29,30] in the doubly bound system (a symmetric wave was not driven because of geometric constraints), and a hybrid mode, in which both symmetric and asymmetric modes are present in the system, which is periodic in \hat{y} . These models are each scalable to larger areas. The antenna designs have been chosen primarily for the ease in which they could be incorporated into our simulation code, XPDP2 [35], and not on their realizability in laboratory experiments. This idealization should not diminish the

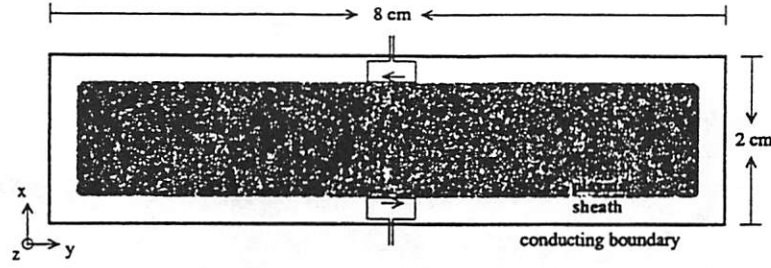


Figure 1. Schematic of 2D model bound in \hat{x} and \hat{y} for surface wave sustained discharge. Antenna current is given by $I_1 = -I_2 = \sin(\omega_{rf} t)$. Approximately to scale.

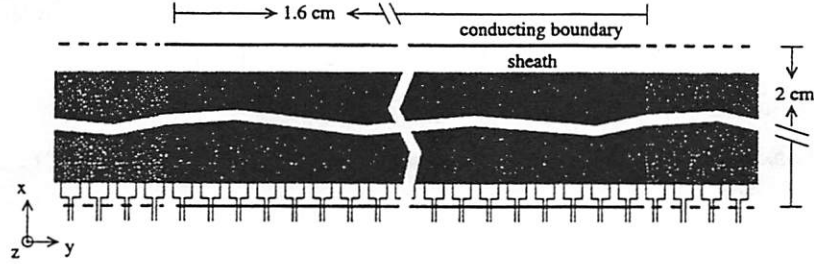


Figure 2. Schematic of 2D model bound in \hat{x} and \hat{y} for surface wave sustained discharge. Antenna current is given by $I_n = \cos(2\pi y_n/L_y) \sin(\omega_{rf} t)$.

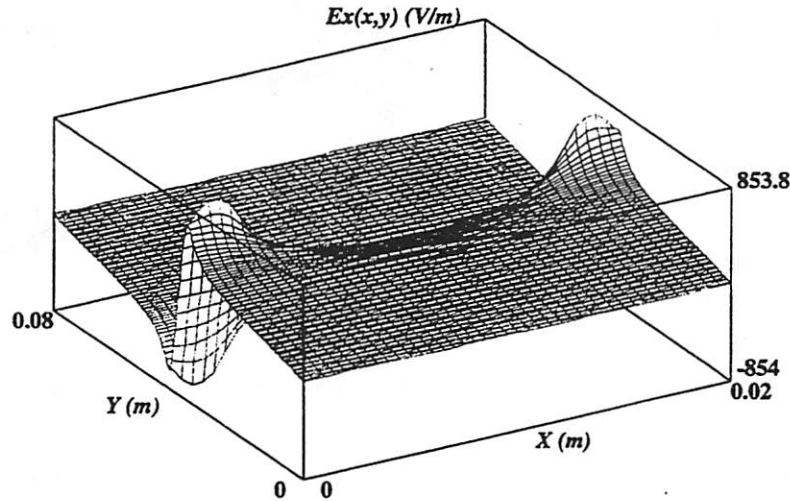


Figure 3. Peak antenna field, $E_x(x, y)$, for double-bounded system ($f_{rf} = 150$ MHz, $I_{source} = 700$ A m $^{-1}$).

results presented here. Several more realistic means of coupling might be envisioned in which the characteristics of the metal bound standing surface wave discharge are not greatly altered.

For all simulations, the slab thickness (\hat{x}) is 2 cm and a length of 1 m in the unresolved (\hat{z}) dimension is chosen for bookkeeping. The simulations bound in \hat{y} are 8 cm long in that dimension. The simulations which are infinite (and periodic) in \hat{y} have a period of 1.6 cm. Argon pressures vary from 2 to 100 mTorr. This range has been chosen because 1D simulations have shown that a heating mode transition takes place here [34] in which collisional or ohmic heating at higher pressures gives way to collisionless heating via wave-particle interactions at lower pressures. A modest frequency range of 1.5×10^8 – 3.0×10^8 Hz is used

to investigate plasma density, and discharge scaling with frequency. The standing, planar surface wave discharge described here is not thought to be restricted to this pressure and frequency range; however, simulation at higher argon pressures and frequencies requires increasing computation; runtimes on the workstations used for this work become prohibitive.

3. Simulation

As previously mentioned, we use the PIC code XPDP2 [35], with a Monte Carlo scheme [33] for modelling collisions with argon neutrals, for our study. This code has been heavily modified to allow modelling of the planar surface wave discharge. The main change has been the

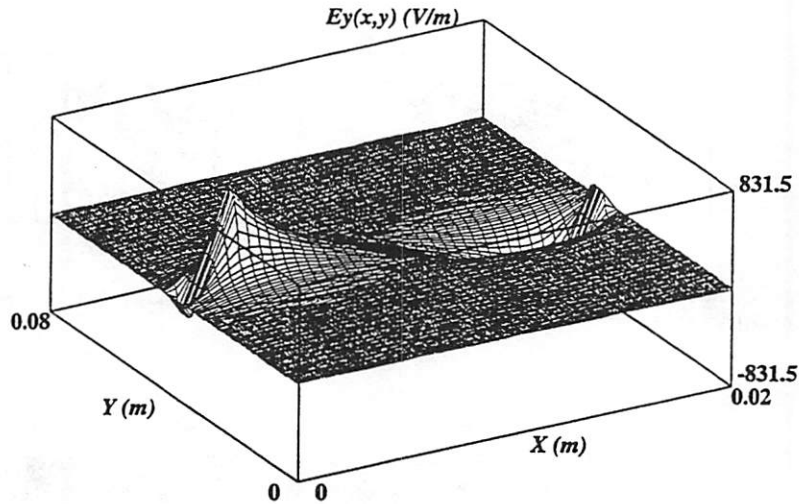


Figure 4. Peak antenna field, $E_y(x, y)$, for double-bounded system ($f_{rf} = 150$ MHz, $I_{source} = 700$ A m $^{-1}$).

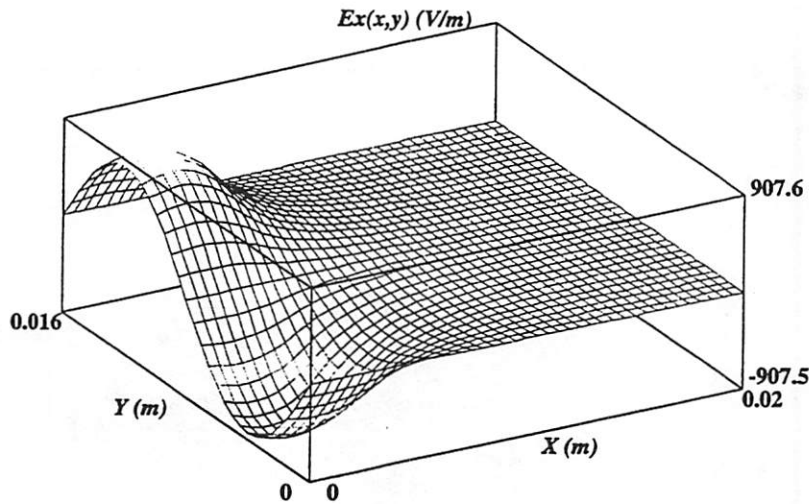


Figure 5. Peak antenna field, $E_x(x, y)$, for system bound in \hat{x} and periodic in \hat{y} ($f_{rf} = 200$ MHz, $I_{source} = 350$ A m $^{-1}$).

addition of an electromagnetic field solver and a charge conserving, particle current gathering routine [36] for both the periodic and bound models (in \hat{y}). The current gathering is done simultaneously with the particle advance in order to detect cell crossings and more accurately gather the particle current. The switch from an electrostatic code to an electromagnetic one was needed in order to self-consistently couple the antenna fields to the surface waves. We will see, however, that, since the surface waves are slow waves with the wavelengths much smaller than that of waves of the same frequency in vacuum, the wave fields present in the steady-state discharge are primarily electrostatic (irrotational) in nature and may be derived from Poisson's equation. However, at longer wavelengths in \hat{y} or at higher (microwave) frequencies not modelled here (due to computational constraints), the waves would require an electromagnetic description.

In order to improve computational performance, several additional modifications to XPDP2 were made. They include the subcycling of the electromagnetic field solver

with respect to the electron particle push and gather, and the subcycling of electrons with respect to the ion pushing/gathering [32]. This is useful because the field Courant condition requires that $\Delta x/(c\Delta t)$, $\Delta y/(c\Delta t) \lesssim 0.5$ while particle Courant merely requires $\Delta x/(v_{Te}\Delta t)$, $\Delta y/(v_{Te}\Delta t) \lesssim 0.5$ and, since we are examining a non-relativistic plasma, these conditions impose significantly different constraints on the time step for field and particle advance. Numerical instabilities, associated with subcycling the fields, were eliminated with damping schemes including the introduction of a small surface impedance on the walls and a lag averaging scheme [37] in the electric field advance. Divergence cleaning was also implemented to further reduce error whereby $\nabla \cdot \mathbf{E} = \rho/\epsilon_0$ is periodically enforced to correct numerical error in the field solver which relies on Faraday's law and Ampere's law to advance the fields in time without explicitly enforcing Coulomb's law.

The metal boundaries are taken to be nearly perfect conductors and to absorb incident particles. Secondary

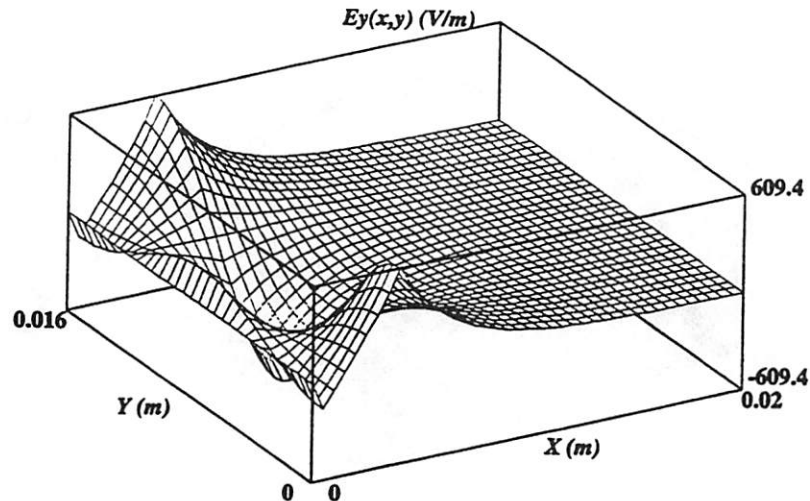


Figure 6. Peak antenna field, $E_y(x, y)$, for system bound in \hat{x} and periodic in \hat{y} ($f_H = 200$ MHz, $I_{source} = 350$ A m $^{-1}$).

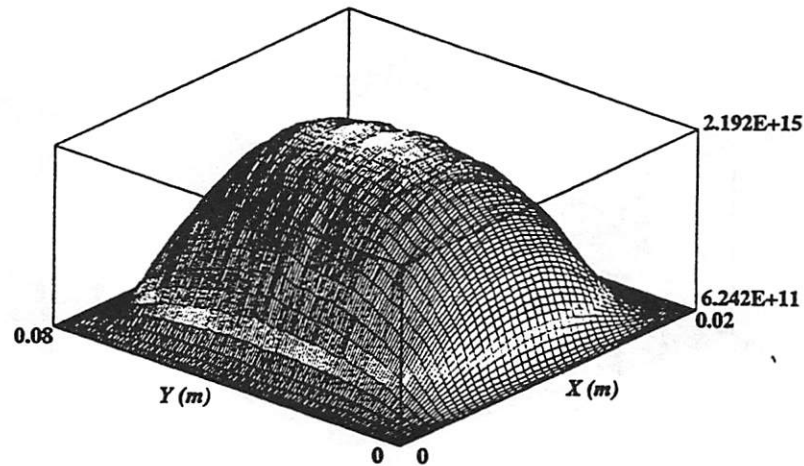


Figure 7. Average electron density, $n_e(x, y)$ (in m $^{-3}$), for double-bounded system.

emission is not implemented (which is acceptable for low plasma potentials, V_{plasma}) although the code is capable of secondary emission. In the periodic model, both particles and electromagnetic fields which exit one end are injected at the other end.

The following method is applied to produce the steady-state discharges. A uniform plasma is loaded at $t = 0$ between the conducting boundaries with a density chosen to be near the expected equilibrium value at the midplane of the final steady state. A fixed current is applied to the antennae throughout the simulation. After an initial transient period of the order of several ion transit times, a steady-state equilibrium is achieved provided the applied antenna currents were sufficient and the initial density was not too far from the final density. One need not start the simulations with an initial density; however, a more complex antenna circuit would have been necessary to allow for the build-up of a discharge from breakdown. After the stable discharge is formed, the applied current (to the antennae) is incrementally lowered to a minimum value below which the plasma extinguishes. The coarseness

of the current decrement provides some source of error in the determination of the minimum; however, this method is estimated to yield measurements of I_{min} no more than 15% above the actual value. The existence of a minimum applied current is analogous to the minimum applied voltage observed by Godyak and Popov [38] and demonstrated in simulation by one of the authors and a co-worker [34].

Much of the simulation output, which will be presented in section 4, is produced by cycle averaging the signals through one period of the applied signal.

4. Results

In presenting our results for surface wave sustained discharges using the models described in section 2, it is convenient to treat the surface waves as being electrostatic. The fully electromagnetic simulation described in section 3 produces the vacuum antenna fields shown in figures 3–6. For the frequencies of operation (150–300 MHz), the free space wavelength is much longer than the dimensions and wavelengths chosen for our discharges (i.e., the drive

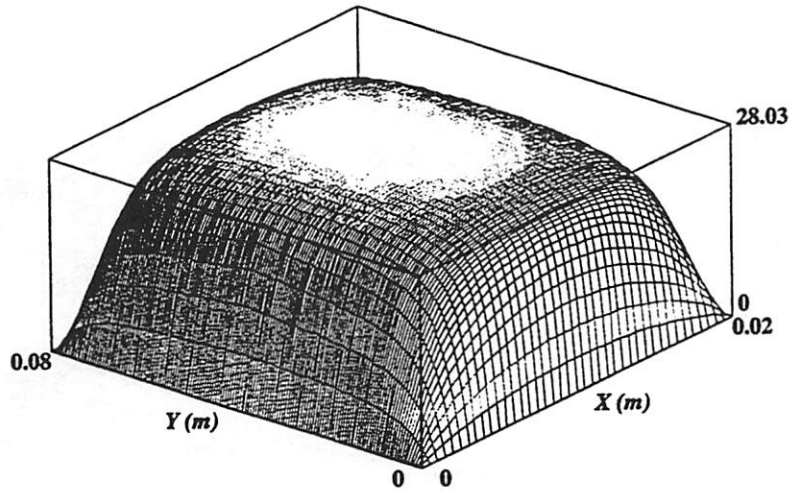


Figure 8. Average electrostatic potential, $\Phi(x, y)$ (in volts), for double-bounded system.

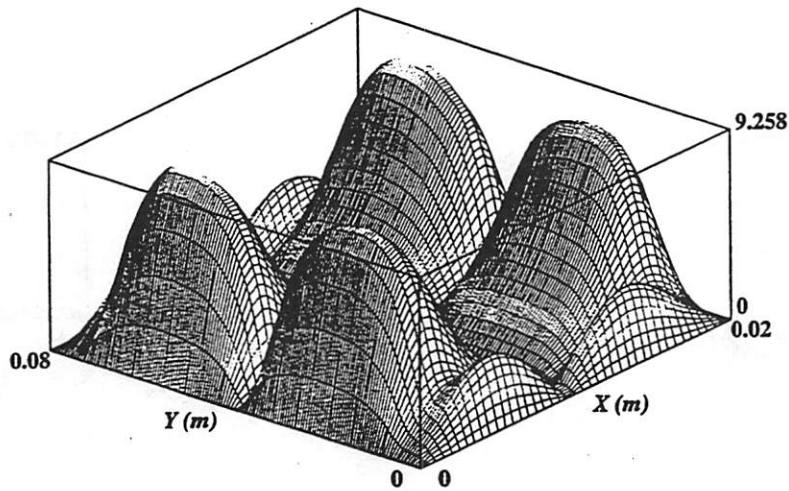


Figure 9. Amplitude of the electrostatic potential signal (in volts) at the fundamental (drive) frequency, $|\Phi(x, y, \omega_H = 150 \text{ MHz})|$ as measured by simulation, for double-bounded system.

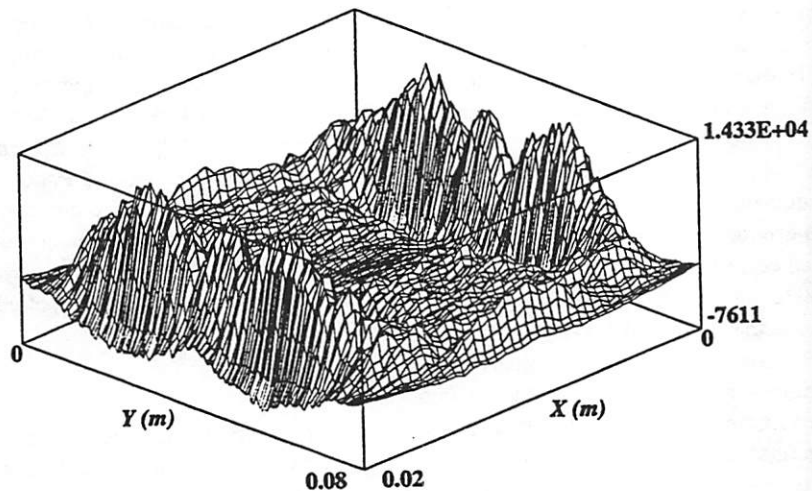


Figure 10. Average electron heating profile, $\langle J_{\text{electron}} \cdot E \rangle_t$ (in W m^{-3}), for double-bounded system.

frequencies are well below cutoff for the conducting parallel plate system in the absence of plasma), and the fields are

found to decay exponentially away from the antennae. At these frequencies, the surface wave modes present in the

Table 1. Varying ω_H , fixed neutral density: parameters for various experiments, ν_m (Hz) $\approx 10^7 T_e$ (eV). $\lambda_{ion m.f.p.}$ (cm) $\approx 3.2 p_{gas}$ (mTorr), $k_y = 3.93$ cm $^{-1}$, $L_x = 2$ cm for experiments A–D. n_e , f_{pe} and V_{plasma} represent peak time averaged values.

Experiment	f_{source} (MHz)	p_{argon} (mTorr)	I_{source} (A m $^{-1}$)	n_e (cm $^{-3}$)	f_{pe} (MHz)	T_e (V)	V_{plasma} (V)	P (W)	Q
A	150	10.0	600	1.1×10^9	300	3.3	21	0.41	2.3
B	200	10.0	350	2.2×10^9	420	3.4	21	0.77	3.8
C	250	10.0	300	5.1×10^9	640	3.2	23	1.7	5.7
D	300	10.0	260	8.6×10^9	830	3.2	25	2.7	10

Table 2. Varying neutral density, fixed ω_H : parameters for various experiments, $\lambda_{ion m.f.p.}$ (cm) $\approx 3.2 p_{gas}$ (mTorr), $k_y = 3.93$ cm $^{-1}$, $L_x = 2$ cm for experiments E–G. n_e , f_{pe} and V_{plasma} represent peak time averaged values. ν_m and λ_m are the electron momentum collision frequency and mean free path for electron–neutral collisions respectively. (Experiments F and B are identical.)

Experiment	f_{source} (MHz)	p_{argon} (mTorr)	I_{source} (V)	n_e (cm $^{-3}$)	f_{pe} (MHz)	ν_m (MHz)	λ_{me} (cm)	T_e (V)	V_{plasma} (V)	P (W)	Q
E	200	2.0	600	2.2×10^5	420	9.7	15	4.7	31	1.3	3.1
F	200	10.0	350	2.2×10^9	420	36	3.4	3.4	21	0.77	3.8
G	200	100.0	290	3.4×10^9	520	250	0.42	2.4	17	0.59	2.3

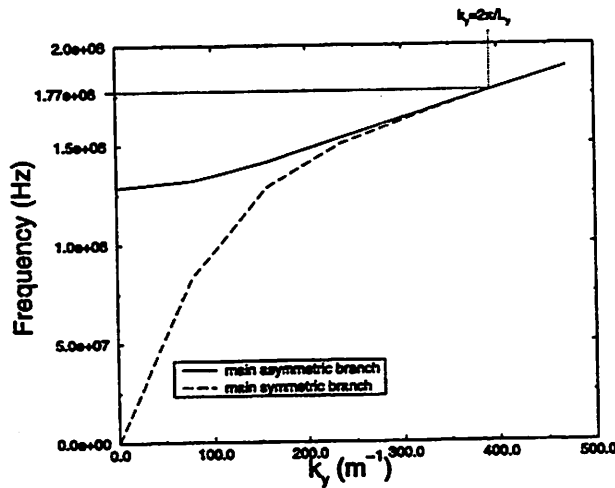


Figure 11. Theoretical dispersion relation for the main symmetric and asymmetric surface wave for the plasma density and electron temperature measured in experiment B (table 1).

steady-state discharges are ‘slow waves’ with wavelengths much shorter than those of light at the same frequency in free space. The result is that the plasma responds nearly electrostatically to the applied electrodynamic fields. As evidence that our approximation is valid, we have observed that the ratio of the (time and space averaged) perturbed electrostatic (derived from Poisson’s equation) field energy density to the perturbed electrodynamic field energy density is $\gtrsim 0.9$ for all simulations. In order to study surface waves at longer wavelengths in \hat{y} or at higher frequencies (achieved by varying the cavity and antennae design) one must abandon the electrostatic approximation. Also, if the free-space wavelength approaches the slab width in \hat{x} , the electrostatic approximation fails. As a further comment, in the studies of travelling surface wave sustained plasma columns, the axial wavelength of the surface wave

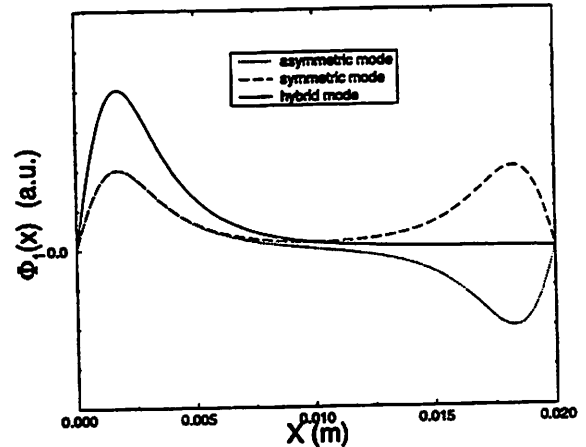


Figure 12. Theoretical eigenfunction, $\Phi_1(x, k_y = 2\pi/1.6$ cm $^{-1}$), for the plasma density and electron temperature measured in experiment B (table 1).

varies as the plasma density decays and the electrostatic approximation may be valid at the end of the plasma column and invalid at the beginning since the axial wavelength generally decreases with decreasing density.

We now proceed with a presentation and discussion of our simulation results.

4.1. Case 1: bound in x and y

For this simulation (see figures 1, 3 and 4) two antennae are driven by ideal current sources operating at 150 MHz with peak current of 700 A m $^{-1}$ (the units reflecting a depth in the unresolved \hat{z} dimension). The antennae signals are 180 degrees out of phase in order to excite an asymmetric standing surface wave in the plasma along \hat{y} . The argon neutral pressure is 10 mTorr. The average electron density and the electrostatic potential in the steady-state discharge are shown in figures 7 and 8. The time averaged peak

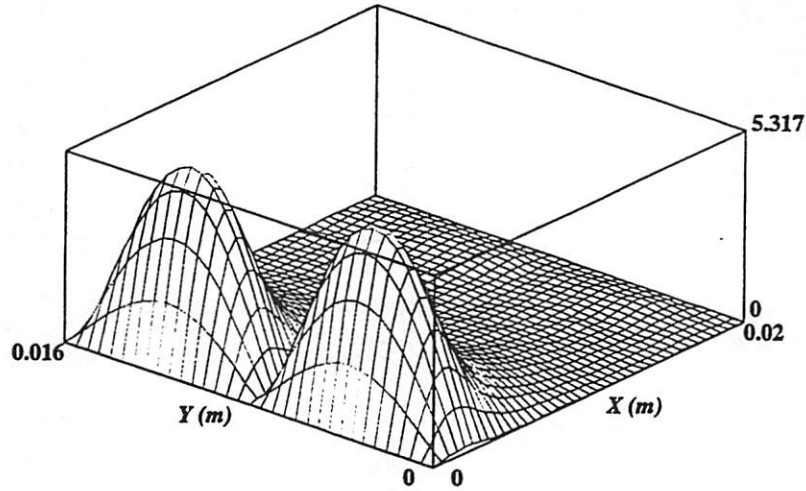


Figure 13. Amplitude of the electrostatic potential signal (in volts) at the fundamental (drive) frequency, $|\Phi(x, y, \omega_d = 200 \text{ MHz})|$ as measured in experiment B.

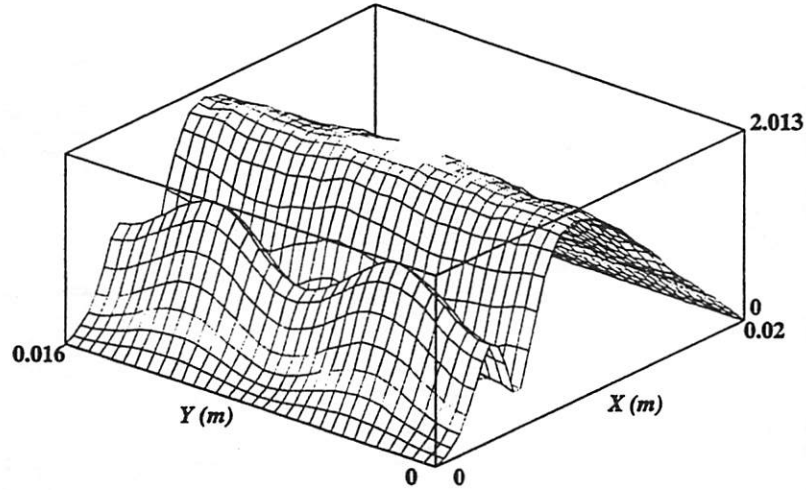


Figure 14. Amplitude of the electrostatic potential signal (in volts) at the second harmonic of the drive frequency, $|\Phi(x, y, 2\omega_d = 400 \text{ MHz})|$ as measured in experiment B.

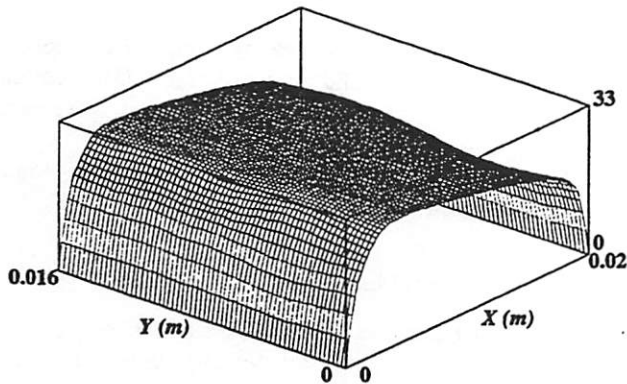


Figure 15. Potential at $t = 0$.

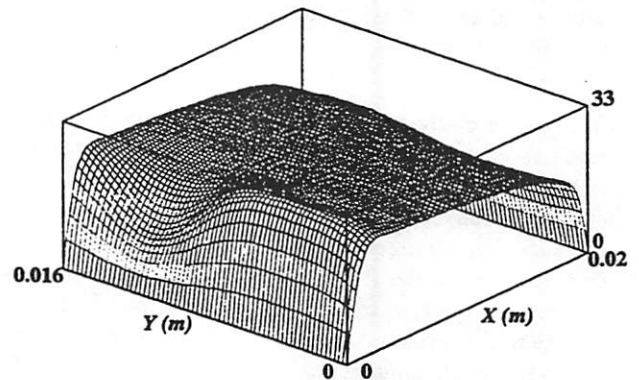
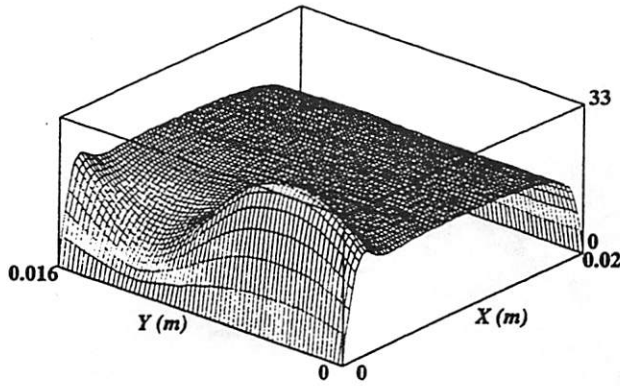
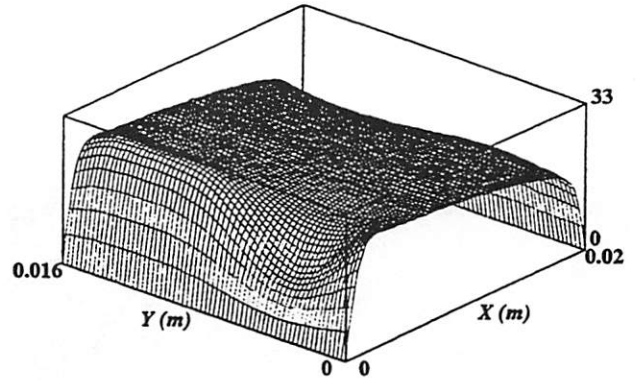
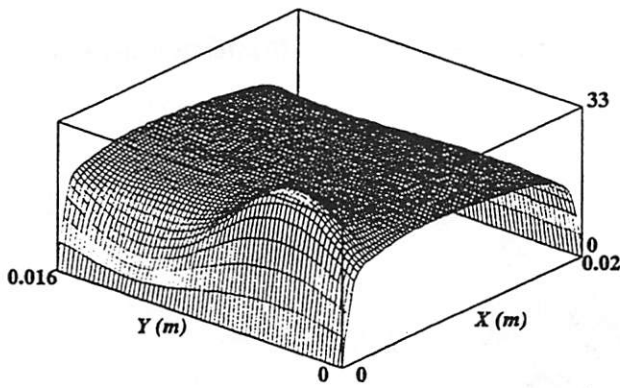
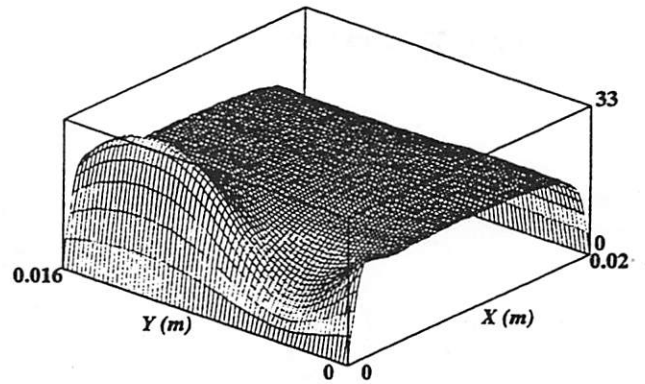
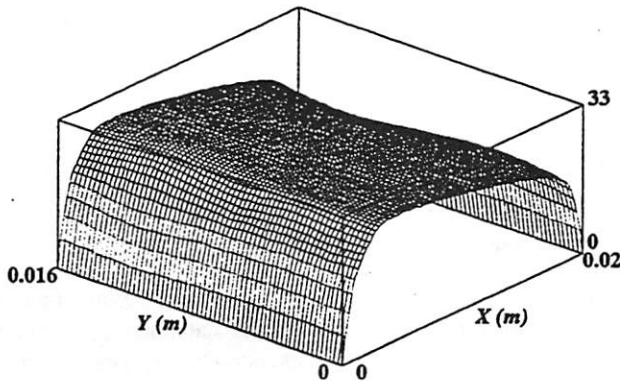
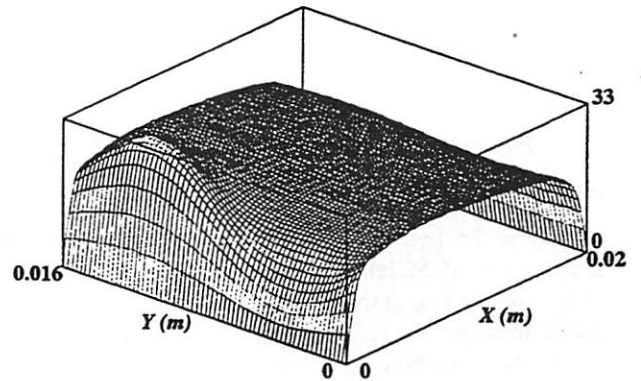


Figure 16. Potential at $t = T/8$.

density is $2.19 \times 10^{15} \text{ m}^{-3}$ which leads to a peak plasma frequency of 420 MHz. The DC peak potential is 28 V. The electron temperature, defined as $2\langle KE \rangle / 3$, is 3.4 eV. The ratio of electrostatic electric field energy density to

electrodynamic electric field energy density is 0.99. The power supplied to the discharge, which is calculated from an integration over volume of the time averaged $\mathbf{J} \cdot \mathbf{E}$, is 3.39 W (taking 1 m depth in \hat{z}). The amplitude of the


 Figure 17. Potential at $t = 2T/8$.

 Figure 20. Potential at $t = 5T/8$.

 Figure 18. Potential at $t = 3T/8$.

 Figure 21. Potential at $t = 6T/8$.

 Figure 19. Potential at $t = 4T/8$.

 Figure 22. Potential at $t = 7T/8$.

standing surface wave is shown in figure 9. Reflection at the y boundaries produces only small deviation from perfect reflection in which the wave would exhibit purely sinusoidal behaviour in \hat{y} (actually a standing surface wave can also be seen along the \hat{y} boundaries!). The potential shown in figure 9 is in good qualitative agreement with the fields predicted by the main asymmetric surface wave in a metal bound plasma slab [29, 30].

The quality of the resonance is given by

$$Q = \frac{2\pi}{T} \frac{\text{stored energy}}{\text{power dissipated}} = \frac{\omega_{rf}}{\text{fwhm}}$$

where T is the wave period. This can be computed with the approximation that the RF stored energy density is given by

$$\begin{aligned} & \frac{\epsilon_0}{2} |E(x, y, t) - \langle E(x, y, t) \rangle_t|^2 \\ & + \frac{m_e}{2} (n_e(x, y, t) |v(x, y, t)|^2 \\ & - \langle n_e(x, y, t) \rangle_t | \langle v(x, y, t) \rangle_t |^2) \end{aligned}$$

which is integrated over space and averaged over time. The power loss is given by the time averaged $J \cdot E$ integrated over space. The result is a Q factor of 8.5. We note that

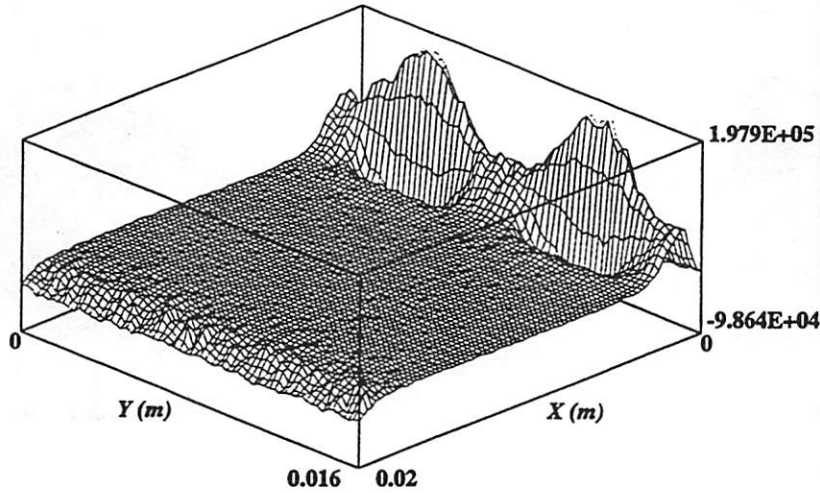


Figure 23. Average electron heating profile, $(J_{ex} \cdot E_x)_t$ (in $W m^{-3}$) at $f = 300$ MHz, $p = 10$ mTorr (experiment D).

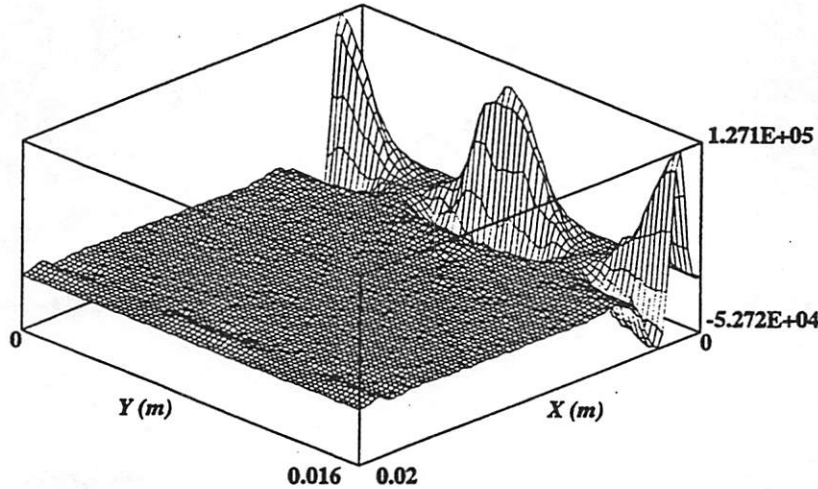


Figure 24. Average electron heating profile, $(J_{ey} \cdot E_y)_t$ (in $W m^{-3}$) at $f = 300$ MHz, $p = 10$ mTorr (experiment D).

$\omega_{rf}/\nu_c = 26$ (where ν_c is the electron-neutral collision frequency ~ 36 MHz). The underestimate of the measured Q may be due in part to the presence of collisionless heating which increases the effective collision frequency.

Evidence of non-ohmic heating is shown in figure 10 in which the time averaged $J_e \cdot E$ is plotted. There is qualitative agreement with the heating profiles at similar densities and pressures in 1D series resonance sustained discharges [34]. The oscillatory pattern along the \hat{y} boundaries is thought to arise from a collisionless heating mechanism. For further discussion of this phenomenon see Cooperberg and Birdsall [34].

Before proceeding, it should be noted that a significant potential signal in the discharge is observed at the second harmonic of the applied frequency as in capacitive discharges [39]. The ratio of the peak potential at the second harmonic to the peak potential at the first harmonic is ~ 0.4 . The strength of this harmonic may be due in part to coupling to higher (Tonks-Dattner) surface wave modes [30]. Third and higher harmonics are not significantly generated in this or subsequently described experiments.

4.2. Case 2: bound in x , periodic in y

A series of computer experiments has been conducted using the model having N phased antennae represented in figure 2. Two sets of experiments were performed. In one, the applied frequency is varied at fixed argon pressure. In the other, the argon pressure is varied at constant applied frequency. Before discussing these experiments, we briefly discuss how the device pictured in figure 2 excited electron surface waves.

The main electron surface modes in the non-uniform, collisionless, thermal, metal bound plasma slab are measured and analysed (in the linear regime) by Cooperberg [29,30]. Applying the same numerical techniques as in this previous work, and using an electron temperature and steady-state density profile determined from a representative surface wave sustained discharge (identified as experiment B in table 1 and experiment F in table 2), we find the linear fluid result for the dispersion relations of the main symmetric and asymmetric surface waves which are plotted in figure 11. For $k_y =$

3.93 cm^{-1} , which is determined by our antennae structure, the two modes occur at nearly the same frequency, $f = 180 \text{ MHz}$, and they can be excited simultaneously. Note the experimentally measured frequency, at $k_y = 3.93 \text{ cm}^{-1}$, is $f = 200 \text{ MHz}$, in reasonable agreement with the theory. The potential perturbation resulting from the sum of the symmetric and asymmetric modes, as derived from the fluid theory, is plotted in figure 12. A sinusoidal dependence in \hat{y} is not shown. This eigenfunction can be compared with the experimentally measured amplitude of the potential oscillating at the fundamental (applied) frequency in the sustained discharge (figure 13). Reasonable agreement is again achieved. The amplitude of the potential oscillating at the second harmonic of the applied frequency is shown in figure 14.

Now we discuss our first set of simulations in which the neutral gas (argon) pressure is fixed at 10 mTorr and the driving frequency is varied. At 10 mTorr the electron mean free path is of the order of the system size and non-local heating may be assumed. Also for at this pressure the argon discharge is in a diffusion regime for charged particle losses. Results for these experiments are summarized in table 1. Several conclusions can be drawn from these data. First, we find that the peak steady-state plasma potentials are nearly the same and of the order of $7T_e$. We also find that the T_e values are nearly the same in these experiments. The applied frequency is consistently less than the plasma frequency associated with the peak plasma density located in the central overdense region as is expected for electron surface waves. The quality factor, Q (computed from the ratio of stored to dissipated energy described in section 4.1), is less than is predicted by ω_{rf}/ν_c (where ν_c is the electron-neutral collision frequency $\sim 36 \text{ MHz}$). This error may be due to additional dissipation through collisionless heating, and, also, to poor antenna coupling. To explain the decreasing I_{min} we note that the electric field strength generated by a current loop antennae in vacuum is $\propto \omega I$, and, by analogy with 1D series resonant discharges [6, 34], we expect the minimum E field to be a function of gas pressure and spatial dimensions, and not driving frequency.

Significant second-harmonic generation is again detected for the experiments listed in table 1. The peak potential at the second harmonic is approximately 0.4 times the peak at the applied frequency and our previous calculations of Q must be considered as approximate.

Figures 15–22 show snapshots of the electrostatic potential in the plasma over one period of the applied signal (for experiment D). For the same experiment, the electron heating in \hat{x} and \hat{y} is shown in figures 23 and 24. The oscillatory behaviour of $J_{ex} \cdot E_x$ on the antenna side of the slab again shows qualitative agreement with 1D measurements [34]. The oscillatory behaviour of $J_{ey} \cdot E_y$ may be caused by collisionless heating in the propagation direction (\hat{y}). Similar, although less pronounced oscillations, are observed in the $J_e \cdot E$ of the other experiments.

Finally, we have plotted ω_{rf} versus n_{peak} in figure 25. The data, over the limited frequency range measured, seems

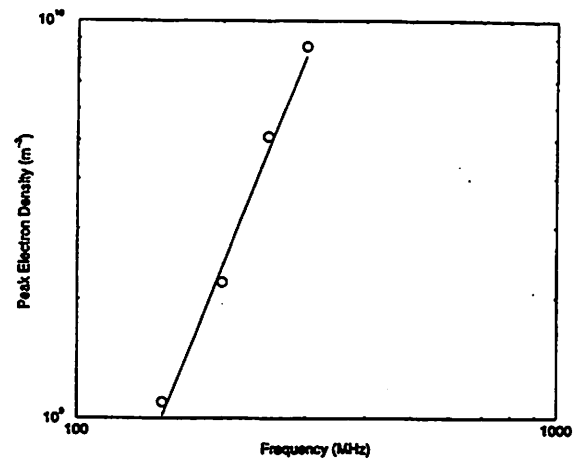


Figure 25. Peak electron density versus applied frequency. The line represents $n_{peak} \propto \omega_{rf}^3$, $p_{argon} = 10 \text{ mTorr}$.

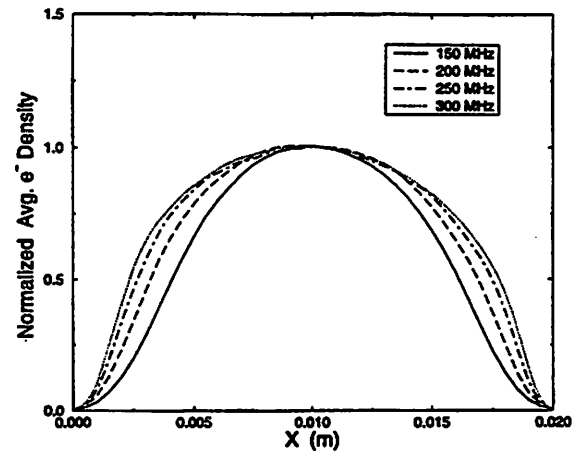


Figure 26. Electron densities averaged in \hat{y} and time. Sheath width decreases with increasing applied frequency, $p_{argon} = 10 \text{ mTorr}$.

to agree with the 1D prediction [6] that $n_{peak} \propto \omega_{rf}^3$. Also shown are the average electron density profiles in \hat{x} (figure 26) in which it is observed that the sheath width decreases with increasing drive frequency. It is observed that the variation of the steady-state electron density in \hat{y} is less than 2% for experiments A–D.

The second set of surface wave sustained discharge experiments, in which frequency is fixed and neutral pressure is varied, are summarized in table 2. The data shows that electron temperature, T_e , increases with decreasing pressure as can be expected [39]. Also the quality factor is decreased at higher pressure as can be expected due to a higher collision frequency. Q is lower at 2 mTorr than at 10 mTorr which is not expected. A possible explanation is weaker coupling to the antenna fields since the plasma density profile varies with pressure; however, more comprehensive simulation is needed to clarify this seeming discrepancy. The ratio of the peak amplitude of the electrostatic potential at the second harmonic to that at the fundamental frequency is 0.58, 0.38, 0.19 for experiments E, F and G respectively. This shows a decrease in second-harmonic generation for more

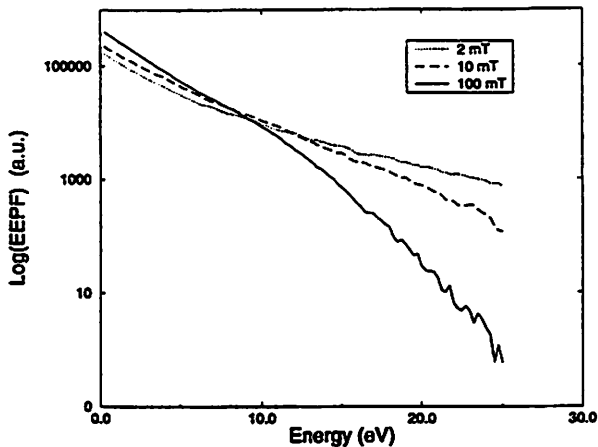


Figure 27. Electron energy probability functions for varying neutral pressure, $f = 200$ MHz. A hot-tail is present at the lowest pressure.

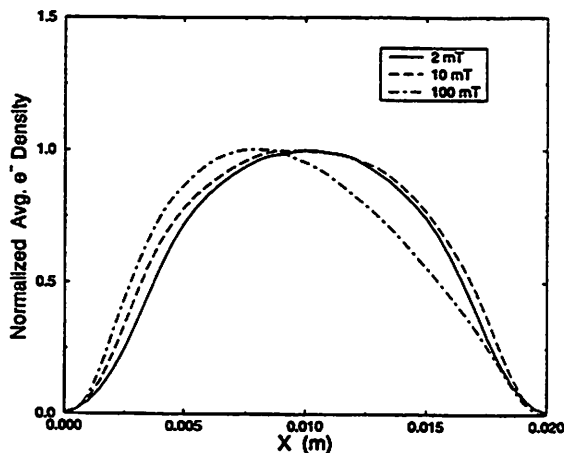


Figure 28. Electron densities averaged in \hat{y} and time. Density asymmetry is visible at the highest pressure, $f = 200$ MHz.

dissipative systems.

Figure 27 shows the electron energy probability function (EEPF) averaged over space for each experiment (E, F and G). Experiment E (2 mTorr) exhibits a hot-electron tail analogous to the lower-pressure 1D discharges described in a previous article [34]. At the higher pressure (experiment G, 100 mTorr) the tail is lost and, instead, we see depletion of the distribution at higher energies, which is presumably due to inelastic collisions.

Figure 28 shows electron density profiles averaged in \hat{y} and time. Again, variation of the steady-state electron density function in \hat{y} is less than 2% in each experiment. The increased density on the antenna side of the discharge for the highest-pressure simulation (experiment G) may be due to a shift from a non-local regime (long electron mean free path) to a local one (short electron mean free path) as indicated in table 2.

5. Conclusions

We have shown, via PIC-MCC simulation, that metal bound planar plasma discharges can be sustained via

standing surface wave excitation. Discharges in both infinite (periodic) and bound slabs have been successfully modelled. Low-voltage, low- (and moderate-) pressure plasmas which exhibit uniform densities in the directions parallel to the slab boundaries are produced.

The scalability to larger discharge areas, possibility for operation at higher frequencies (leading to higher densities), and ability to operate in a one-sided mode where large surface wave fields and electron heating are localized to one edge of the plasma slab, along with the lack of complexity in the reactor design, give this type of discharge promise for use in applications such as materials processing. Also, since the plasma is completely surrounded by conducting walls, there is no HF radiation loss associated with dielectric or partially dielectric bound HF sources. One can also speculate that excitation of surface waves along the conducting containing boundaries present in other types of plasma source may be used as a secondary heating mechanism in order to modify or enhance plasma density and uniformity.

Further simulation and computational speed-ups may lead to efficient modelling of larger-area, higher-density plasmas. Further simulations and laboratory experiments are needed to perfect a more efficient wave exciting mechanism. Also, the details of collisionless electron heating mechanisms in two dimensions need further investigation.

Acknowledgments

The technical assistance offered by J Verboncoeur and V Vahedi in adapting XDPD2 for this work is greatly appreciated. Assistance in incorporating surface impedance into the code was thankfully received from K Cartwright. This work was supported in large part by ONR-ASSERT N100014-93-1-1389. Much of the simulation work presented here was performed on the Berkeley NOW Project computing facility.

References

- [1] Taillet J 1969 Resonance-sustained radio frequency discharges *Am. J. Phys.* **37** 423
- [2] Vandenplas P E 1968 *Electron Waves and Resonances in Bounded Plasmas* (New York: Interscience)
- [3] Messiaen A M and Vandenplas P E 1967 Nonlinear resonance effect at high power in a cylindrical plasma *Phys. Lett.* **25A** 339
- [4] Messiaen A M and Vandenplas P E 1969 Resonantly sustained bounded radiofrequency plasma in a spherical cavity *Appl. Phys. Lett.* **15** 30
- [5] Godyak V A 1976 Steady-state low-pressure RF discharges *Sov. J. Plasma Phys.* **2** 78
- [6] Godyak V A 1986 *Soviet RF Discharge Research* (Falls Church, VA: Delphic Associates)
- [7] Fehsenfeld F C, Evenson K M and Broida H P 1965 Microwave discharge cavities operating at 2450 MHz *Rev. Sci. Instrum.* **36** 294
- [8] Moisan M, Beaudry C and Leprince P 1975 A small microwave plasma source for long column production without magnetic field *IEEE Trans. Plasma Sci.* **3** 55

- [9] Moisan M and Zakrzewski Z 1991 Plasma sources based on the propagation of electromagnetic surface waves *J. Phys. D: Appl. Phys.* **24** 1025
- [10] Zakrzewski Z, Moisan M, Glaude V M M, Beaudry C and Leprince P 1977 Attenuation of a surface wave in an unmagnetized RF plasma column *Plasma Phys.* **19** 77
- [11] Zakrzewski Z 1983 Conditions of existence and axial structure of long microwave discharges sustained by travelling waves *J. Phys. D: Appl. Phys.* **16** 171
- [12] Glaude V M M, Moisan M and Pantel R 1980 Axial electron density and wave power distributions along a plasma column sustained by the propagation of a surface microwave *J. Appl. Phys.* **51** 5693
- [13] Ferreira C M 1981 Theory of plasma column sustained by a surface wave *J. Phys. D: Appl. Phys.* **14** 1811
- [14] Ferreira C M 1983 Modelling of a low-pressure plasma column sustained by a surface wave *J. Phys. D: Appl. Phys.* **16** 1673
- [15] Aliev Yu M, Boev A G and Shivarova A P 1982 On the non-linear theory of a long gas discharge produced by an ionizing slow electromagnetic wave *Phys. Lett.* **92** 235
- [16] Aliev Yu M, Boev A G and Shivarova A P 1984 Slow ionising high-frequency electromagnetic wave along a thin plasma column *J. Phys. D: Appl. Phys.* **17** 2233
- [17] Aliev Yu M, Maximov A V, Bychenkov V Yu and Schlüter H 1992 High energy electron generation in surface-wave-produced plasmas *Plasma Sources Sci. Technol.* **1** 126
- [18] Rakem Z, Leprince P and Marec J 1992 Modelling of a microwave discharge created by a standing surface wave *J. Phys. D: Appl. Phys.* **25** 953
- [19] Rakem Z, Leprince P and Marec J 1990 Characteristics of a surface wave produced discharge operating under standing wave conditions *Revue Phys. Appl.* **25** 125
- [20] Nonaka S 1994 Proposal of non-cylindrical and large-area RF plasma productions by surface wave *J. Phys. Soc. Japan* **63** 3185
- [21] Nonaka S 1995 The axial gradient of planar RF plasmas produced by a surface wave *J. Phys. D: Appl. Phys.* **28** 1058
- [22] Komachi K and Kobayashi S 1989 Generation of a microwave plasma using travelling waves *J. Microwave Power Electromagn. Energy* **24** 140
- [23] Nagatsu M, Xu G, Yamage M, Kanoh M and Sugai H 1997 Optical emission and microwave field intensity measurements in surface wave-excited planar plasma *Japan. J. Appl. Phys.* **35** 341
- [24] Ghanashev I, Nagatsu M and Sugai H 1997 Surface wave eigenmodes in a finite-area plane microwave plasma *Japan. J. Appl. Phys.* **36** 337
- [25] Bosisio R G, Weissfloch C F and Wertheimer M R 1972 The large volume microwave plasma generator (LMPTM): a new tool for research and industrial processing *J. Microwave Power* **7** 325
- [26] Bosisio R G, Wertheimer M R and Weissfloch C F 1973 Generation of large volume microwave plasmas *J. Phys. E: Sci. Instrum.* **6** 628
- [27] Sauvé G, Moisan M, Zakrzewski Z and Bishop C A 1995 Sustaining long linear uniform plasmas with microwaves using a leaky-wave (troughguide) field applicator *IEEE Trans. Antennas Propag.* **AP-43** 249
- [28] Zakrzewski Z and Moisan M 1995 Plasma sources using long linear microwave field applicators: main features, classification and modelling *Plasma Sources Sci. Technol.* **4** 379
- [29] Cooperberg D J 1997 Electron surface waves in a plasma slab with uniform ion density *Phys. Plasmas* accepted for publication
- [30] Cooperberg D J 1997 Electron surface waves in a nonuniform plasma slab *Phys. Plasmas* accepted for publication
- [31] Napoli L S and Swartz G A 1963 Wave propagation in a tubular plasma *Phys. Fluids* **6** 918
- [32] Birdsall C K and Langdon A B 1991 *Plasma Physics Via Computer Simulation (The Adam Hilger Series on Plasma Physics)* (Bristol: Hilger)
- [33] Vahedi V and Surendra M 1995 A Monte Carlo collision model for the particle-in-cell method: applications to argon and oxygen discharges *Comput. Phys. Commun.* **87** 179
- [34] Cooperberg D J and Birdsall C K 1997 Series resonance sustained plasmas in a metal bound plasma slab *Plasma Sources Sci. Technol.* submitted
- [35] Vahedi V, DiPeso G, Rognlien T D and Birdsall C K 1993 Verification of frequency scaling laws for capacitive RF discharges using two-dimensional simulations *Phys. Fluids B* **5** 2719
- [36] Verboncoeur J P, Langdon A B and Gladd N T 1995 An object-oriented electromagnetic PIC code *Comput. Phys. Commun.* **87** 199
- [37] Rambo P, Ambrosiano J and Friedman A 1989 Temporal and spatial filtering remedies for dispersion in electromagnetic particle codes *Proc. 13th Conf. on the Numerical Simulation of Plasmas (Santa Fe, NM, 1989)* p PMA9
- [38] Godyak V A and Popov O A 1979 Experimental study of resonant rf discharges *Sov. J. Plasma Phys.* **5** 227
- [39] Lieberman M A and Lichtenberg A J 1994 *Principles of Plasma Discharges and Materials Processing* (New York: Wiley)